

INFORMATION TO USERS

This manuscript has been reproduced from the microfilm master. UMI films the text directly from the original or copy submitted. Thus, some thesis and dissertation copies are in typewriter face, while others may be from any type of computer printer.

The quality of this reproduction is dependent upon the quality of the copy submitted. Broken or indistinct print, colored or poor quality illustrations and photographs, print bleedthrough, substandard margins, and improper alignment can adversely affect reproduction.

In the unlikely event that the author did not send UMI a complete manuscript and there are missing pages, these will be noted. Also, if unauthorized copyright material had to be removed, a note will indicate the deletion.

Oversize materials (e.g., maps, drawings, charts) are reproduced by sectioning the original, beginning at the upper left-hand corner and continuing from left to right in equal sections with small overlaps. Each original is also photographed in one exposure and is included in reduced form at the back of the book.

Photographs included in the original manuscript have been reproduced xerographically in this copy. Higher quality 6" x 9" black and white photographic prints are available for any photographs or illustrations appearing in this copy for an additional charge. Contact UMI directly to order.

U·M·I

University Microfilms International
A Bell & Howell Information Company
300 North Zeeb Road, Ann Arbor, MI 48106-1346 USA
313/761-4700 800/521-0600

Order Number 9416848

**Ground motion studies in the Southern Great Basin of Nevada
and California**

Samiezáde Yazd, Mohammad Reza, Ph.D.

Saint Louis University, 1993

U·M·I

300 N. Zeeb Rd.
Ann Arbor, MI 48106

GROUND MOTION STUDIES IN THE SOUTHERN GREAT BASIN
OF NEVADA AND CALIFORNIA

Mohammad Reza Samiezhadé Yazd, B.S., M.S.

A Dissertation Presented to the Faculty of the Graduate School
of Saint Louis University in Partial Fulfillment of
the Requirements for the Degree of
Doctor of Philosophy

1993

GROUND MOTION STUDIES IN THE SOUTHERN GREAT BASIN
OF NEVADA AND CALIFORNIA

Mohammad Reza Samiezhadé Yazd, B.S., M.S.

A Digest Presented to the Faculty of the Graduate School
of Saint Louis University in Partial Fulfillment of
the Requirements for the Degree of
Doctor of Philosophy

1993

DIGEST

Spatial amplitude attenuation of high frequency seismic waves of locally recorded earthquakes in the Southern Great Basin near the Nevada Test Site was studied by constructing a response spectra data base of SV and PSRV using a time-domain deconvolution method to restore the ground motion from instrumental recordings. Response spectra are shown to be an efficient method for estimating ground motion for attenuation studies of small size earthquakes at local distances. The epicentral distances for the data set are from 5 km to 200 km.

The geometrical spreading rate changes markedly between 60 and 120 km, requiring a segmented geometrical spreading approach to be used. PSRV attenuation is controlled by a moderate frequency dependence with $Q = 600 f^{0.15}$ for $f < 8$ Hz and $Q = 150 f^{0.8}$ for $f > 8$ Hz. Coda Q values based on a single scattering model were calculated to be $Q_c = 150 f^{0.9}$. Based on source-site-path separability of coda, the S-waves were normalized to a common source excitation and the resultant data base was inverted for attenuation parameters. A frequency-dependent Q similar that of the SV regression resulted from this data set. In addition, a frequency-independent Q of $Q = 1661$ with geometrical spreading r^{-1} also describes the data well, but fails in describing the detailed attenuation in the 60 - 120 km range. The Q values calculated for the S waves at distances less than 60 km are close to the coda Q values.

The Radiative Transfer Energy approach shows that the coda Q values at lower frequencies are dominated by scattering and that the peak motion attenuation, on the contrary, is dominated by anelastic attenuation. Site effects are dominant features that affect spectral levels in the Nevada Test Site. Site amplification studies were conducted using the coda waves, response spectra data, and spectral method. There is general agreement among the three methods and the agreement between the site terms from peak motion and the residual of spectrum is particularly good when the number of recordings at a given station exceeds 10. A correlation is noted between site terms and site geology.

COMMITTEE IN CHARGE OF CANDIDACY :

**Professor Robert B. Herrmann,
Chairperson and Advisor**

Professor Brian J. Mitchell

Assistant Professor Frederick M. Chester

ACKNOWLEDGEMENTS

I would like to thank my mother, Safa, my wife, Caroline, and my children, Safa, Isa Amin, and Azadeh, for unconditionally supporting me and giving me their love for all these years. I thank Dr. Robert Herrmann, my adviser, for suggesting the idea presented here and for his thoughtful comments that guided me through much of this work, and for his careful review of the manuscript. I also thank Drs. Brian Mitchell and Frederick Chester for reviewing this dissertations and their comments. I thank Dr. Karl Chau for all the help he gave me, Eric Haug for maintaining a high quality computing facility, and Melanie Whittington for her friendly assistance.

I would like to express my deep gratitude to the memory of the late Dr. Otto Nuttli who inspired me as a human being and as an earth scientist.

TABLE OF CONTENTS

Chapter 1 -- Introduction	1
1.1 Statement of Problem	1
1.2 Geology of the Southern Great Basin	3
1.3 Seismicity of the Nevada Test Site	6
1.4 Thickness of the crust at Nevada Test Site	7
Chapter 2 -- Restitution of Ground Motion, Recursive Deconvolution Filters	11
2.1 Introduction	11
2.2 Recursive Filter Method	12
2.3 Southern Great Basin Seismic Network	15
2.4 Inverse filters, deconvolution	22
2.5 Application of zero-phasing inverse filter to SGB system	28
Chapter 3 -- Attenuation of Response Spectra	44
3.1 Introduction	44
3.2 Parametrization of the attenuation problem	46
3.3 Singular value decomposition and the stochastic inverse	50
3.4 Attenuation measurements	52
3.5 Discussion and conclusions	59
Chapter 4 -- Coda Wave Methods	70
4.1 Introduction	70
4.2 Coda Q method	72
4.3 Coda Q measurements	75
4.4 Q of S waves using coda normalization method	79
4.5 Parametrization of the attenuation problem	87
4.6 Attenuation measurements	89
4.7 Discussion and conclusions	97

Chapter 5 -- Attenuation, Scattering, and Coda Q for the Southern Great Basin between 2 and 16 Hz	101
5.1 Introduction	101
5.2 Review of the Radiative Transfer Energy Theory	103
5.3 Methods for measurement of energy density	107
5.4 Measurements of scattering and anelastic attenuation	117
5.5 Discussion and conclusions	124
 Chapter 6 -- Local Site Effects	 130
6.1 Introduction	130
6.2 Coda site amplification	135
6.3 Site amplification from S waves	155
6.4 Site effects using spectral model	157
6.5 Discussion and conclusions	164
 Chapter 7 -- Conclusions	 168
 Appendix A -- Response Spectra	 174
1. Introduction	174
2. Definition of response spectra	175
3. Computation of response spectra for digitized data	175
4. Fourier spectrum	179
5. Energy consideration	180
 Bibliography	 182
 Vita Auctoris	 189

LIST OF TABLES

TABLES		PAGE
1.1	List of the Southern Great Basin Earthquakes	10
2.1	SGB Network Station Parameters	16
2.2	Constant values of SGB instruments	19
3.1	Trilinear regression of PSRV data	60
3.2	Trilinear regression of PSRV with fixed geometrical spreading at large distances	65
3.3	Bilinear regression of PSRV data in SGB	66
4.1	Coda Q values of the Southern Great Basin	80
4.2	Trilinear fit to the coda normalized S-wave data	91
4.3	Q values of direct S wave	94
5.1	Intrinsic and scattering Q parameters of SGB	123
6.1	Site geology and site attenuation parameter of SGBSN	162
7.1	Q relations in the SGB	172

LIST OF ILLUSTRATIONS

FIGURE		PAGE
1.1	Earthquakes recorded on the Southern Great Basin Seismic Network, SGBSN, used for this study.	8
1.2	Histogram of the observed records used for this study. The vertical axis is the number of observations for every 10 km of epicentral distance, while the horizontal axis is the epicentral distance.	9
2.1	Map of the SGBSN between the border of Nevada and California. Location of the stations are shown by open triangles.	18
2.2	An impulsive time function, shown by the solid line, is input into the recursive instrument system of L4C-V and the output is input into the inverse deconvolution filter of the same instrument system. The long dashed line is the output for $\xi = 0.94$ while the short dashed line shows the output for $\xi = 0.98$.	24
2.3	Transfer function amplitude versus frequency for the L4C-V system. The solid line is the analog amplitude, the dashed line is the amplitude response calculated from the inverse recursive filter.	29
2.4	Transfer function amplitude versus frequency for the L4C-H system. The solid line is the analog amplitude, the dashed line is the amplitude response calculated from the inverse recursive filter.	30
2.5	Transfer function amplitude versus frequency for the S13-O system. The solid line is the analog amplitude, the dashed line is the amplitude response calculated from the inverse recursive filter.	31

LIST OF ILLUSTRATIONS (continued)

FIGURE		PAGE
2.6	Transfer function amplitude versus frequency for the L4C-V system. The solid line is the analog amplitude, the dashed line is the amplitude response calculated from the inverse recursive filter.	32
2.7	Test of reconstitution of input for L4C-V system. An impulse time function is input in the recursive instrument response function and the inverse recursive deconvolution filter is applied on the output. The output is a zero phase, unit spectrum, which is approximately realized in the passband.	34
2.8	Test of reconstitution of input for L4C-H system. An impulse time function is input in the recursive instrument response function and the inverse recursive deconvolution filter is applied on the output. The output is a zero phase, unit spectrum, which is approximately realized in the passband.	35
2.9	Test of reconstitution of input for S13-O system. An impulse time function is input in the recursive instrument response function and the inverse recursive deconvolution filter is applied on the output. The output is a zero phase, unit spectrum, which is approximately realized in the passband.	36
2.10	Test of reconstitution of input for S13-Y system. An impulse time function is input in the recursive instrument response function and the inverse recursive deconvolution filter is applied on the output. The output is a zero phase, unit spectrum, which is approximately realized in the passband.	37
2.11	An impulsive time function, shown by the solid line, is input into the recursive instrument system of the L4C-V and the inverse recursive deconvolution filter for the L4C-V is applied on the output. The resulting output is shown by the dashed line. Notice the non-causal nature of the procedure causes the early and late arrival of the arrival pulse.	39

LIST OF ILLUSTRATIONS (continued)

FIGURE		PAGE
2.12	An impulsive time function, shown by the solid line, is input into the recursive instrument system of the L4C-H and the inverse recursive deconvolution filter for the L4C-H is applied on the output. The resulting output is shown by the dashed line. Notice the non-causal nature of the procedure causes the early and late arrival of the arrival pulse.	40
2.13	An impulsive time function, shown by the solid line, is input into the recursive instrument system of the S13-O and the inverse recursive deconvolution filter for the S13-O is applied on the output. The resulting output is shown by the dashed line. Notice the non-causal nature of the procedure causes the early and late arrival of the arrival pulse.	41
2.14	An impulsive time function, shown by the solid line, is input into the recursive instrument system of the S13-Y and the inverse recursive deconvolution filter for the S13-Y is applied on the output. The resulting output is shown by the dashed line. Notice the non-causal nature of the procedure causes the early and late arrival of the arrival pulse.	42
2.15	A typical seismogram shown here before removal of instrument and the restituted displacement, velocity, and acceleration after applying the inverse recursive deconvolution procedure. On the top, the seismogram recorded at BGB is shown as units of counts versus time in seconds from the beginning of recording. The other time series shown are displacement, cm; velocity, cm/s; and acceleration, cm/s-s, respectively. Notice that the seismogram and the velocity time series are very similar which is expected because the instrument is a velocity sensor in the passband.	43
3.1	PSRV and SV calculated for the earthquake on May 27, 1986 15:42:46.38. The location of this event is given in Table 2.1. Notice the similarity between these two spectra for frequencies higher than 5 Hz. For frequencies close to zero there is difference between these two measurements as is explained in Appendix A.	53

LIST OF ILLUSTRATIONS (continued)

FIGURE		PAGE
3.2	SV plots versus distance for earthquake 39 of Table 1.1 for frequencies of 2 and 10 Hz.	54
3.3	Typical attenuation plot using SV amplitudes at 2 Hz. All records normalized to the common source and site terms removed.	58
3.4a	Trilinear regression fit to PSRV data for 2 and 4 Hz.	61
3.4b	Trilinear regression fit to PSRV data for 8 and 12 Hz.	62
3.5a	Trilinear regression fit to SV data for 2 and 4 Hz.	63
3.5b	Trilinear regression fit to SV data for 8 and 12 Hz.	64
4.1a	Seismograms of earthquake 5 of Table 1.1 recorded at six stations with epicentral distances ranging from 16 km(top) to 56 km (bottom).	76
4.1b	Seismograms of earthquake 17 of Table 1.1 recorded at six stations with epicentral distances ranging from 48 km (top) to 153 (bottom).	77
4.1c	Seismograms of earthquake 31 of Table 1.1 recorded at six stations with epicentral distances ranging from 120 km (top) to 187 km (bottom).	78
4.2a	Coda normalized amplitudes versus distance for 2 Hz(top) and 4 Hz (bottom).	83
4.2b	Coda normalized amplitudes versus distance for 6 Hz(top) and 8 Hz (bottom).	84
4.2c	Coda normalized amplitudes versus distance for 10 Hz(top) and 12 Hz (bottom).	85
4.2d	oda normalized amplitudes versus distance for 14 Hz(top) and 16 Hz (bottom).	86
4.3a	Bilinear regression fit to the coda normalized data for 2 Hz and 4 Hz. Values of geometrical spreading for the two distance ranges are shown.	92

LIST OF ILLUSTRATIONS (continued)

FIGURE		PAGE
4.3b	Bilinear regression fit to the coda normalized data for for 8 Hz and 12 Hz. Values of geometrical spreading for the two distance ranges are shown.	93
4.4a	Frequency independent Q model fit to the coda normalized amplitude data for 2Hz and 4 z.	95
4.4b	Frequency-independent Q model fit to the coda normalized amplitude data for 8 Hz and 12 Hz.	96
5.1	Theoretical prediction of the Radiative Transfer Energy. Vertical axis is $4\pi r^2 E(r)$, where $E(r)$ is the total energy measured for a long time window of the seismogram. Seismic albedo B_0 varies from 0.99 (top) to 0.2 (bottom).	105
5.2a	Site and source corrected coda energy averaged over 10 km spacing for 2 Hz and 4 Hz at 30, 40, 50, and 60 seconds lapse time.	109
5.2b	Site and source corrected coda energy averaged over 10 km spacing for 10 Hz and 14 Hz at 30, 40, 50, and 60 seconds lapse time. Notice the homogeneity of the coda energy for 30 second lapse time.	110
5.3a	Plot of normalized S-wave energy corrected for geometrical spreading for 2 Hz and 3 Hz. The theoretical curve from the Radiative Transfer Energy is shown by the solid line.	112
5.3b	Plot of normalized S-wave energy corrected for geometrical spreading for 4 Hz and 6 Hz. The theoretical curve from the Radiative Transfer Energy is shown by the solid line.	113
5.3c	Plot of normalized S-wave energy corrected for geometrical spreading for 8 Hz and 10 Hz. The theoretical curve from the Radiative Transfer Energy is shown by the solid line.	114

LIST OF ILLUSTRATIONS (continued)

FIGURE		PAGE
5.3d	Plot of normalized S-wave energy corrected for geometrical spreading for 12 Hz and 14 Hz. The theoretical curve from the Radiative Transfer Energy is shown by the solid line.	115
5.4a	Plots of $\log_{10}(4\pi r^2 PSRV^2)$ versus distance and the corresponding fit to the Radiative Transfer Energy for 2 Hz and 3 Hz. PSRV data are corrected for source and site effect terms. The corresponding model parameters are listed in Table 5.1.	118
5.4b	Plots of $\log_{10}(4\pi r^2 PSRV^2)$ versus distance and the corresponding fit to the Radiative Transfer Energy for 4 Hz and 6 Hz. PSRV data are corrected for source and site effect terms. The corresponding model parameters are listed in Table 5.1.	119
5.4c	Plots of $\log_{10}(4\pi r^2 PSRV^2)$ versus distance and the corresponding fit to the Radiative Transfer Energy for 8 Hz and 10 Hz. PSRV data is corrected for source and site effect terms. The corresponding model parameters are listed in Table 5.1.	120
5.4d	Plots of $\log_{10}(4\pi r^2 PSRV^2)$ versus distance and the corresponding fit to the Radiative Transfer Energy for 12 Hz and 16 Hz. PSRV data is corrected for source and site effect terms. The corresponding model parameters are listed in Table 5.1.	121
5.5	Values of Q_s^{-1} , Q_i^{-1} , and Q_t^{-1} predicted from the Radiative Transfer Energy for the Southern Great Basin are plotted versus frequency. Also shown is Q_c^{-1} . Notice that Q_c^{-1} and Q_t^{-1} are very close from 2 to 16 Hz.	126
5.6	Average coda envelope, Lg amplitude, and first S wave at 2 Hz and 16 Hz. Lg and S-wave amplitudes are coda normalized. For coda envelopes, time is lapse time in seismogram after origin time. For Lg and S waves amplitudes, time is travel time.	128

LIST OF ILLUSTRATIONS (continued)

FIGURE		PAGE
6.1	SV for YMT1 and YMT5 for the earthquake no. 39 of Table 1.1. Notice that SV at YMT1 is amplified ten times more than at YMT5 in the frequency range of 1-5 Hz..	132
6.2a	The residuals of the observed spectrum and the modeled spectrum averaged for all events recorded at YMT1 are shown here by the line denoted by small circles. Site amplification terms calculated from the regression of PSRV data are shown by long broken line. The solid line represents the site amplification terms using the coda method. The vertical scale is $\log_{10}(\text{amplification})$.	138
6.2b	The residuals of the observed spectrum and the modeled spectrum averaged for all events recorded at YMT2, YMT3, and YMT4 are shown here by the line denoted by small circles. Site amplification terms calculated from the regression of PSRV data are shown by long broken line. The solid line represents the site amplification terms using the coda method. The vertical scale is $\log_{10}(\text{amplification})$.	139
6.2c	The residuals of the observed spectrum and the modeled spectrum averaged for all events recorded at YMT5, YMT6, and TMBR are shown here by the line denoted by small circles. Site amplification terms calculated from the regression of PSRV data are shown by long broken line. The solid line represents the site amplification terms using the coda method. The vertical scale is $\log_{10}(\text{amplification})$.	140
6.2d	The residuals of the observed spectrum and the modeled spectrum averaged for all events recorded at AMR, APKW, and BGB are shown here by the line denoted by small circles. Site amplification terms calculated from the regression of PSRV data are shown by long broken line. The solid line represents the site amplification terms using the coda method. The vertical scale is $\log_{10}(\text{amplification})$.	141

LIST OF ILLUSTRATIONS (continued)

FIGURE		PAGE
6.2e	The residuals of the observed spectrum and the modeled spectrum averaged for all events recorded at BLT, BMTN, and CTS are shown here by the line denoted by small circles. Site amplification terms calculated from the regression of PSRV data are shown by long broken line. The solid line represents the site amplification terms using the coda method. The vertical scale is $\log_{10}(\text{amplification})$.	142
6.2f	The residuals of the observed spectrum and the modeled spectrum averaged for all events recorded at EPN, FMT, and GLR are shown here by the line denoted by small circles. Site amplification terms calculated from the regression of PSRV data are shown by long broken line. The solid line represents the site amplification terms using the coda method. The vertical scale is $\log_{10}(\text{amplification})$.	143
6.2g	The residuals of the observed spectrum and the modeled spectrum averaged for all events recorded at GMN, GMNH, and GVN are shown here by the line denoted by small circles. Site amplification terms calculated from the regression of PSRV data are shown by long broken line. The solid line represents the site amplification terms using the coda method. The vertical scale is $\log_{10}(\text{amplification})$.	144
6.2h	The residuals of the observed spectrum and the modeled spectrum averaged for all events recorded at GMR, GMRH, and GWV and YMT4 are shown here by the line denoted by small circles. Site amplification terms calculated from the regression of PSRV data are shown by long broken line. The solid line represents the site amplification terms using the coda method. The vertical scale is $\log_{10}(\text{amplification})$.	145

LIST OF ILLUSTRATIONS (continued)

FIGURE		PAGE
6.2i	The residuals of the observed spectrum and the modeled spectrum averaged for all events recorded at HCR, JON, and JONH are shown here by the line denoted by small circles. Site amplification terms calculated from the regression of PSRV data are shown by long broken line. The solid line represents the site amplification terms using the coda method. The vertical scale is $\log_{10}(\text{amplification})$.	146
6.2j	The residuals of the observed spectrum and the modeled spectrum averaged for all events recorded at KRNA, LCH, and LOP are shown here by the line denoted by small circles. Site amplification terms calculated from the regression of PSRV data are shown by long broken line. The solid line represents the site amplification terms using the coda method. The vertical scale is $\log_{10}(\text{amplification})$.	147
6.2k	The residuals of the observed spectrum and the modeled spectrum averaged for all events recorded at LSM, ELSM, and NLSM are shown here by the line denoted by small circles. Site amplification terms calculated from the regression of PSRV data are shown by long broken line. The solid line represents the site amplification terms using the coda method. The vertical scale is $\log_{10}(\text{amplification})$.	148
6.2l	The residuals of the observed spectrum and the modeled spectrum averaged for all events recorded at MCA, MCY, and MGM are shown here by the line denoted by small circles. Site amplification terms calculated from the regression of PSRV data are shown by long broken line. The solid line represents the site amplification terms using the coda method. The vertical scale is $\log_{10}(\text{amplification})$.	149

LIST OF ILLUSTRATIONS (continued)

FIGURE		PAGE
6.2m	The residuals of the observed spectrum and the modeled spectrum averaged for all events recorded at MZP, NPN, and PGE are shown here by the line denoted by small circles. Site amplification terms calculated from the regression of PSRV data are shown by long broken line. The solid line represents the site amplification terms using the coda method. The vertical scale is $\log_{10}(\text{amplification})$.	150
6.2n	The residuals of the observed spectrum and the modeled spectrum averaged for all events recorded at PPK, PRN, and QCS are shown here by the line denoted by small circles. Site amplification terms calculated from the regression of PSRV data are shown by long broken line. The solid line represents the site amplification terms using the coda method. The vertical scale is $\log_{10}(\text{amplification})$.	151
6.2o	The residuals of the observed spectrum and the modeled spectrum averaged for all events recorded at QSM, SDH, and SGV are shown here by the line denoted by small circles. Site amplification terms calculated from the regression of PSRV data are shown by long broken line. The solid line represents the site amplification terms using the coda method. The vertical scale is $\log_{10}(\text{amplification})$.	152
6.2p	The residuals of the observed spectrum and the modeled spectrum averaged for all events recorded at SPRG, SSP, and TCN are shown here by the line denoted by small circles. Site amplification terms calculated from the regression of PSRV data are shown by long broken line. The solid line represents the site amplification terms using the coda method. The vertical scale is $\log_{10}(\text{amplification})$.	153

LIST OF ILLUSTRATIONS (continued)

FIGURE		PAGE
6.2q	The residuals of the observed spectrum and the modeled spectrum averaged for all events recorded at TMO, WCT, and WRN are shown here by the line denoted by small circles. Site amplification terms calculated from the regression of PSRV data are shown by long broken line. The solid line represents the site amplification terms using the coda method. The vertical scale is $\log_{10}(\text{amplification})$.	154
6.3	Source terms of all the events used for the regression of SV data. The source terms are adjusted to be proportional to displacements. Notice that the corner frequencies are between 8 to 12 Hz and that the asymptotic zero frequency source terms vary more than two order of magnitudes.	156
6.4	Displacement spectrum of S waves (top). The observed spectrum of S waves is shown by long broken lines, the noise spectrum by the short dashed lines, and the modeled spectrum by the solid line. The difference between the observed and the modeled spectrum is shown in the bottom figure.	159
6.5	Average site amplification for frequencies 1 to 20 Hz for a group of stations located of Paleozoic carbonated rocks and for Tertiary Ash-Flow Tuff. Notice two opposite frequency trends for these two group of stations.	167

CHAPTER 1

INTRODUCTION

1.1 Statement of Problem

Attenuation of ground motion in seismology is of great importance for understanding source properties of distant seismic sources and also for predicting seismic ground motion of earthquakes of local and regional distances. The factors controlling earthquake ground motion are those related first to the source which includes size, depth, mechanism, and stress drop, second to properties related to propagation of seismic waves through the body of the earth, e.g., geometrical attenuation, dissipation of seismic energy due to anelastic properties of the earth, and scattering of elastic waves during propagation, and third to the effects of the local site. In the distance range of a few kilometers to a few hundred kilometers, the physics of propagation of the main ground motion, which carries most of elastic energy, can change. At distances less than 80 km, the main shear wave energy is carried by the direct S wave (Frankel, *et al.*, 1990). At distances of 150 to 1000 km, the dominant phase is the Lg phase, comprised of postcritical reflections of S waves trapped within the crustal wave guide (Bouchon, 1982; Kennett, 1985). Wave propagation in the distance range between 80 and 150 km is more complex and the exact

propagation mechanism is not well understood (Burger, *et al.*, 1987). Any attempt to understand the attenuation of ground motion has to deal with the question of separation of the geometrical spreading contribution to attenuation from intrinsic attenuation and scattering in the different distance ranges where the mechanism of propagation may change. Geometrical attenuation is usually assumed as a frequency independent operator in the overall wave propagation (Ou and Herrmann, 1990; Frankel *et al.*, 1990)

Waves can also experience scattering due to cracks, faults, and velocity heterogeneities of different scales within the crust. Scattering usually manifests itself as a frequency dependent factor which can present itself mathematically in a form similar to the absorption factor. Because scattering is not a net loss of elastic wave energy and only a redistribution of energy in space and time (Frankel, 1991; Toksöz *et al.*, 1988), a proper strategy that investigates elastic waves at different distances from the source and at different times should be able to account for the total energy and thus account for the degree of scattering and its contribution to the total apparent attenuation (Wu, 1985; Wu and Aki, 1988; Hoshiya, 1991; Frankel, 1991).

Local site effects can amplify or deamplify ground motion. Geology and the type of rocks or sediments around the site are controlling factors in evaluating the site factor (Su *et al.*, 1992; Mayeda

et al., 1992; Castro *et al.*, 1990; Phillips and Aki, 1986). It has been observed that younger and less consolidated sediments may amplify seismic waves several times more than hard rocks. At the same time, young sediments can attenuate waves near local sites. These competing factors are frequency dependent. Small magnitude and large magnitude earthquakes may present different site effects due to non-linear mechanical properties of some sediments in a high stress environment. The question of the site effect, its frequency dependence and amplification function is important in seismic hazard analysis.

In the area that this study is performed, the Southern Great Basin of Nevada and California, the dominant local site geology consists of sequences of very complex volcanic basalt and tuff of Tertiary age, in many places adjacent to Paleozoic limestone and dolomite. The porosity for these various rock types varies greatly. It is important to characterize the site effects for a network of seismic stations where non-welded tuff, welded tuff, bedded tuff, and non-bedded tuff exist. Yucca Mountain, the focus of our site study, has been designated as a storage site for radioactive waste storage. Here tuff may be found, close to many old carbonate rocks.

1.2 Geology of the Southern Great Basin

Basin-range structure consisting of alternating mountains and

valleys is best developed in the basin-and-range physiographic province that extends from southern Oregon and Idaho through most of Nevada and part of California, Utah, Arizona, and New Mexico. In the United States, the province is about 500 to 800 km across in the Great Basin region of Nevada and in western Utah. The elevations of the valleys in the Great Basin are generally 1,300 to 1,600 m, whereas mountain crests are 2,000 to 3,000 m and locally about 3,600 m. The crust of the basin-and-range province is different from that of most continental crust by being thinner, warmer and highly fractured. The southern Great Basin of Nevada and California form the southern part of the Great Basin of the basin-and-range province. High-angle extensional faulting extends throughout much of the province. The province is notable for its broadly distributed normal faulting. With the exception of the northern part of the east African rift system, it is unusual among continental regions by having high heat flow, a thin lithosphere, the occurrence of low seismic velocities in the underlying upper mantle, and a history of long-lived episodic magmatism (Eaton, 1982). It is a full-scale model of the predrift-rifting of continental lithosphere, but one in which rifting is broadly distributed, more like a marginal back-arc basin than a spreading ocean ridge (Eaton, 1982). The southern Great Basin in the Nevada test site region (Carr, 1990) exhibits diverse structural trends, styles, and tectonic activity.

Compressional tectonism during the Mesozoic created a structural grain of thrust faults and folds. Granitic rocks are the only rocks of Mesozoic age in the region (Carr, 1990). Much of the Mesozoic structure is buried under volcanic rocks, mostly Miocene in age, that are more than 5 km thick in caldera areas (Carr, 1990). Voluminous silicic tuff and lava eruptions occurred from about 16 Ma to 10 Ma, forming a complex of overlapping calderas concentrated in a major volcano-tectonic rift. Volcanism and tectonism abruptly declined about 10 Ma ago, in all but the southwestern part of the region. This decline was accompanied by the first significant basaltic volcanism about 10 Ma ago. The last silicic eruptions in the region occurred about 5 Ma ago, but basaltic activity continued into the Quaternary (Carr, 1990).

The majority of the stations used in this study are in The Nevada Test Site, NTS, situated near the center of the Southern Great Basin. Up to 3000m of Rhyolitic tuffs cover many parts of NTS from the eruption of the Timber Mountain-Oasis Valley caldera complex in late the Tertiary (16-9 m.y.) (Hagstrum *et al.*, 1980). NTS consists primarily of volcanic rocks which are mainly ash-flow tuffs. The ash-flow tuff and bedded tuff sequence at NTS comprises a complex sequence of variously welded tuffs with super-imposed crystallization and altered zones.

1.3 Seismicity of the Nevada Test Site

Rogers *et al.* (1987) and Gomberg (1991) studied the seismicity of the region surrounding to the Southern Great Basin Seismic Network (SGBSN) region. In summary, the following features were identified for the Nevada Test Site region and surroundings:

1. A relatively large number of earthquakes occur in the southern and eastern portions of the Nevada Test Site, and to a lesser extent west of the Bear Mountain fault. The northern Nevada Test Site also has numerous small earthquakes, but these are thought to be caused by non-tectonic processes related to the nuclear testing done in this part of NTS.
2. A "gap" (lack of seismicity) is centered at Yucca Mountain.
3. A considerable number of events in the SGBSN catalog cannot be correlated with mapped faults.
4. The region where recent deformation appears to be greatest, to the west of the Death Valley/Furnace Creek fault system, has few small earthquakes
5. Clusters of earthquakes exist at all magnitudes at the northern end of the Furnace Creek fault and in the Pahrangat Shear Zone. These clusters cover areas much larger than the surface projections of any of the mapped faults.

Figure 1.1 shows a map of the area of study, the Southern Great Basin of Nevada and California, the seismic network used, SGBSN, and the location of the earthquake used for the study. Table 1.1 lists origin times, locations, depths, and magnitudes of events used. The event locations and magnitudes are from Harmsen and Rogers (1987). Figure 1.2 shows a histogram of the number of observations from 0 to 200 km grouped in 10 km windows.

1.4 Thickness of the crust at the Nevada Test Site

The crust of the Great Basin is everywhere less than 30 km thick (Eaton, 1982). Locally the crust is as thin as 20 km. All geophysical investigations including seismicity, gravity anomalies, and heat flow studies support an unusually thin crust throughout most of the Great Basin. Taylor (1983), studied the three-dimensional crust and upper mantle velocity structure at the Nevada Test Site. He found that the velocity structure derived by examining P-wave travel time residuals, shows that the crust is generally thinner than 32 km. Strong lateral variations of the crust at shallow depths are observed which are mainly due to strongly layered structures consisting of Tertiary volcanic and late Tertiary and Quaternary alluvium on top of the Paleozoic sedimentary rocks with varying thickness throughout the NTS (Taylor, 1983).

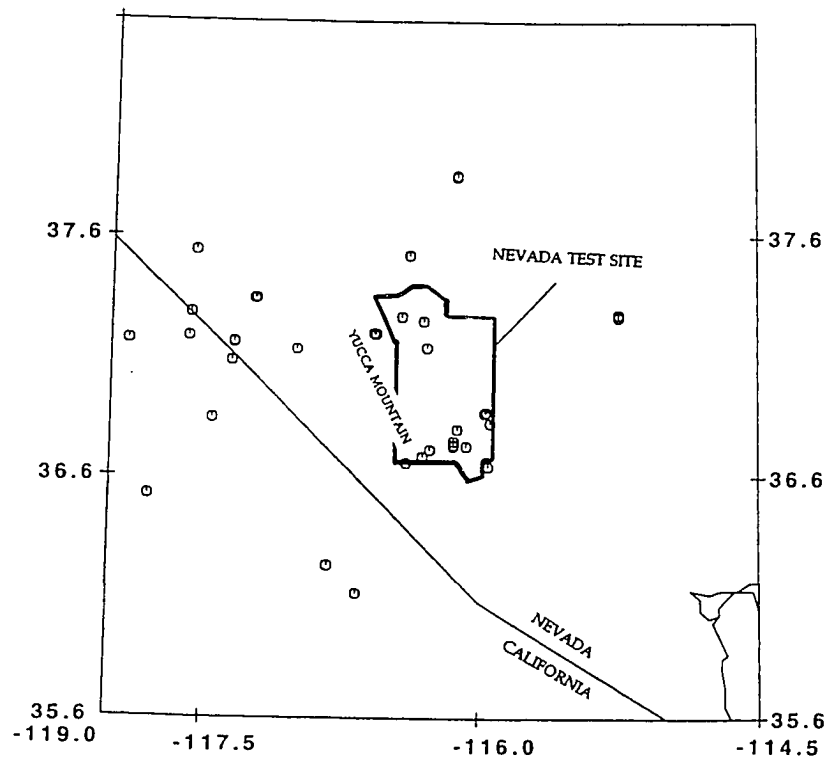


Figure 1.1. Earthquakes recorded on the Southern Great Basin Seismic Network, SGBSN, used for this study.

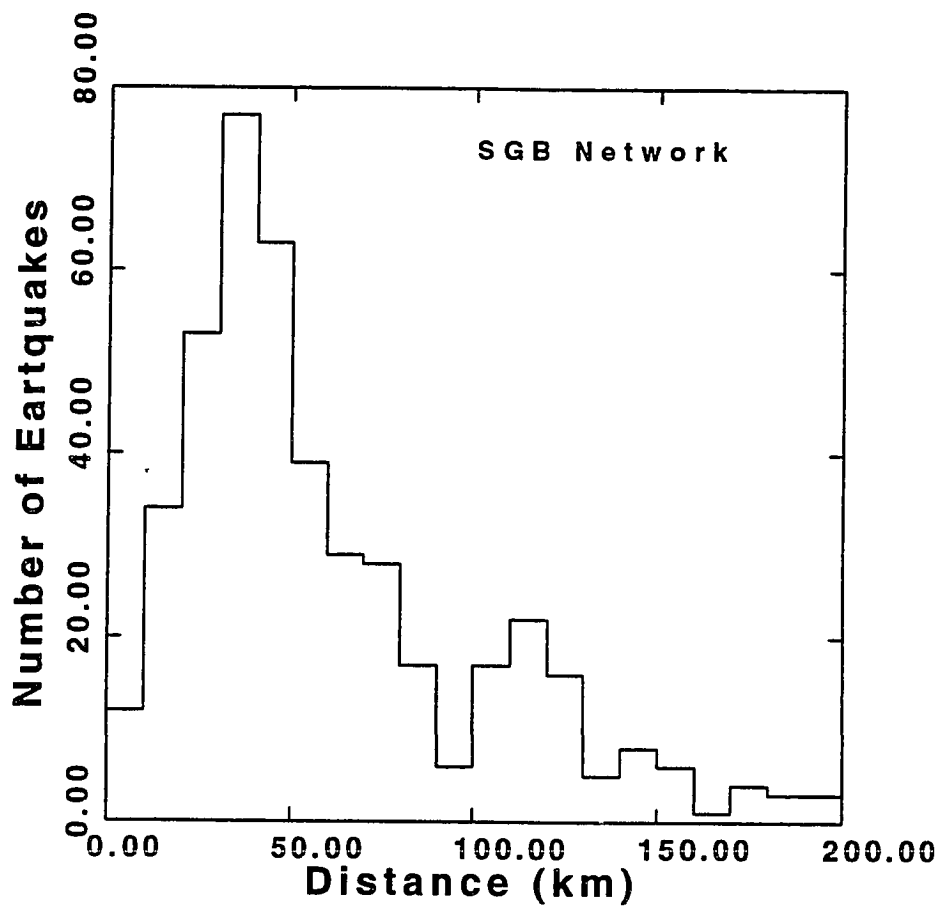


Figure 1.2. Histogram of observed records. The vertical axis is the number of observations for every 10 km of epicentral distance, while the horizontal axis is the epicentral distance.

TABLE 1.1 List of the Southern Great Basin Earthquakes

No	ORIGIN TIME (Yr Mon Day Hr Min Sec)	LAT (° N)	LON (° W)	DEPTH (km)	m_bL_g
1	1986 3 20 11 13 02.01	37.265	115.250	10.3	1.5
2	1986 3 25 18 00 51.11	37.346	117.235	0.1	1.8
3	1986 3 29 16 43 40.13	37.166	117.352	9.5	1.3
4	1986 3 30 10 46 28.94	36.871	115.971	0.0	0.9
5	1986 3 31 08 11 30.83	37.142	116.294	8.6	1.7
6	1986 3 31 21 53 33.09	36.648	115.950	14.8	1.7
7	1986 4 08 23 33 46.86	37.135	117.001	8.7	1.3
8	1986 4 09 05 27 32.21	37.345	117.241	0.2	2.0
9	1986 4 09 08 54 27.63	36.689	116.316	3.7	1.0
10	1986 4 09 08 59 42.71	36.687	116.314	4.8	1.1
11	1986 4 14 03 00 18.01	36.870	115.977	5.3	1.0
12	1986 4 14 05 48 18.31	37.162	117.354	8.9	2.2
13	1986 4 15 03 58 12.14	37.853	116.133	0.5	1.7
14	1986 4 17 19 36 59.02	36.734	116.144	0.5	1.2
15	1986 4 17 23 06 38.63	36.119	116.672	8.3	1.6
16	1986 4 18 09 06 39.26	36.739	116.145	0.2	1.0
17	1986 4 19 02 44 00.87	36.521	117.808	9.8	2.2
18	1986 4 19 10 28 63.53	36.875	115.967	0.0	1.0
19	1986 4 20 09 28 50.81	36.236	116.826	9.4	1.4
20	1986 4 20 11 19 44.35	37.271	115.256	8.0	1.2
21	1986 4 21 17 14 58.18	36.847	117.463	5.6	1.7
22	1986 4 23 16 57 28.18	36.733	116.075	0.1	1.1
23	1986 4 27 14 23 32.62	37.542	117.569	0.2	1.2
24	1986 4 28 05 15 16.26	37.199	116.578	4.2	1.6
25	1986 4 28 15 52 43.82	37.169	117.916	5.0	2.0
26	1986 5 01 03 05 24.57	37.285	117.589	8.1	1.5
27	1986 5 01 06 45 58.99	37.086	117.360	1.9	1.2
28	1986 5 02 05 59 29.86	37.201	116.589	6.9	1.0
29	1986 5 10 13 14 38.98	37.270	116.430	0.9	1.6
30	1986 5 14 01 36 56.46	37.252	116.312	0.1	1.7
31	1986 5 14 14 30 58.21	37.282	115.255	0.5	2.2
32	1986 5 16 03 39 31.27	37.186	117.597	10.1	1.1
33	1986 5 16 21 00 06.44	36.823	115.935	11.8	1.0
34	1986 5 16 21 02 53.14	36.828	115.942	9.1	1.0
35	1986 5 17 02 06 45.99	37.347	117.232	1.4	1.2
36	1986 5 20 18 52 30.65	37.525	116.397	15.3	1.7
37	1986 5 21 13 18 61.28	36.753	116.145	0.0	0.9
38	1986 5 27 14 38 51.86	36.662	116.406	8.4	0.9
39	1986 5 27 15 42 46.38	37.860	116.136	0.7	1.8
40	1986 5 28 13 15 15.79	37.854	116.133	0.5	1.8
41	1986 5 28 17 27 11.84	37.854	116.132	0.6	1.5

CHAPTER 2
RESTITUTION OF GROUND MOTION
RECURSIVE DECONVOLUTION FILTERS

2.1 Introduction

The recovery of true ground motion from seismograms in terms of displacement, velocity, or acceleration is known as the restitution problem in seismology.

For many studies, it is necessary to remove the instrument effect from the seismogram to obtain the true ground motion. This can be done in two ways. For most applications, the complex spectrum at a particular frequency is divided by the instrument response at that frequency. This is called frequency domain removal. Next the spectrum is transformed to the time domain to yield a time series. This method has its advantages and disadvantages. The advantages are that it is symbolically and mathematically rather simple and in principal can be done for any set of instruments as long as the mathematical form of response is known as a function of frequency. The primary disadvantage is that for a long time series there will be a problem of processing and storing long time series.

Another problem which often arises is the instability of division by the instrument response which usually tends to zero at low and high frequencies. For these reasons time domain recursive deconvolution of the instrument becomes attractive. In summary, calculations are done using difference equations and instabilities can be avoided without paying a serious price.

2.2 Recursive Filter Method

The transfer function of a seismograph system is often described in analog form with its Laplace transform as:

$$H(s) = \frac{\prod_{i=1}^m A_i(s)}{\prod_{i=1}^n B_i(s)} = \frac{Y(s)}{X(s)} \quad (2.1)$$

where $A_i(s)$ and $B_i(s)$ are linear or quadratic polynomials and usually $n > m$. Therefore, the ground motion $X(s)$, is related to the recorded motion, $Y(s)$, by the relation

$$Y(s) = X(s) H(s). \quad (2.2)$$

The inverse transfer function of the seismograph system, $H^{-1}(s)$, is defined as

$$H^{-1}(s) = \frac{\prod_{i=1}^n B_i(s)}{\prod_{i=1}^m A_i(s)} \quad (2.3)$$

$H^{-1}(s)$ is system transfer function in itself and is equal to the ratio of $X(s)$ to $Y(s)$,

$$\frac{X(s)}{Y(s)} = \frac{\prod_{i=1}^n B_i(s)}{\prod_{i=1}^m A_i(s)}. \quad (2.4)$$

This formulation represents a continuous process in time. To be able to evaluate these quantities in digital processing, we introduce the z-transform, in which we transform the analogue s argument to the digital variable z through the bilinear transform (Oppenheim and Schaffer, 1975). The meaning of the z variable is illustrated by the definition of the z-transform. Given a continuous function $h(t)$ sampled at equal time intervals T , the z-transform, $H(z)$, is defined as:

$$H(z) = \sum_{n=-\infty}^{\infty} h(nT) z^{-n} \quad (2.5)$$

To convert a causal filter, represented by a rational polynomial in s , into a digital filter, we can use either a bilinear or an impulse invariant transformation. We will use the bilinear transformation which introduces the substitution

$$s \rightarrow \frac{2}{T} \frac{1 - z^{-1}}{1 + z^{-1}}. \quad (2.6)$$

This mapping has the property that the imaginary axis in the s -plane maps onto the unit circle. To demonstrate this, substitute $z =$

$e^{j\omega T}$, where ω is the digital frequency, into (2.6). Then

$$\begin{aligned}
 s &= \frac{2}{T} \frac{1 - e^{-j\omega T}}{1 + e^{j\omega T}} & (2.7) \\
 &= \frac{2}{T} \frac{j \sin\left(\frac{\omega T}{2}\right)}{\cos\left(\frac{\omega T}{2}\right)} \\
 &= \frac{2}{T} j \tan\left(\frac{\omega T}{2}\right) = \sigma + j \Omega.
 \end{aligned}$$

Thus for z on the unit circle, ω is real, and $\sigma = 0$. Ω and ω are related by:

$$\bullet \quad \Omega = \frac{2}{T} \tan\left(\frac{\omega T}{2}\right) \quad (2.8)$$

ω and Ω are digital and analog frequencies, respectively.

$$\omega = \frac{2}{T} \tan^{-1}\left(\frac{\Omega T}{2}\right) \quad (2.9)$$

The positive and negative imaginary axis of the s -plane are mapped, respectively, into the upper and lower halves of the unit circle in the z -plane. Also, the left half of the s -plane, where complex singularities yield causal time histories, maps to the inside of the unit circle, and the right half of the s -plane maps to the outside of the unit circle. The problem that arises in this transformation is

the clear non-linear relationship between frequencies. This phenomenon, the distortion in the frequency axis, is known as frequency warping. The usefulness of this digital filter is acceptable as long as this distortion can be tolerated or compensated. If the critical frequencies of the analog filter are prewarped using (2.8), when the analog filter is transformed to a digital filter through the bilinear transformation, then the digital filter will meet the desired specifications.

2.3. Southern Great Basin Seismic Network

Table 2.2 describes station codes, locations, and types of instrumentation of the Southern Great Basin Seismic Network, SGBSN, used in this study (Harmsen and Rogers, 1987). The locations are shown in Figure 2.1. There are four different seismograph instrument systems used, L4C-vertical, L4C-horizontal, S13-O, and S13-Y systems. The transfer function describing seismometer output voltage as a function of ground displacement in meters for these instruments is given by

$$H_{\text{seis}} = 409.6 G_{\text{le}} \frac{s^3}{s^2 + 2h\omega_n s + \omega_n^2}.$$

Table 2.1 shows the values of the effective loaded motor constants, G_{le} , the seismometer natural frequencies, f_n in $\omega_n = 2\pi f_n$, and the damping coefficient, h , for these instruments (Rogers, *et al.*, 1987).

TABLE 2.1 SGB network station parameters.

STATION NAME	LATITUDE DEG-MIN	LONGITUDE DEG-MIN	INSTRUMENT TYPE ⁽¹⁾	GAIN DB
NOP	36 07.68	116 09.16W	2	84
JON	36 26.39	116 06.18W	1	84
WRN	37 58.90	115 35.30W	1	84
JONH	36 26.39	116 06.18W	4	78
SDH	36 38.73	116 20.29W	1	84
AMR	36 23.86	116 28.45W	1	84
GWV	36 11.20	116 40.24W	1	84
WCT	36 47.53	116 37.60W	1	84
TCN	37 08.63	116 43.27W	1	84
PGE	36 20.93	117 03.95W	1	84
PGEH	36 20.93	117 03.95W	4	78
GVN	37 00.09	117 20.55W	1	84
TMO	36 48.32	117 24.48W	1	84
TMBR	37 02.05	116 23.13W	1	84
SGV	36 58.87	117 01.94W	2	84
QSM	35 57.93	116 52.10W	1	84
FMT	36 38.38	116 46.73W	1	84
MCA	36 38.89	117 16.85W	1	84
SSP	36 55.50	116 13.11W	1	84
HEPN	37 12.85	116 19.42W	4	60
EPN	37 12.85	116 19.42W	1	84
BGB	37 02.27	116 13.66W	1	84
GLR	37 11.96	116 01.06W	1	84
MCY	36 39.70	115 57.73W	2	84
LOP	36 51.25	116 10.05W	1	84
GMR	37 20.03	115 46.27W	1	84
GMRH	37 20.03	115 46.27W	1	84
EPR	37 10.12	115 11.19W	1	84
PRN	37 24.42	115 02.99W	2	84
PRNH	37 24.42	115 02.99W	4	78
APK	36 19.17	115 34.46W	1	84
APKW	36 19.19	115 35.22W	1	84
LSM	36 44.40	116 16.37W	2	84

TABLE 2.1 Continued

STATION NAME	LATITUDE DEG-MIN	LONGITUDE DEG-MIN	INSTRUMENT TYPE ⁽¹⁾	GAIN DB
CPX	36 55.80	116 03.33W	1	84
KRNA	37 44.47	116 22.80W	1	84
BLT	37 28.93	116 07.35W	1	84
SHRG	36 30.27	115 09.31W	1	84
SPRG	36 41.64	115 48.56W	1	84
QCS	37 46.07	115 54.98W	1	84
CTS	37 39.40	116 43.54W	1	84
SRG	37 52.93	115 04.08W	1	84
MTI	37 40.60	115 16.36W	1	84
TPU	37 36.30	115 38.95W	1	84
NPN	37 39.16	114 56.22W	1	84
HCR	38 14.02	116 26.18W	1	84
MZP	37 42.04	117 22.98W	1	84
GMN	37 18.01	117 15.58W	1	84
GMNH	37 18.01	117 15.58W	4	78
LCH	37 14.08	117 38.84W	1	84
MGM	37 26.47	117 29.79W	1	84
SVP	37 42.90	117 48.05W	1	84
PPK	37 25.58	117 54.43W	1	84
CDH1	36 51.62	116 19.05W	1	84
CDH5	36 51.62	116 19.05W	1	108
BMT	37 17.01	116 38.74W	1	84
BMTN	37 17.35	116 38.43W	1	84
YMT1	36 51.20	116 31.80W	3	84
YMT2	36 47.12	116 29.19W	3	84
YMT3	36 47.23	116 24.79W	3	84
YMT4	36 50.83	116 27.07W	3	84
YMT5	36 53.90	116 27.23W	3	84
YMT6	36 51.51	116 24.26W	3	84
ELSM	36 44.40	11616.37W	4	60
NLSM	36 44.40	11616.37W	4	60

(1) Instrument Type = 1 is for L4C-Vertical
Instrument Type = 2 is for L4C-Horizontal
Instrument Type = 3 is for S13-O
Instrument Type = 4 is for S13-Y.

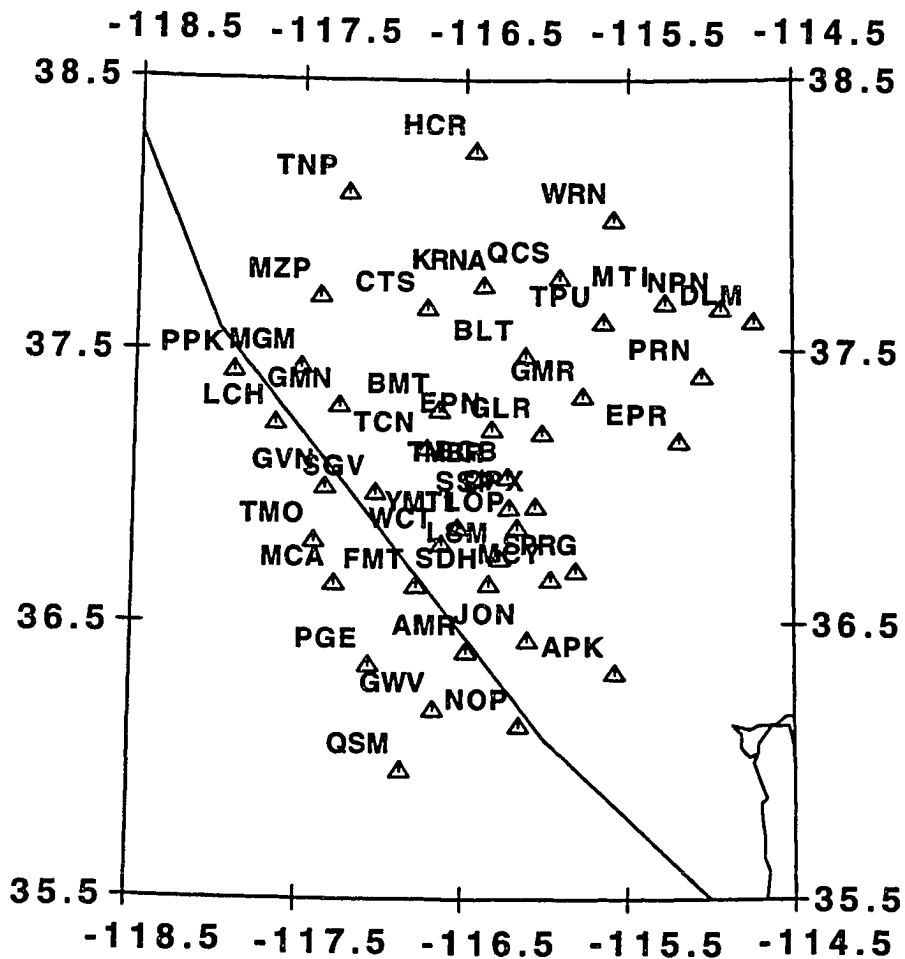


Figure 2.1. Map of the SGBSN between the border of Nevada and California. Location of the stations are shown by open triangles.

TABLE 2.2
Constant values of SGB Instruments

Seismometer Type	G_{le} <u>volts-sec</u> meter	f_n Hz	h (Damping)
L4C-Vertical	126.5	1.0	0.355
L4C-Horizontal	126.5	1.0	0.355
S13-O	377.8	1.0	0.35
S13-Y	368.0	1.0	0.365

The voltage output of the seismometers is input into an amplifier and from there into a vco/discriminator. The analog signal then is converted into digital counts through a digital converter, the PDP AD11K. The frequency response of the digital converter is flat for input signals having frequencies between 0 to 52 Hz. 52 Hz is the Nyquist frequency. The system output is in digital counts, such that 1 volt input to the AD11K results in 409.6 counts output for all frequencies below the Nyquist frequency. The frequency response of the amplifiers and the vco/discriminators used are as follows:

Tricom 649 Amplifiers The analogue response of the Tricom 649 amplifier is modeled using a second-order Bessel low pass filter cascaded with a third-order Butterworth high pass filter. Letting $H_l(s)$ =the low pass filter, and $H_h(s)$ =the high pass filter, the transfer

function, $H_1(s)$ is written as

$$H_1(s) = 10^{g/20} H_l(s)H_h(s) ,$$

where, g = amplifier gain (dB),

$$H_l(s) = \frac{\omega_1^2}{s^2 + 2h\omega_1 + \omega_1^2} ,$$

where $\omega_1 = 128.076$ and $h_1 = 0.0.866$, and

$$H_h(s) = \frac{s^2}{(s^2 + 2h_2\omega_2 + \omega_2^2)} \cdot \frac{s}{(s + \omega_3)} ,$$

where $h_2 = 0.5, \omega_2 = 6.283$, and $\omega_3 = 6.283$.

Tricom 642 Discriminator This is a fifth order Bessel low pass filter.

This filter can be represented as product of one first-order and two second-order filters.

$$H_2(s) = \frac{\omega_1}{s + \omega_1} \cdot \prod_{i=2}^3 \frac{\omega_i^2}{s^2 + 2h_i\omega_i s + \omega_i^2} ,$$

where $\omega_1 = 142.9, \omega_2 = 161.2, \omega_3 = 137.9, h_2 = 0.8875$, and $h_3 = 0.5455$.

Geotech 4250 Amplifier This amplifier is a second-order low pass Bessel filter, $H_l(s)$, cascaded with a second-order high pass Butterworth filter, $H_h(s)$,

$$H_3(s) = 10^{g/20} H_l(s)H_h(s) ,$$

where, g = amplifier gain (dB) and

$$H_1(s) = \frac{\omega_1^2}{s^2 + 2h_1\omega_1s + \omega_1^2},$$

where $\omega_1 = 160.1$, and $h_1 = 0.886$, and

$$H_h(s) = \frac{s^2}{s^2 + 2h_2\omega_2s + \omega_2^2},$$

where $\omega_2 = 1.257$, and $h_2 = 0.707$.

Geotech 4612 Discriminator This is a third-order Paynter low pass filter given by

$$H_4(s) = \frac{\omega_1^2}{s^2 + 2h_1\omega_1s + \omega_1^2} \cdot \frac{\omega_2}{s + \omega_2},$$

where $\omega_1 = 170.494$, $\omega_2 = 162.86$, and $h_1 = 0.6015$.

SGB Seismograph System

The complex frequency response of the entire system as a function of analogue frequency s , $H(s)$, may be described by

$H(s) = 409.6 H_{\text{seis}}(s) H_1(s) H_2(s)$ for the L4C-vertical system,

$H(s) = 409.6 H_{\text{seis}}(s) H_4(s) H_5(s)$ for the L4C-horizontal system,

$H(s) = 409.6 H_{\text{seis}}(s) H_1(s) H_2(s)$ for the S13-O system, and

$H(s) = 409.6 H_{\text{seis}}(s) H_3(s) H_4(s)$ for the S13-Y system, where the

parameters G_{1e} and h are chosen for the proper seismometer from

Table 2.2.

2.4 Inverse filters, deconvolution

By simple algebraic transformation the overall transfer function can be written as a product of low-pass filters, high-pass filters, s^n where n is an integer, and a constant A . That transfer function is

$$H(s) = A s^n H_L H_H, \quad (2.10)$$

where

$$H_L = \prod_{j=1}^m \left(\frac{\omega_j^2}{s^2 + 2h_j \omega_j s + \omega_j^2} \right) \prod_{k=1}^n \left(\frac{\omega_k}{s + \omega_k} \right)$$

and

$$H_H = \prod_{j=1}^k \frac{s^2}{s^2 + 2h_j \omega_j s + \omega_j^2}.$$

(2.10) can be further written as

$$H(s) = \frac{s^M}{P_N(s)} \quad (2.11)$$

where $P_N(s)$ is a polynomial of order N in s . The inverse transfer function of SGB can be represented by

$$H^{-1}(s) = \frac{P_N(s)}{s^M}, \quad (2.12)$$

and in z -domain this equation is

$$H^{-1}(z) = \frac{Q_N(z)}{(z-1)^M (z+1)^N}, \quad (2.13)$$

where $P_N(s)$ and $Q_N(z)$ are polynomials of order N in s and z respectively, $N = 9$ to 12 and $M = 5$ to 6 depending on the

particular system considered. Instability arises at $s = 0$ and $s = \infty$ in (2.12) which correspond to $z=1$ and $z=-1$ in (2.13) respectively. The region of convergence in the z -plane is located outside a circle with radius one, centered at the origin. This means that, for a stable system, the region of convergence should include the unit circle and entire z -plane outside the unit circle. Therefore, all poles of the system function must lie inside the unit circle in the z -plane, if a stable system is required. Therefore, all poles must be located in the left half of the s -plane. This can be done by the substitutions

$$\frac{1}{1 - z^{-1}} \rightarrow \frac{1 - z}{(1 - \xi z^{-1})(1 - \xi z)} \quad |\xi| < 1 \quad (2.14)$$

and

$$\frac{1}{1 + z^{-1}} \rightarrow \frac{1 + z}{(1 + \xi z^{-1})(1 + \xi z)} \quad |\xi| < 1 \quad (2.15)$$

(Farber, 1989). These substitutions, which are equivalent to a high pass filter and a low pass filter, respectively, not only move the poles on the unit circle into the unit circle in the z plane, but also preserve the phase. The inverse filter of the transfer function, H^{-1} can be approximated by the effective inverse function

$$H_{\text{eff}}^{-1} = H_{\text{hp}} H^{-1} H_{\text{lp}}.$$

If $\xi \ll 1$, H_{eff}^{-1} will not closely approximate H^{-1} . In Figure 2.2 we show a time history of an input pulse, $\delta(t)$ and $H_{\text{eff}}^{-1} H \delta(t)$ for $\xi = 0.95$ and $\xi = 0.98$. We will show that $\xi = 0.98$ results in satisfac-

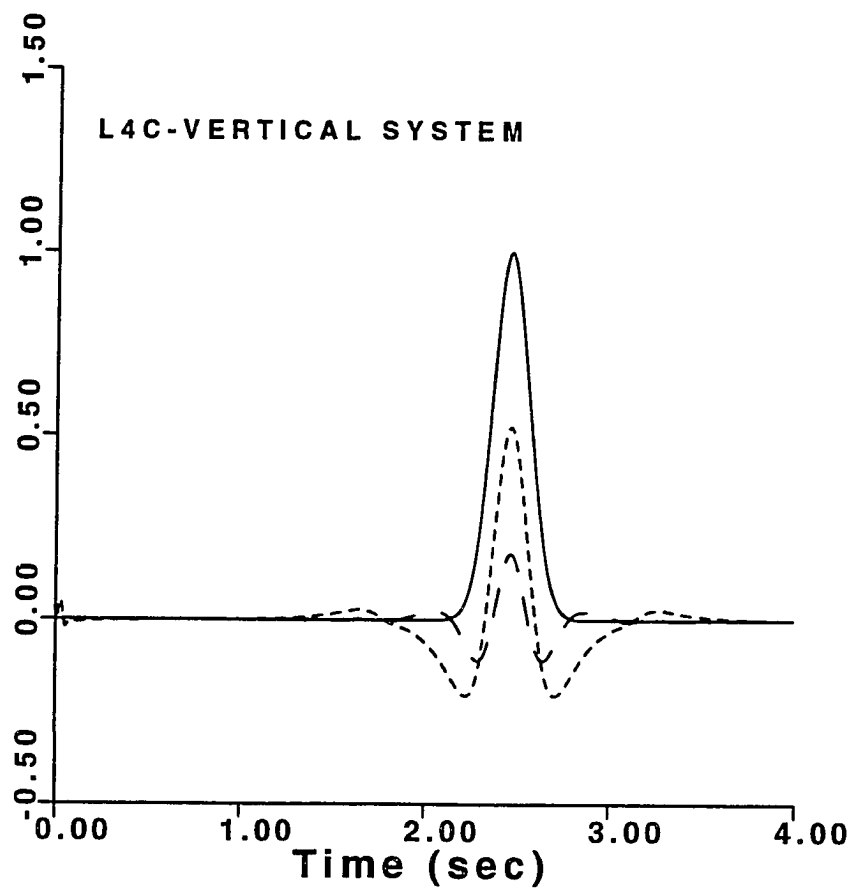


Figure 2.2. An impulse time function, shown by the solid line, is input into the recursive instrument system of L4C-V and the output is input into the inverse deconvolution filter of the same instrument system. The long dashed line is the output for $\xi = 0.94$ while the short dashed line shows the output for $\xi = 0.98$.

tory results for all four seismograph systems. For purposes of computation a filter operation of $\frac{1}{1 + \xi z^{-1}}$ if it is applied in a backward recursion on a time series is equivalent to the filter operation of $\frac{1}{1 + \xi z}$. These forward and backward recursions result in non-causal impulse response (Marschall, 1984). It will be shown, however, that the phase of the inverse filter will not be altered because of this stabilizing technique.

Inverse Digital Filter for Second-Order High-Pass Filter

The Laplace transform of the transfer function of a high-pass filter can be written as

$$H(s) = \frac{s^2}{s^2 + 2h\omega s + \omega^2}.$$

Using the bilinear z-transform

$$s = \frac{2}{T} \frac{1 - z^{-1}}{1 + z^{-1}}$$

and frequency prewarping

$$\omega' = \tan\left(\frac{\omega T}{2}\right) \quad (2.16)$$

$H^{-1}(s)$ will transform to

$$H^{-1}(z) = \frac{\alpha_0 + \alpha_1 z^{-1} + \alpha^2 z^{-2}}{(1 - z^{-1})^2} \quad (2.17)$$

with

$$\alpha_0 = 1 + 2h\omega' + \omega'^2$$

$$\alpha_1 = 2(\omega'^2 - 1)$$

$$\text{and } \alpha_2 = 1 - 2h\omega' + \omega'^2$$

substituting

$$\frac{1-z}{(1-\xi z^{-1})(1-\xi z)} \text{ for } \frac{1}{(1-z^{-1})}$$

yields a stable inverse filter.

Inverse Digital Filter for Second-Order Low-Pass Filter

For a low-pass transfer function

$$H(s) = \frac{\omega^2}{s^2 + 2h\omega s + \omega^2} \quad (2.18)$$

a stable inverse filter arises by using a bilinear transformation and frequency prewarping and the substitution

$$\frac{1}{(1+z^{-1})^2} \rightarrow \frac{z}{(1+\xi z^{-1})(1+\xi z)}. \quad (2.19)$$

Substituting (2.18) into (2.19), the zero-phase inverse digital filter of the low-pass function is given by the following two-sided recursive filter

$$H^{-1}(s) = \frac{1}{a_0} \cdot \frac{z + a_1 + a_2 z^{-1}}{(1 + \xi z^{-1})(1 + \xi z)}, \quad \xi < 1, \quad (2.20)$$

where a_0 , a_1 , and a_2 are given by

$$a_0 = \frac{\omega'^2}{1 + 2h\omega' + \omega'^2}$$

$$a_1 = \frac{2(\omega'^2 - 1)}{1 + 2h\omega' + \omega'^2}$$

$$a_2 = \frac{1 - 2h\omega' + \omega'^2}{1 + 2h\omega' + \omega'^2}$$

$$\omega' = \tan\left(\frac{\omega T}{2}\right).$$

Another approach is to design a shaping filter with an f_b near the Nyquist frequency and a damping factor constant $h \approx 1.0$ to simulate the second order low-pass filter in (2.18). The inverse of the low-pass filter is shaped into this filter. The simulation process eliminates instability inherent in the inverse problem of the low-pass filter (Seidl, 1980). If b_0 , b_1 , and b_2 represent the coefficients of the low-pass simulating filter, the zero-phase equivalent of the inverse low-pass filter is given by

$$H^{-1}(s) = \frac{\alpha_0}{b_0^2} \frac{(1+b_1z^{-1}+b_2z^{-2})(1+b_1z+b_2z^{-2})}{(z^2+c_1z+c_0+c_1z^{-1}+c_2z^{-2})} \quad (2.21)$$

with

$$b_0 = \frac{\omega_b'^2}{1 + 2h_b \omega_b' + \omega_b'^2}$$

$$b_1 = \frac{2(\omega_b'^2 - 1)}{1 + 2h_b \omega_b' + \omega_b'^2}$$

$$b_2 = \frac{1 - 2h_b \omega_b' + \omega_b'^2}{1 + 2h_b \omega_b' + \omega_b'^2}$$

$$\omega_b' = \tan\left(\frac{\omega_b T}{2}\right)$$

$$c_0 = 2 + \alpha_1, \quad c_1 = 1 + 2\alpha_1 + \alpha_2$$

$$c_2 = \alpha_1 + 2\alpha_2, \quad c_3 = \alpha_3$$

Inverse Digital Filter of a Differentiator

The Laplace transform operator for the n'th derivative is

$$H(s) = s^n . \quad (2.22)$$

With the bilinear transformation this will become

$$H^{-1}(z) = \left(\frac{T}{2}\right)^n \left(\frac{1+z^{-1}}{1-z^{-1}}\right)^n .$$

A stable zero-phase, two-sided recursive filter for this can be achieved by substitutions

$$\frac{1}{(1-z^{-1})} \rightarrow \frac{(1-z)}{(1-\xi z^{-1})(1-\xi z)}$$

or

$$H^{-1}(z) = \left(\frac{T}{2}\right)^n \frac{(1-z)^n (1+z^{-1})^n}{(1-\xi z^{-1})^n} (1-\xi z)^n \quad (2.23)$$

This again can be viewed as cascades of forward as well as backward recursions.

2.5 Application of zero-phasing inverse filter to SGB system

The parameters used for the deconvolution filter are natural frequency 44 Hz with damping $h_b = 0.9$ for the low-pass zero-phasing shaping system, and $\xi = 0.98$. Figures 2.3 - 2.6 show the transfer functions of the original (solid curves) system as well as those derived which have a stable inverse (dashed lines). The difference between the real response function and the one obtained

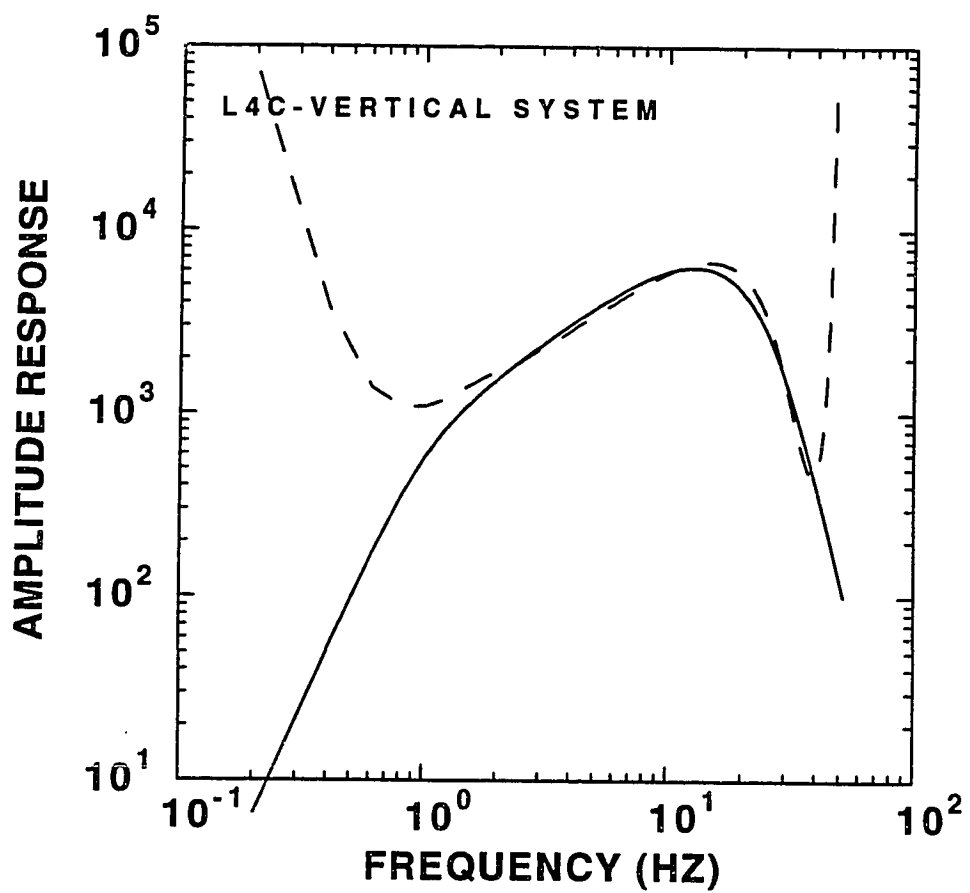


Figure 2.3. Transfer function amplitude versus frequency for the L4C-vertical system. The solid line is the analog amplitude, the dashed line is the amplitude response calculated from the inverse recursive filter.

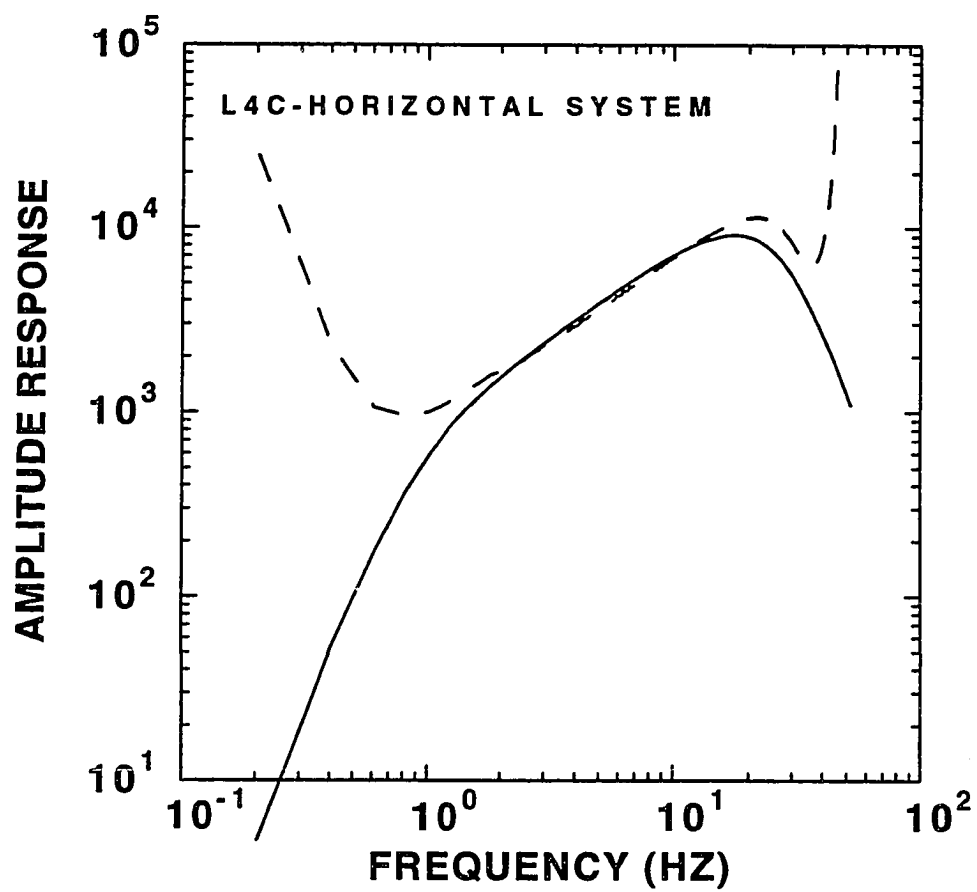


Figure 2.4. Same as Figure 2.3 but for the L4C-horizontal system.

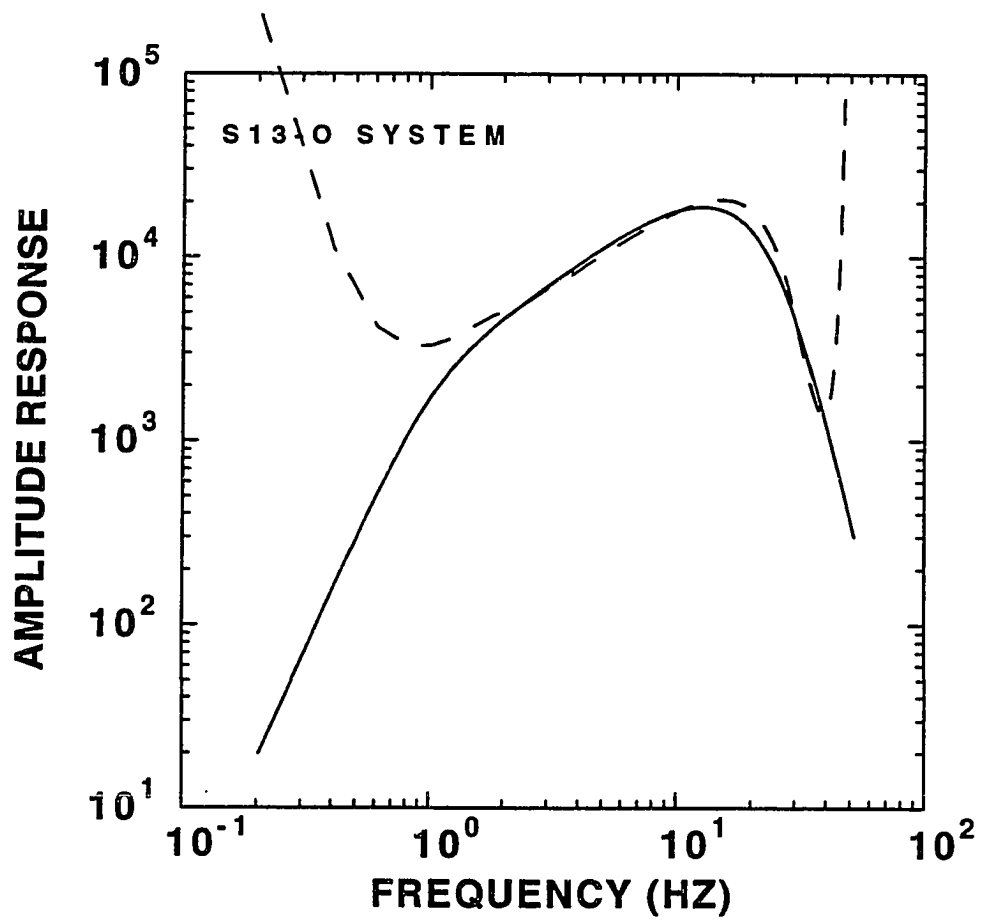


Figure 2.5. Same as Figure 2.3 but for the S13-O system.

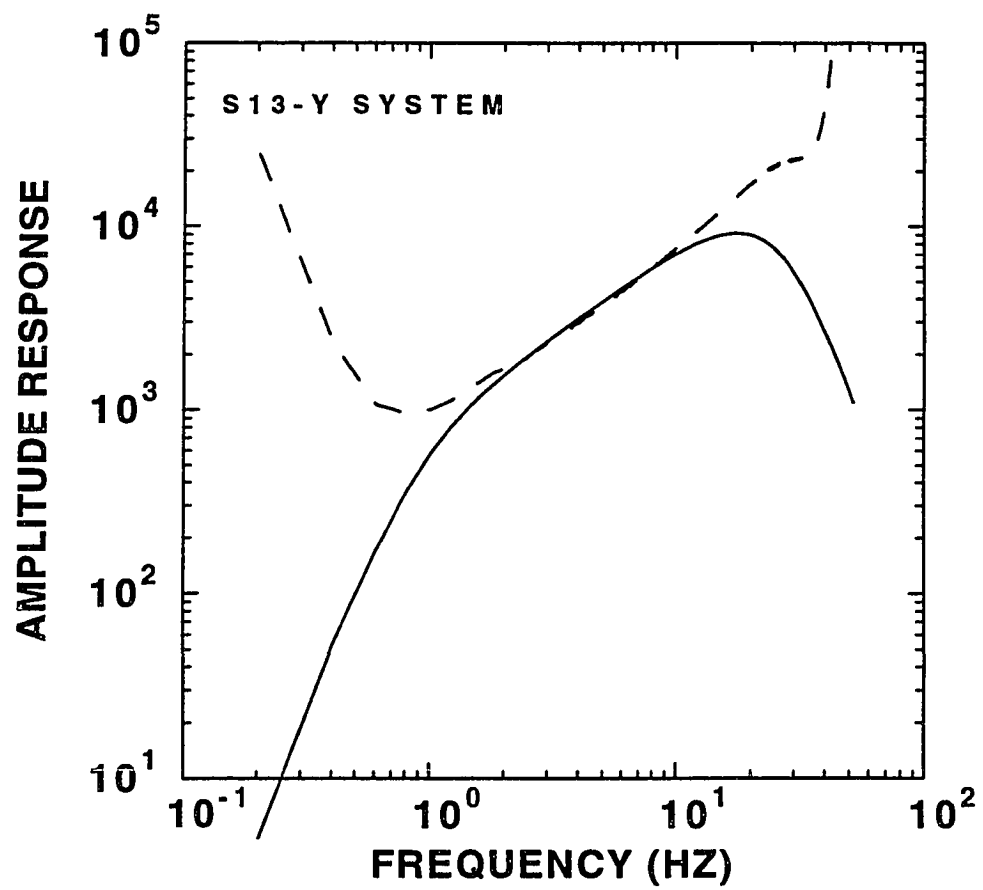


Figure 2.6. Same as Figure 2.3 but for the S13-Y system.

by the deconvolution for frequencies less than 1 Hz and frequencies greater than 25 Hz is the result of low-pass and high-pass filtering inherent in the inverse filter.

Low-pass filtering in the inverse filter is necessary because the instrument removal strongly amplifies any high-frequency noise present in the record. High-pass filtering is necessary because low-frequency noise present in the record is strongly amplified by the computation of response spectral values at long periods. Avoiding the use of high-pass filters with too sharp a cutoff, which may cause oscillation at frequencies near the cutoff frequencies, is generally preferred (Joyner and Boore, 1988). In this study a zero phase band-pass Butterworth filter of sixth order with high-pass frequency of 0.2 Hz and low-pass frequency of 35 Hz was applied. It was also necessary to pad the record with enough zeros to accommodate the transient at the end of the record.

In another numerical experiment, an impulse function was input into the system transfer function, and from there into the zero-phasing inverse filters. If the procedure is mathematically correct the resulting output has to be another impulse function. The amplitude and phase spectrum of the Fourier transformed time series are shown in Figures 2.7 - 2.10. These overall amplitudes are very close to unity and the phase to 0° in the 1.5 to 25 Hz pass band. This demonstrates that the inverse filters behave as desired

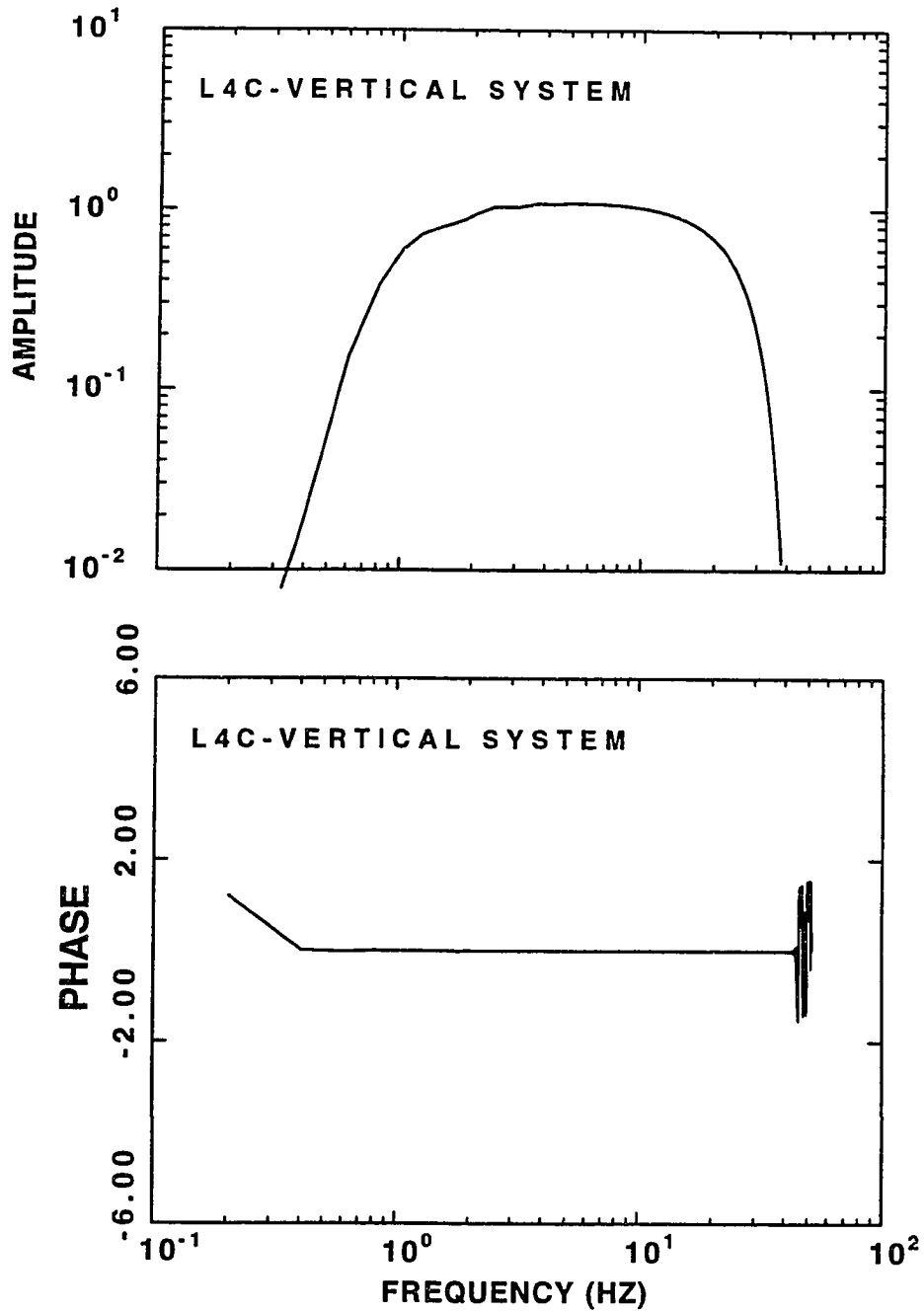


Figure 2.7. Test of reconstitution of input for L4C-V system. An impulse time function is input in the recursive instrument response function and the inverse recursive deconvolution filter is applied on the output. The output is a zero phase, unit spectrum, which is approximately realized in the passband.

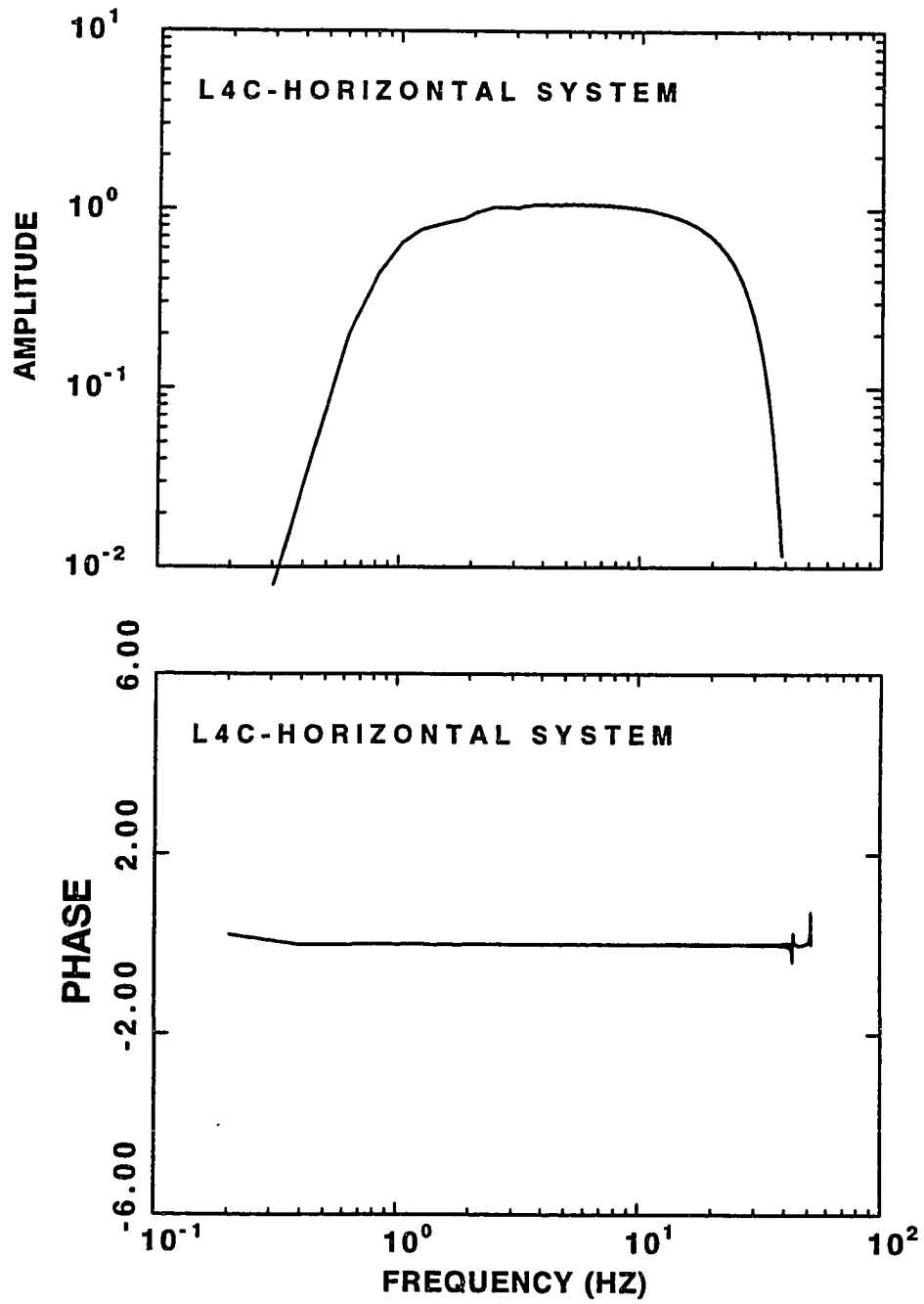


Figure 2.8. Same as Figure 2.7 but for L4C-H system.

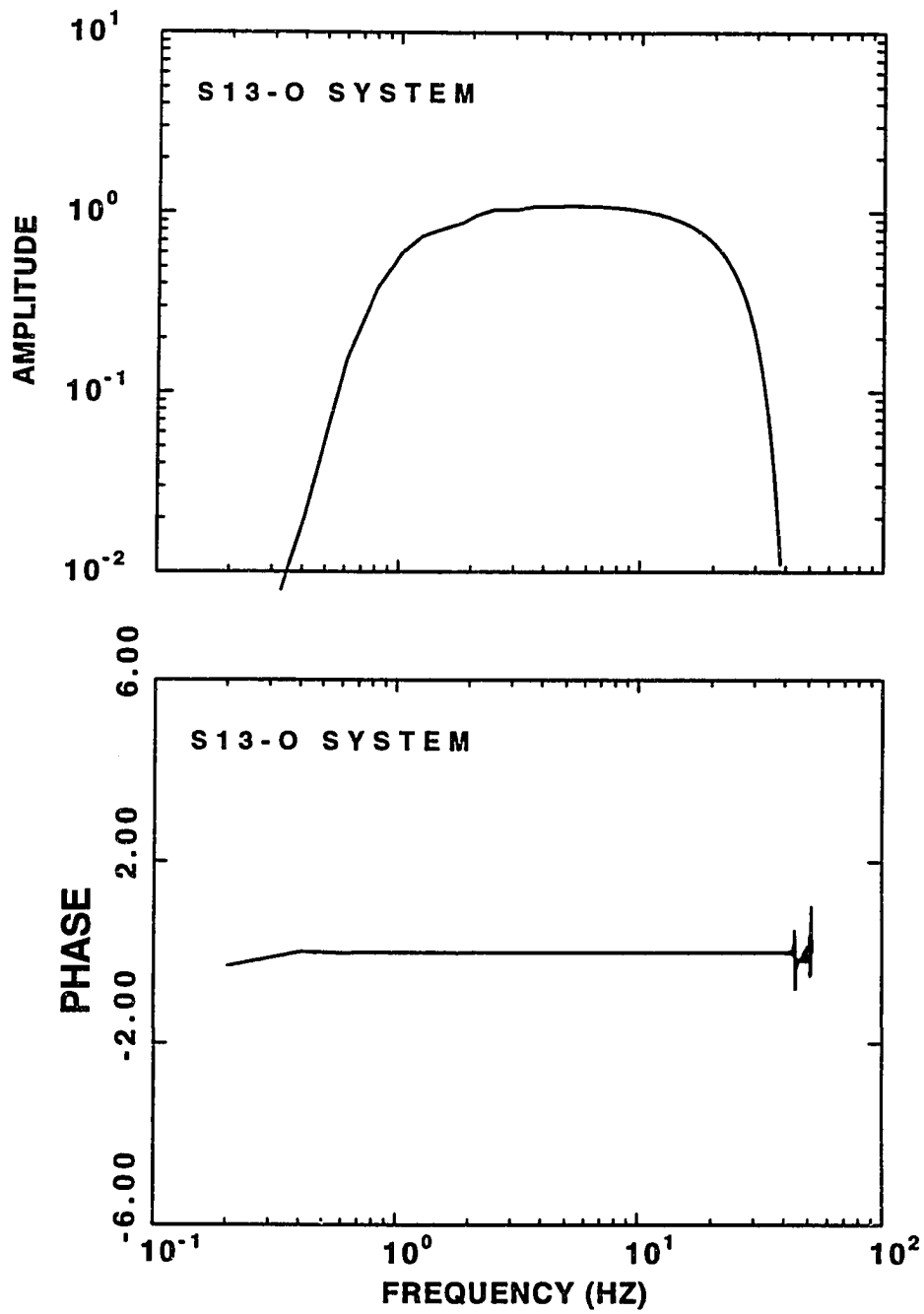


Figure 2.9. Same as Figure 2.7 but for S13-O system.

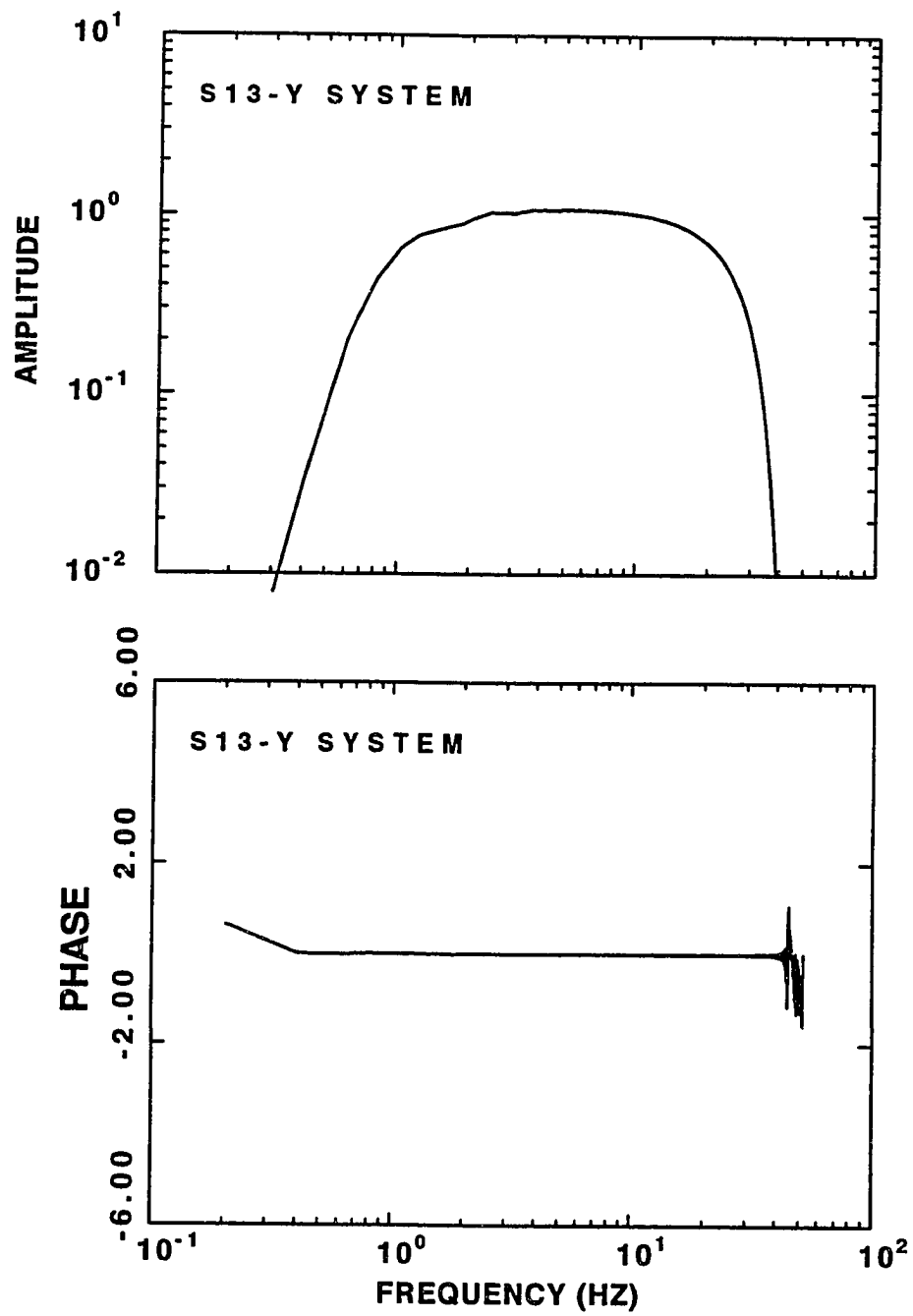


Figure 2.10. Same as Figure 2.7 but for S13-Y system.

in their pass band.

In a third experiment, a time function is input into the transfer function of the instrument systems and the inverse procedure is applied on the output. Results shown on Figures 2.11 - 2.14 show the input time function and the time function after the instrument was imposed and removed. The only significant difference between these two signals is the non-causal behavior of the output signal due to the zero-phasing design of the inverse.

Figure 2.15 shows an original seismogram of earthquake number 5 in Table 1.1 recorded at BGB along with the deconvolved records of ground displacement, velocity, and acceleration. Since the instrument response is essentially a velocity transducer in this frequency range, the deconvolved ground velocity is very similar to the original seismogram. In our procedure, we calculated the deconvolved ground displacements after removing the instrument. Subsequent time derivatives are used to find the acceleration records for calculating response spectra in applications that will be needed later in Chapter 3.

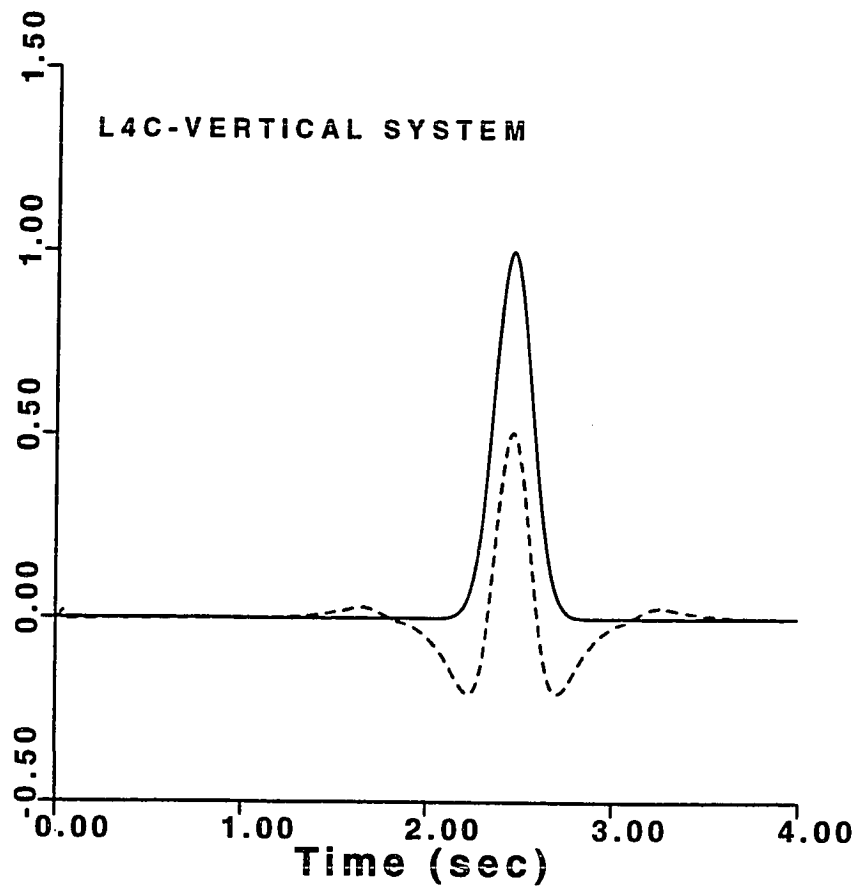


Figure 2.11. An impulse time function, shown by the solid line, is input into the recursive instrument system of L4C-V and the inverse recursive deconvolution filter for L4C-V is applied on the output. The resulting output is shown by the dashed line. Notice the non-causal nature of the procedure causes the early and late arrival of the pulse.

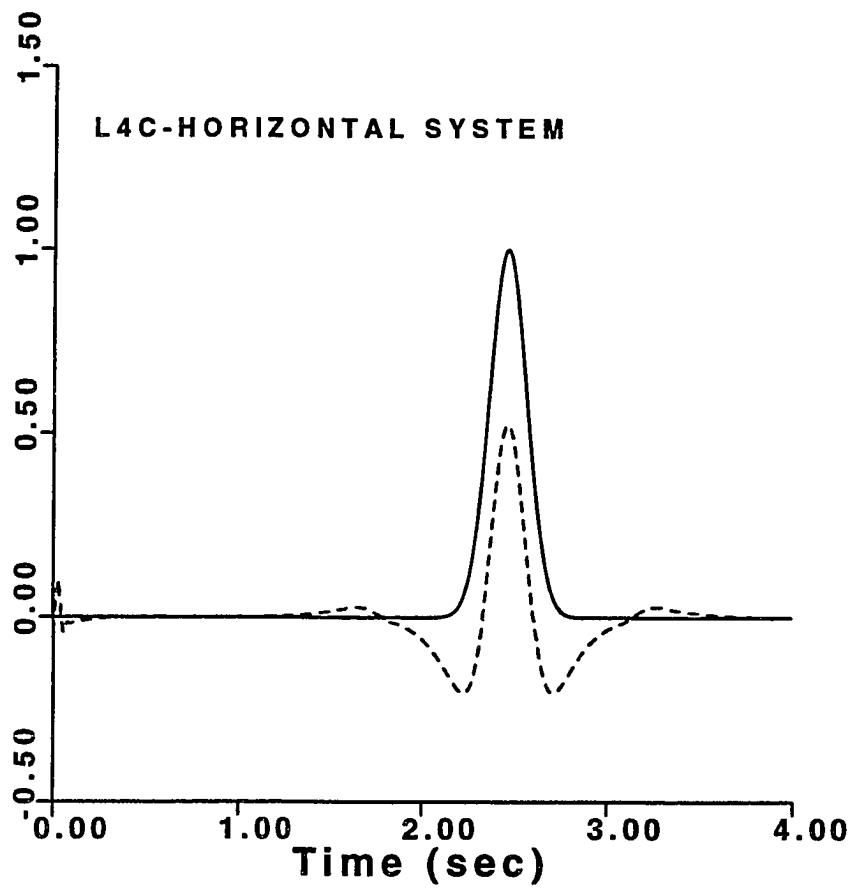


Figure 2.12. Same as Figure 2.11 but for the L4C-H system.

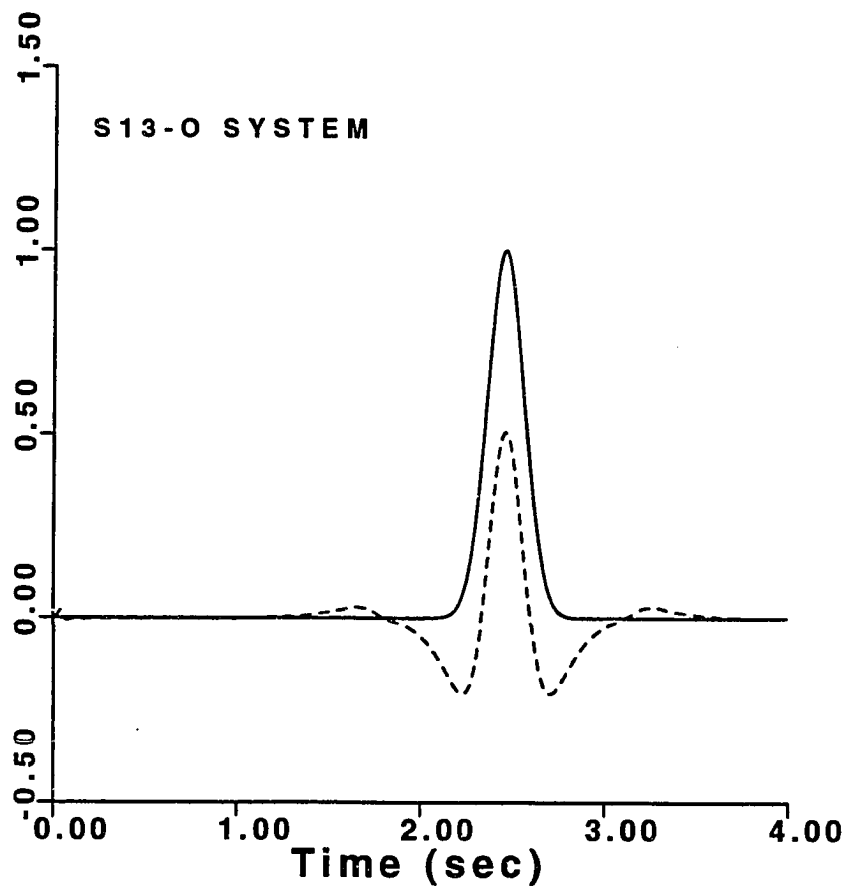


Figure 2.13. Same as Figure 2.11 but for the S13-O system.

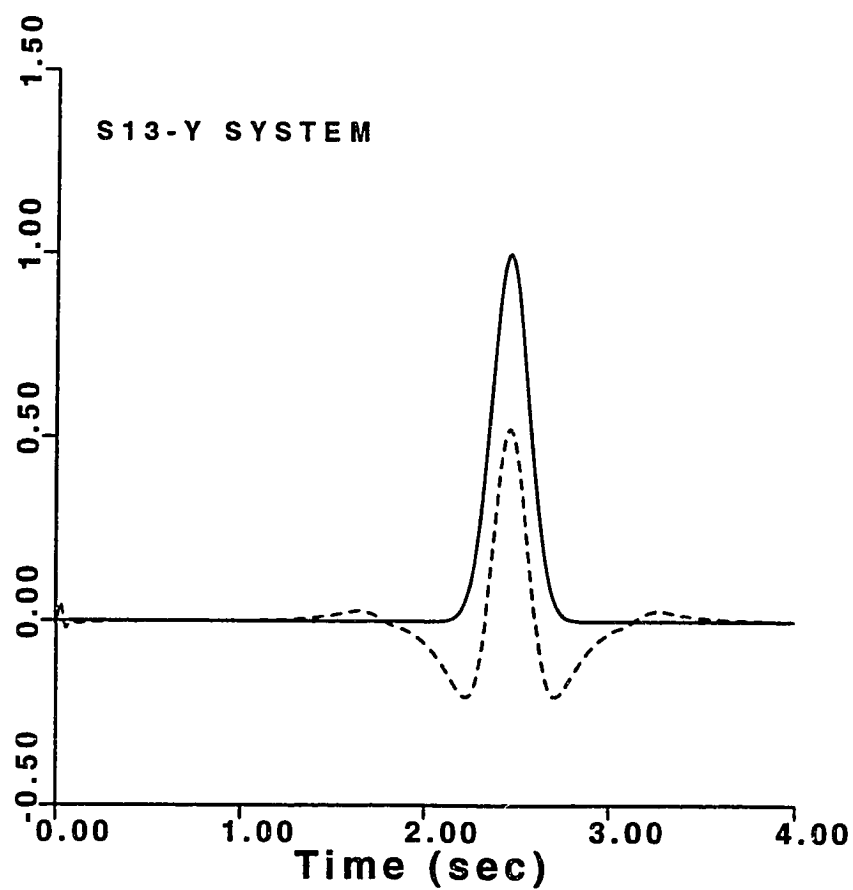


Figure 2.14. Same as Figure 2.11 but for the S13-Y system.

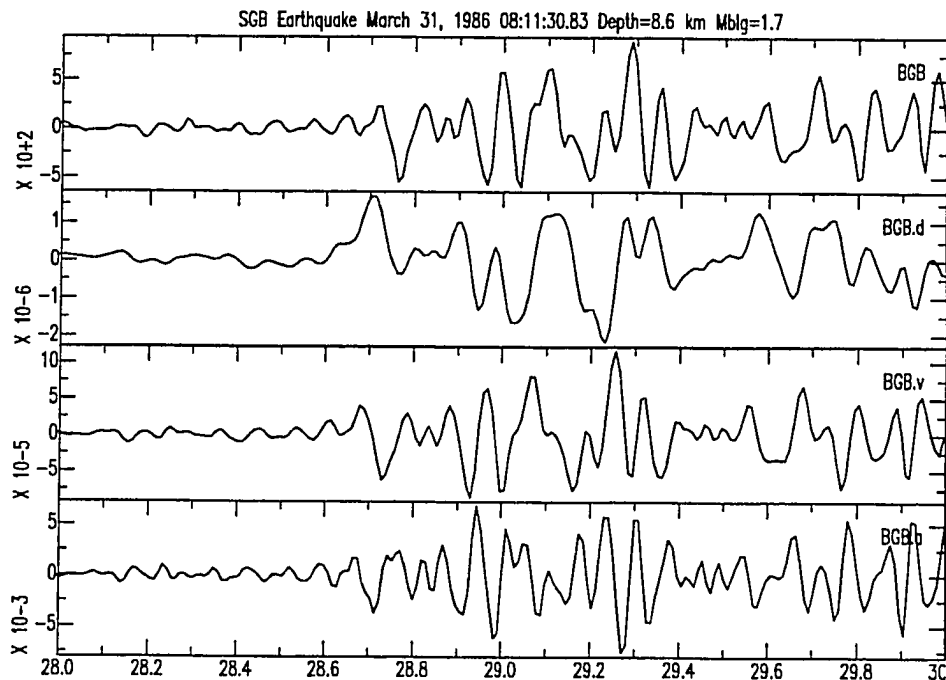


Figure 2.15. A typical seismogram shown here before removal of instrument and the restituted displacement, velocity, and acceleration after applying the inverse recursive deconvolution procedure. On the top, the seismogram recorded at BGB shown as units of counts versus time in seconds from the beginning of recording. The other time series shown are displacement, cm; velocity, cm/s; and acceleration, cm/s/s, respectively. Notice that the seismogram and the acceleration, cm/s/s, respectively. Notice that the seismogram and the velocity time series are very similar which is expected because the instrument is a velocity sensor in the passband.

CHAPTER 3

ATTENUATION OF RESPONSE SPECTRA

3.1 Introduction

Attenuation studies of seismic waves have been carried out on different parts of the seismogram, in various frequency bands, and at different source-receiver distance ranges. A particular attenuation study of interest is the attenuation of the peak amplitudes of seismic waves at distances between a few kilometers to a few hundred kilometers separation of source and receiver. This type of study is of particular interest to earthquake engineering as well as to the physics of elastic wave propagation in an attenuating medium. A direct observation of peak amplitude decay with distance, commonly referred to as apparent attenuation, can be a confusing task depending on kind of measurement used to determine the peak amplitude.

Observational studies by Nuttli (1973), Dwyer *et al.* (1983) and numerical studies by Campillo *et al.* (1984) and Herrmann and Kijko (1983) suggest that peak short-period vertical ground motions at regional distances are produced by the Lg wave with peak amplitudes behaving according to

$$A = A_0 r^{-5/6} e^{-\gamma r}$$

where r is the epicentral distance (in kilometers), γ is the attenuation coefficient (km^{-1}), and A_0 is the source term. This formulation is appropriate at distances great enough such that the peak ground motion consists of S waves trapped in the crustal waveguide (Rogers *et al.*, 1987).

Another accepted procedure for studying attenuation is to obtain the response spectra for each recording of ground motion. Response spectra at different damping parameters can be obtained for selected frequencies. King and Hays (1977) used a pseudo-relative velocity response for frequencies 5 to 20 Hz to obtain attenuation in Utah, Nevada and California. Gupta and McLaughlin (1987) used a more spatially distributed response spectra data set in the eastern United States to obtain a frequency dependent attenuation relation. A multiple regression method is needed to separate source-site effects as well as geometrical spreading from the observed ground motion to be able to estimate attenuation at different frequencies. In addition, it is important to test the hypothesis that Lg is the predominant ground motion on short-period records in the western United States. This assumption has been accepted in the more stable, older continental crust of the eastern United States (Nuttli, 1973).

3.2 Parametrization of the attenuation problem

A convenient empirical model to represent spatial attenuation of Lg waves in the time domain is

$$A = Z S e^{-\gamma r} r^{-c_1} r^{-c_2} \quad (3.1)$$

where A represents maximum (or sustained) ground displacement, S is a source term, Z is receiver term, γ is the anelastic attenuation coefficient, r is hypocentral distance, c_1 represents geometrical spreading and c_2 , the dispersion term. For time domain surface-wave measurements of the Airy phase, $c_2 = 0.33$ and for the non-airy (dispersive) phase, $c_2 = 0.5$ (Ewing *et al.*, 1957; Nuttli, 1973) while $c_1 = 0.5$. The quality factor, Q, is defined as $Q = \frac{\pi f}{\gamma u}$, where u is the group velocity of Lg.

For a calculation of the anelastic attenuation coefficient of attenuation in the frequency domain, the Fourier amplitude spectrum at a given frequency will replace A in Equation 2.1. If the time window is chosen to include the entire dispersed waveform, then c_2 can be omitted (Hasegawa, 1985). Thus the empirical model for frequency-domain observations can be stated as

$$F(f) = Z(f) S(f) e^{-\gamma r} r^{-c_1}. \quad (3.2)$$

For a large earthquake-receiver data set that has good azimuthal coverage, the above empirical model for both time-domain and

frequency domain is justifiable. Taking the logarithms of (3.1) and (3.2), both equations can be written in the form

$$a_{ij} = z_i + s_j - \gamma r_{ij} \log_{10} e - c \log_{10} r_{ij} \quad (3.3)$$

where

$$a_{ij} = \log_{10} A_{ij}, \quad s_j = \log_{10} S_j, \quad z_i = \log_{10} Z_i .$$

A_{ij} is the amplitude of the j 'th earthquake observed at i 'th station, s_j is the source term of the j 'th event, z_i is the site term for the i 'th station, and r_{ij} is the hypocentral distance from j 'th event to the i 'th station. We now express (3.3) in a matrix form

$$\mathbf{d} = \mathbf{M} \mathbf{x} \quad (3.4)$$

where

$$\mathbf{d} = \begin{bmatrix} a_{11} \\ a_{12} \\ \vdots \\ a_{1n} \\ a_{21} \\ a_{22} \\ \vdots \\ a_{2n} \\ \vdots \\ \vdots \\ a_{mn} \end{bmatrix} .$$

n is the number stations and m is the number of earthquakes used, therefore D is a vector of $(m \times n)$ rows and one column.

$$\begin{array}{c}
 \longleftarrow m + n + 2 \longrightarrow \\
 \begin{array}{cc}
 n \text{ stations} & m \text{ events} \\
 \hline
 \end{array} \\
 \mathbf{M} = \begin{bmatrix}
 -r_{11} & -\log r_{11} & 1 & 0 & 0 & \dots & 0 & 1 & 0 & 0 & \dots & 0 \\
 -r_{21} & -\log r_{21} & 0 & 1 & 0 & \dots & 0 & 1 & 0 & 0 & \dots & 0 \\
 \cdot & & & & & & & & & & & \\
 \cdot & & & & & & & & & & & \\
 \cdot & & & & & & & & & & & \\
 \cdot & & & & & & & & & & & \\
 -r_{n1} & -\log r_{n1} & 0 & 0 & 0 & \dots & 0 & 1 & 1 & 0 & 0 & \dots & 0 \\
 -r_{12} & -\log r_{12} & 1 & 0 & 0 & \dots & 0 & 0 & 1 & 0 & 0 & \dots & 0 \\
 \cdot & & & & & & & & & & & & \\
 \cdot & & & & & & & & & & & & \\
 \cdot & & & & & & & & & & & & \\
 \cdot & & & & & & & & & & & & \\
 -r_{nm} & -\log r_{nm} & 0 & 0 & 0 & \dots & 0 & 1 & 0 & 0 & \dots & 0 & 1
 \end{bmatrix}
 \begin{array}{c}
 \uparrow \\
 | \\
 | \\
 | \\
 | \\
 | \\
 | \\
 | \\
 | \\
 | \\
 | \\
 \downarrow
 \end{array}
 \begin{array}{c}
 m \\
 x \\
 n
 \end{array}
 \end{array}$$

This is a matrix of $m \times n$ rows and $m+n+2$ columns where m are total number of events and n number of stations.

$$\mathbf{x} = \begin{bmatrix}
 \gamma \log_{10} e \\
 c \\
 z_1 \\
 \cdot \\
 \cdot \\
 \cdot \\
 z_n \\
 s_1 \\
 \cdot \\
 \cdot \\
 s_m
 \end{bmatrix}$$

where z_i , $i = 1, n$ are site terms, s_i , $i = 1, m$ represent source terms and the first two elements describe the attenuation and geometrical spreading, respectively.

Site terms represent amplification (deamplification) of amplitude for a given frequency at a particular site. Since all the stations used here are on nominal hard rock, we impose a constraint that the logarithmic sum of all site effects in (3.3) equals zero:

$$\sum_{i=1}^n z_i = 0 . \quad (3.5)$$

This condition eliminates the inherent linear dependence in which an arbitrary function of frequency can be added to the site term and subtracted from the source term for a system without constraint (Castro et al., 1990).

In our inversion scheme, this constraint can be imposed by adding one row corresponding to (3.5) to the matrix M and weighting this row much greater than the other rows (Lawson and Hanson, 1974). Equation (3.4) can be used to solve for the attenuation term, the geometrical spreading coefficient, the site amplification term, and the source term, under the usual least-squares criterion. In a full inversion case, it is expected that one or more of the eigenvalues will be zero. To avoid these singularities we have used a singular value decomposition and generalized inverse techniques. For the large scale inversion for this work, it is probable that one or

more of the eigenvalues are small enough to dominate the solution. To remedy this, we adopt the stochastic inversion method briefly discussed here. We apply this inversion technique to our ground motion problems as well as to the coda method which will be discussed later.

3.3 Singular value decomposition and the stochastic inverse

To solve the matrix equation

$$\mathbf{d} = \mathbf{M}\mathbf{x} + \boldsymbol{\epsilon} \quad (3.6)$$

for vector \mathbf{x} and data residual $\boldsymbol{\epsilon}$, in the least-square sense, we will minimize

$$(\mathbf{d} - \mathbf{M}\mathbf{x})^T (\mathbf{d} - \mathbf{M}\mathbf{x}) + \mathbf{x}^T \mathbf{x} \quad (3.7)$$

where T denotes transpose and conjugate. The standard singular value decomposition method calls for the decomposition of \mathbf{M} , into $\mathbf{U} \boldsymbol{\Lambda} \mathbf{V}^T$, where \mathbf{U} and \mathbf{V} are orthogonal matrices, i.e. $\mathbf{U}^T \mathbf{U} = \mathbf{I}$ and $\mathbf{V}^T \mathbf{V} = \mathbf{I}$ (Russell, 1988). Here \mathbf{U} and \mathbf{V} are partitioned into two matrices each, $\mathbf{V} = (\mathbf{V}_m, \mathbf{V}_o)$ and $\mathbf{U} = (\mathbf{U}_m, \mathbf{U}_o)$ where \mathbf{U}_m and \mathbf{V}_m are made up from eigenvectors with nonzero eigenvalues:

$$\mathbf{M} \mathbf{V}_m = \mathbf{U}_m \boldsymbol{\Lambda}_m \quad (3.8)$$

$$\mathbf{M}^T \mathbf{U}_m = \mathbf{V}_m \boldsymbol{\Lambda}_m \quad (3.9)$$

\mathbf{U}_o and \mathbf{V}_o are composed of eigenvectors with zero eigenvalues:

$$M V_o = 0$$

$$M^T U_o = 0 \quad (3.10)$$

and Λ is a diagonal matrix of eigenvalues partitioned into $(\Lambda_m, 0)$.

V and U are coupled through equations (3.9). Therefore

$$M = U\Lambda V^T = U_m \Lambda_m V_m^T \quad (3.11)$$

The stochastic inverse of M is L

$$L = M^T(MM^T + e^2I)^{-1} \quad (3.12)$$

and therefore, the solution to the problem is Ld or

$$x = M^T(MM^T + e^2I)^{-1} d = V \frac{\Lambda}{\Lambda^2 + e^2I} U^T d \quad (3.13)$$

Aki and Richards (1980) assumed both d and x are stochastic processes and solved this problem by minimizing the statistical average between x and Ld . They showed in a special case where the covariance of the model solution x , $\text{cov } x$, and covariance of residual data, $\text{cov } \epsilon$, are given by

$$\begin{aligned} \text{cov } x &= \sigma_x^2 I, \\ \text{cov } \epsilon &= \sigma_\epsilon^2 I, \end{aligned} \quad (3.14)$$

$$e^2 = \frac{\sigma_\epsilon^2}{\sigma_x^2}, \quad (3.15)$$

(3.13) gives a good approximation to the general inverse solution.

Here σ_x^2 and σ_ϵ^2 are variances of solution x and the residual data ϵ respectively. Levenberg (1944) also obtained (3.14) by minimizing

$$\frac{|d - Mx|^2}{\sigma_\epsilon^2} + \frac{|x|^2}{\sigma_x^2}, \quad \text{where again } e^2 = \sigma_\epsilon^2/\sigma_x^2. \quad (3.13) \text{ is an}$$

approximation to the generalized inverse in such a way that the contribution of eigenvectors with eigenvalues smaller than ϵ^2 is suppressed in the stochastic inverse.

3.4 Attenuation measurements

In this study, we employ PSRV and SV, each representing some measurement of ground motion. We remove the instrument response recursively according to the procedure explained in Chapter 2, and compute the displacement records. After taking two derivatives of the displacement, the resulting acceleration is used to compute the response spectra. The procedure to calculate the response spectra including *relative velocity response, SV; pseudo relative velocity response, PSRV* and other response spectra is discussed in Appendix A. Figure 3.1 shows the PSRV and SV for two of the records used in this study at 2 and 10 Hz. In Figure 3.2, we show the attenuation curve, as measured by SV, of event number 39 in Table 1.1 recorded in 28 stations from 22 km to 160 km hypocentral distance at 2 and 10 Hz. We use a low damping of two percent for the data presented here.

In the distance range of our interest, from a few kilometers to less than two hundred kilometers from the source, the envelope of the group of the phases which represents the peak motion can change because the physics of wave propagation will be different.

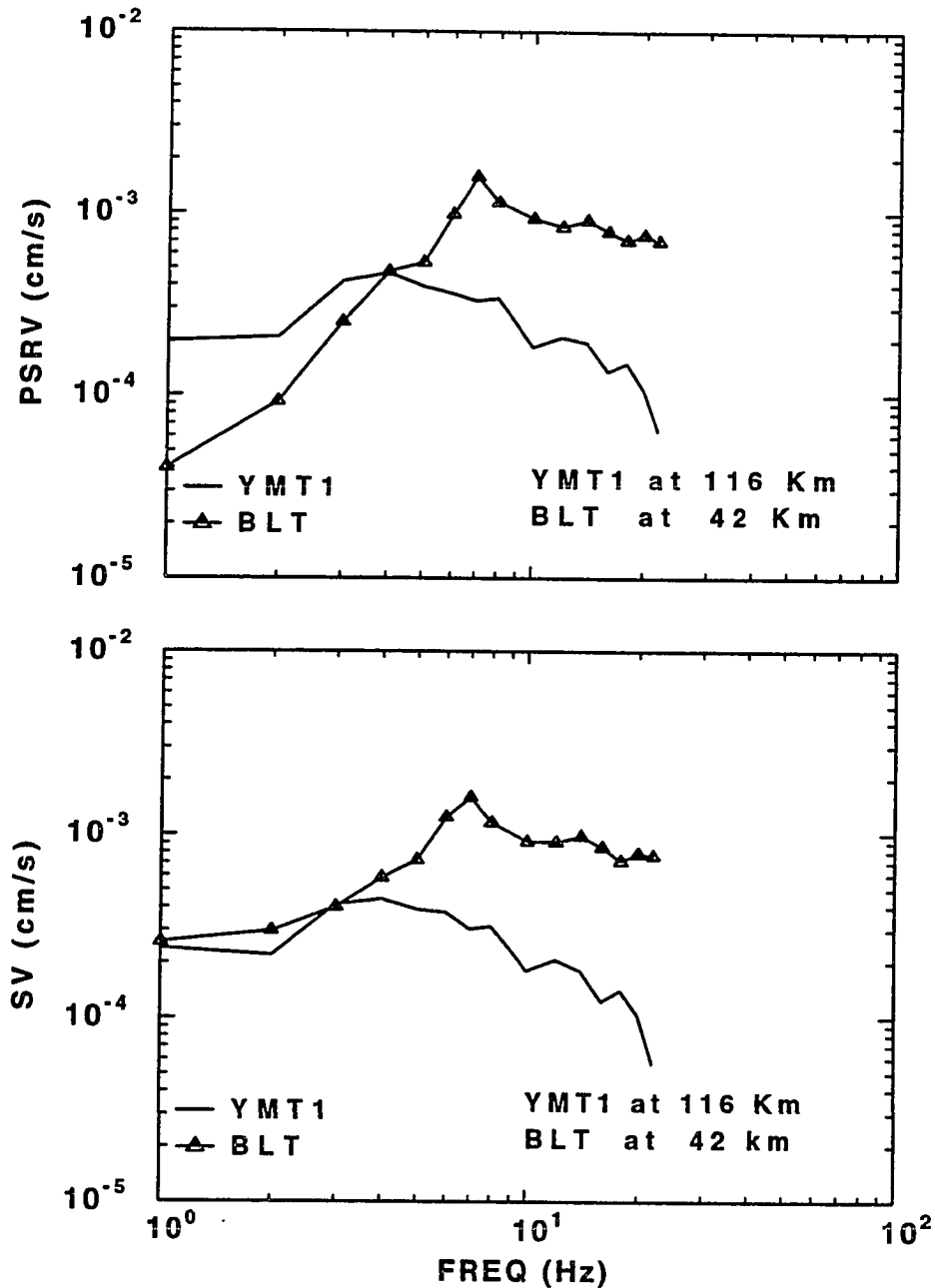


Figure 3.1. PSRV and SV calculated for the earthquake on May 27, 1986 15:42:46.38. The location is given in Table 2.1. Notice the similarity between these two spectra for frequencies higher than 5 Hz. For frequencies close to 1.0 Hz there is a difference between these two measurements as is explained in Appendix A.

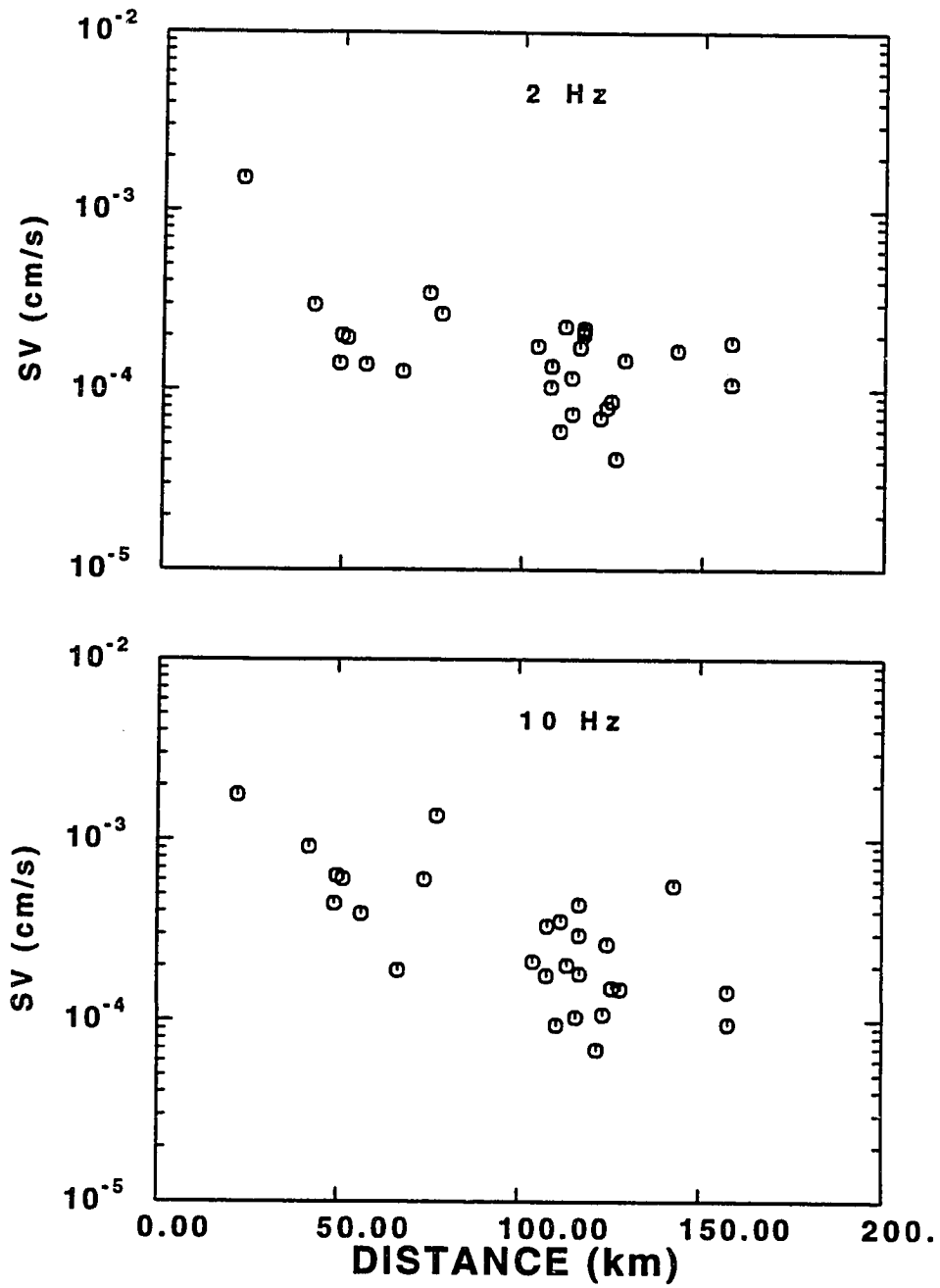


Figure 3.2. SV plots versus distance for earthquake 39 of Table 1.1 for frequencies of 2 and 10 Hz.

For distances less than two thicknesses of the crust, direct rays or phases, that do not suffer severe interference from major discontinuities, dominate. It is generally assumed that the amplitude of these phases decays geometrically as $\frac{1}{r}$. At around 150 km and longer distances, supercritically reflected phases from the Moho and trapped waves gradually dominate the observed wave motion. These are all from the family of surface waves. These phases decay geometrically as $\frac{1}{r^{1/2}}$ and also disperse as $\frac{1}{r^{1/3}}$. The nature of ground motion in the transition zone between these two regimes is very complex.

There is a great degree of subjectivity as to what geometrical spreading coefficient is appropriate for a data set that spans these distance ranges. It can be argued that the selection of a geometrical spreading coefficient factor, therefore, is more a matter of definition and usefulness than exact physical meaning. For time domain studies, many seismologists tend to choose $\frac{1}{r^{1/2}}$ $\frac{1}{r^{1/3}}$ for the distance range greater than 100 km and $\frac{1}{r}$ for less than 100 km (Nuttli, 1973; Hasegawa, 1985; Joyner and Boore, 1988). The earthquake engineer, on the other hand, prefers to use a simple $\frac{1}{r}$ decay for all distances for both time domain and frequency domain studies since this simplifies other analysis. This choice, however removes any physical

meaning from the γ coefficients. In this study, we will examine the range of geometrical spreading factor from $\frac{1}{r^{1/2}}$ to $\frac{1}{r}$.

Attenuation of Response Spectra

A set of plots similar to Figure 3.2 for all the events constitutes the data base for attenuation studies. Regression analysis of the response spectra data based on the method described for the solution of the matrix equation (3.4) were performed for the geometrical spreading exponent c in the range 0.5 to 1. for both SV and PSRV data sets. Q values calculated for $1/r$ and $1/r^{0.833}$ are very large for frequencies less than 6 Hz. For geometrical spreading of $1/r$, the calculated Q from our regression analysis is negative for frequencies of 2 and 3 Hz. In order to obtain Q values physically acceptable with mathematically reasonable standard deviation in the lower frequency range, c has to be about 0.5 or smaller for the entire distance range.

To allow a distance related geometrical spreading attenuation analysis, a modified wave propagation formula to replace (3.3) is needed. A trilinear geometrical spreading model similar to that from the study by Atkinson and Mereu (1992) with two critical distances d_0 and d_1 was applied. The regression equations that guarantee continuity of the attenuation curves and their derivatives at the two critical distances are

$$\begin{aligned}
 a_{ij} &= s_i + z_j - \gamma r_{ij} \log_{10} e - c_1 \log_{10} r_{ij} \\
 &\quad \text{for } r_{ij} \leq d_o \\
 a_{ij} &= s_i + z_j - \gamma r_{ij} \log_{10} e - c_1 \log_{10} d_o - c_2 \log_{10} \frac{r_{ij}}{d_o} \\
 &\quad \text{for } d_o \leq r_{ij} < d_1
 \end{aligned}$$

and

$$\begin{aligned}
 a_{ij} &= s_i + z_j - \gamma r_{ij} \log_{10} e - c_1 \log_{10} d_o - c_2 \log_{10} \frac{d_1}{d_o} \\
 &\quad - c_3 \log_{10} \frac{r_{ij}}{d_1} \quad \text{for } r_{ij} \geq d_1.
 \end{aligned} \tag{3.16}$$

Figure 3.3 shows the SV at 2 Hz corrected for source and site terms plotted versus hypocentral distance. We performed several regressions to obtain physically and mathematically acceptable values for γ and geometrical spreading factors in the three distance ranges to minimize the average residual error. The lowest residuals of the regression are obtained if we choose $d_o = 60$ km and $d_1 = 125$ km. The values of Q are generally very close for SV data and PSRV data. We start regression of the data by imposing the constraint that the shear waves travel like body waves with geometrical spreading of $\frac{1}{r}$ for distances less than 60 km which is twice of the average thickness of the crust in the Basin and Range (Eaton, 1982). A similar regression analysis on a data set in eastern Canada using Fourier amplitudes favored slightly higher geometrical attenuation for the shorter distance range (Atkinson and Mereu, 1992). The

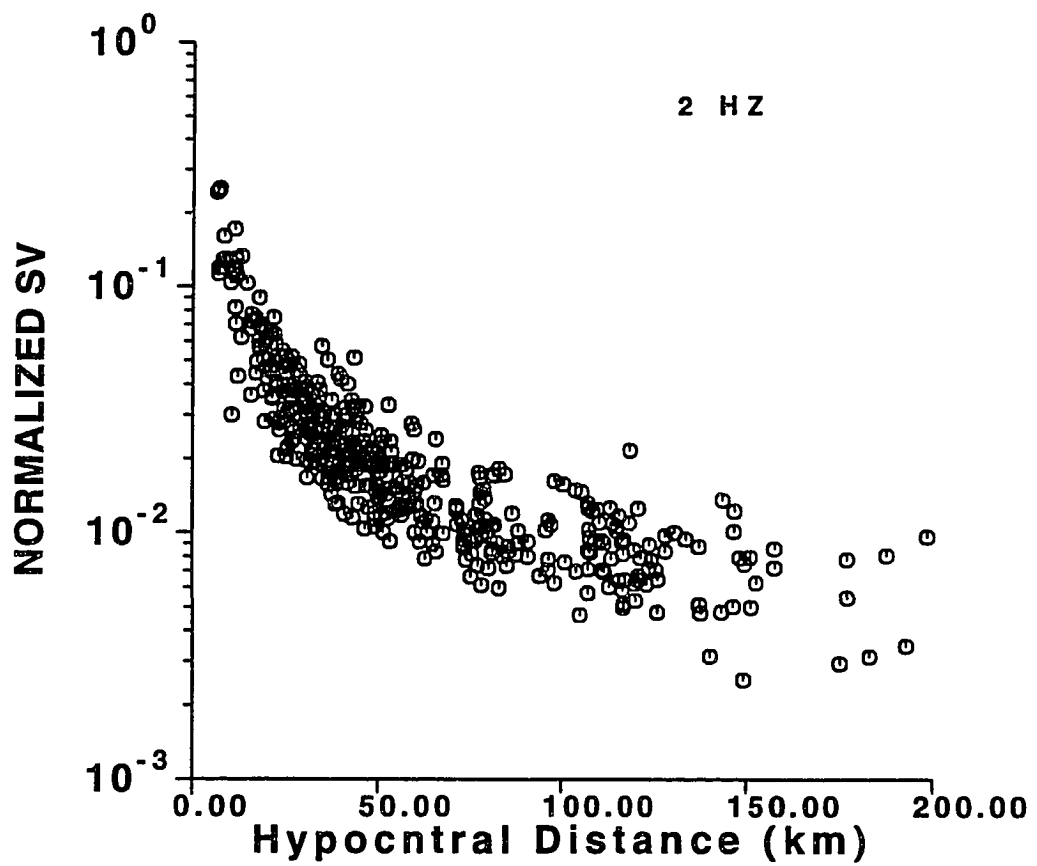


Figure 3.3. Typical attenuation plot using SV amplitudes at 2 Hz. All observations are normalized to the common source, and site terms are removed.

time domain analysis, however tends to converge to a value of geometrical spreading which is more typical of body-wave propagation, i.e. $c_1 = 1.0$. We let the geometrical spreading factor be free parameters to be determined by the regression. Letting $d_0 = 60$ km and $d_1 = 125$ km, values of geometrical spreading parameters c_1 , c_2 , and c_3 and Q and γ are calculated from the trilinear regression of PSRV data tabulated in Table 3.1. Figures 3.4 and 3.5 show the trilinear fit to the PSRV and SV data, respectively. In the midrange distances of 60 to 125 km c_2 is between 0.5 to 0.7 and c_3 corresponding to distances greater than 125 km tend to be slightly higher, $0.9 \geq c_3 \geq 0.7$.

In a second analysis, we force $c_1 = 1.0$ and $c_3 = 0.833$ as fixed parameters of regression and determine c_2 and attenuation from the regression as shown in Table 3.2. We also tried a bilinear regression for which the geometrical spreading parameters are given by c_1 and c_2 corresponding to $r < 60$ km and $r > 60$ km respectively, where again $c_1 = 1.0$ was fixed in the regression. Table 3.3 shows the results of the bilinear regression. Bilinear regression with fixed $c_1 = 1.0$ led c_2 varying between 0.5 to 0.65 .

3.5 Discussion and conclusion

Clearly the choice of the geometrical spreading factor affects the calculated Q and its frequency dependence. Our calculated $Q(f)$

TABLE 3.1

Trilinear regression of PSRV data

Freq (Hz)	γ ($\times 10^{-3}$)	$Q \pm \delta Q$	c_1	$c_2 \pm \delta c_2$	$c_3 \pm \delta c_3$
2	3.99	492 222	1.	0.55 0.19	0.70 0.21
3	3.75	784 336	1.	0.60 0.17	0.76 0.19
4	4.70	836 284	1.	0.53 0.17	0.86 0.19
5	5.87	837 225	1.	0.55 0.17	0.89 0.18
6	7.46	790 160	1.	0.49 0.16	0.91 0.18
7	7.31	939 193	1.	0.62 0.16	0.89 0.18
8	9.05	868 145	1.	0.59 0.16	0.88 0.18
10	11.92	824 103	1.	0.62 0.16	0.89 0.18
12	11.31	1042 130	1.	0.63 0.15	0.89 0.16
14	11.05	1243 163	1.	0.71 0.15	0.86 0.17
16	10.95	1434 192	1.	0.66 0.16	0.81 0.17
18	11.00	1608 225	1.	0.64 0.16	0.75 0.18
20	9.43	2082 335	1.	0.72 0.16	0.73 0.18

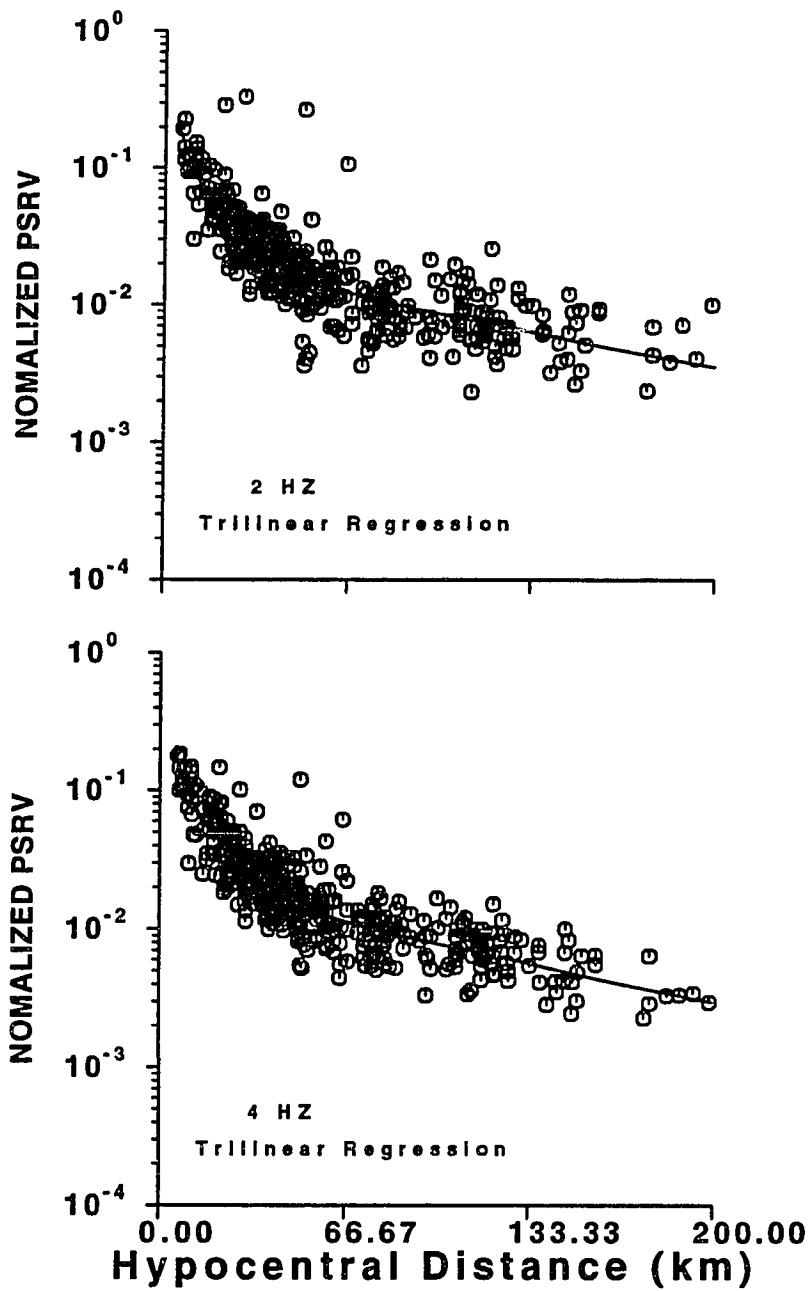


Figure 3.4a. Trilinear regression fit to PSRV data for 2 and 4 Hz.

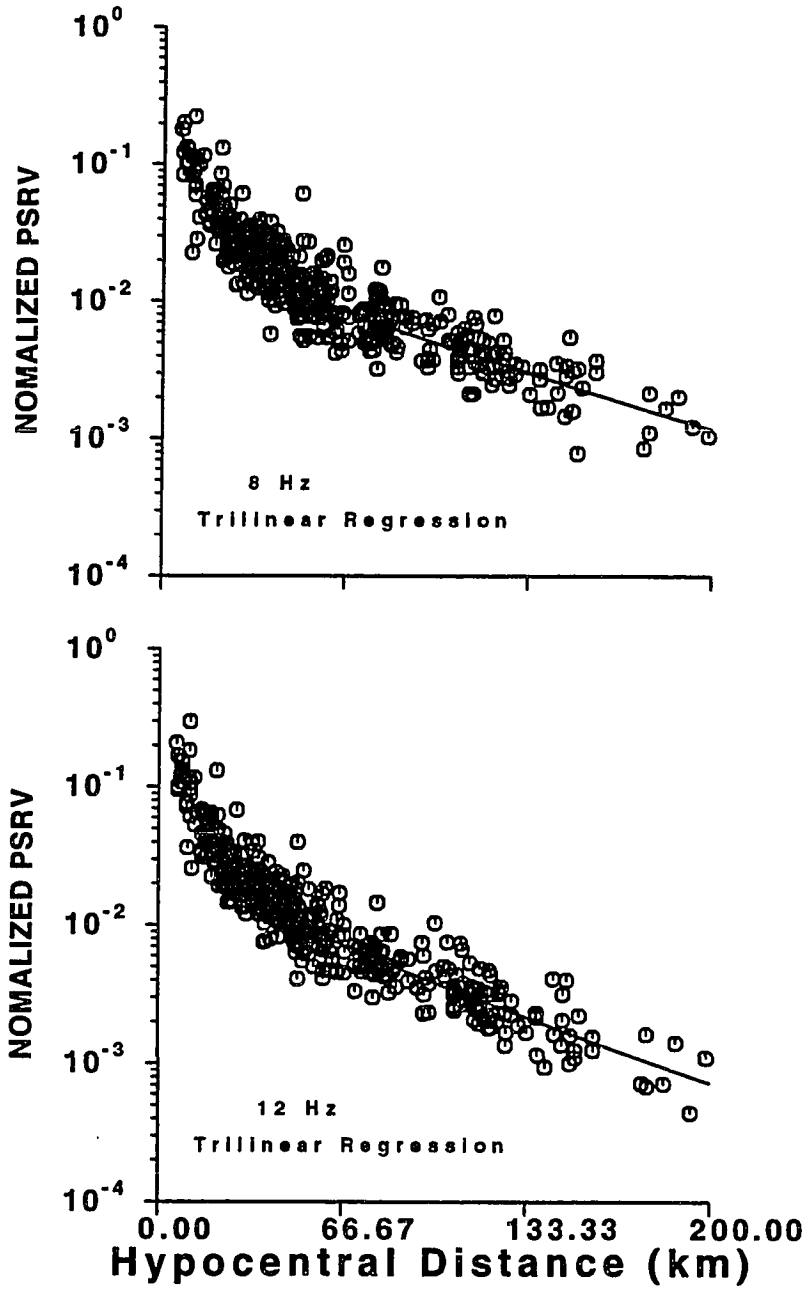


Figure 3.4b. Trilinear regression fit to PSRV data for 8 and 12 Hz.

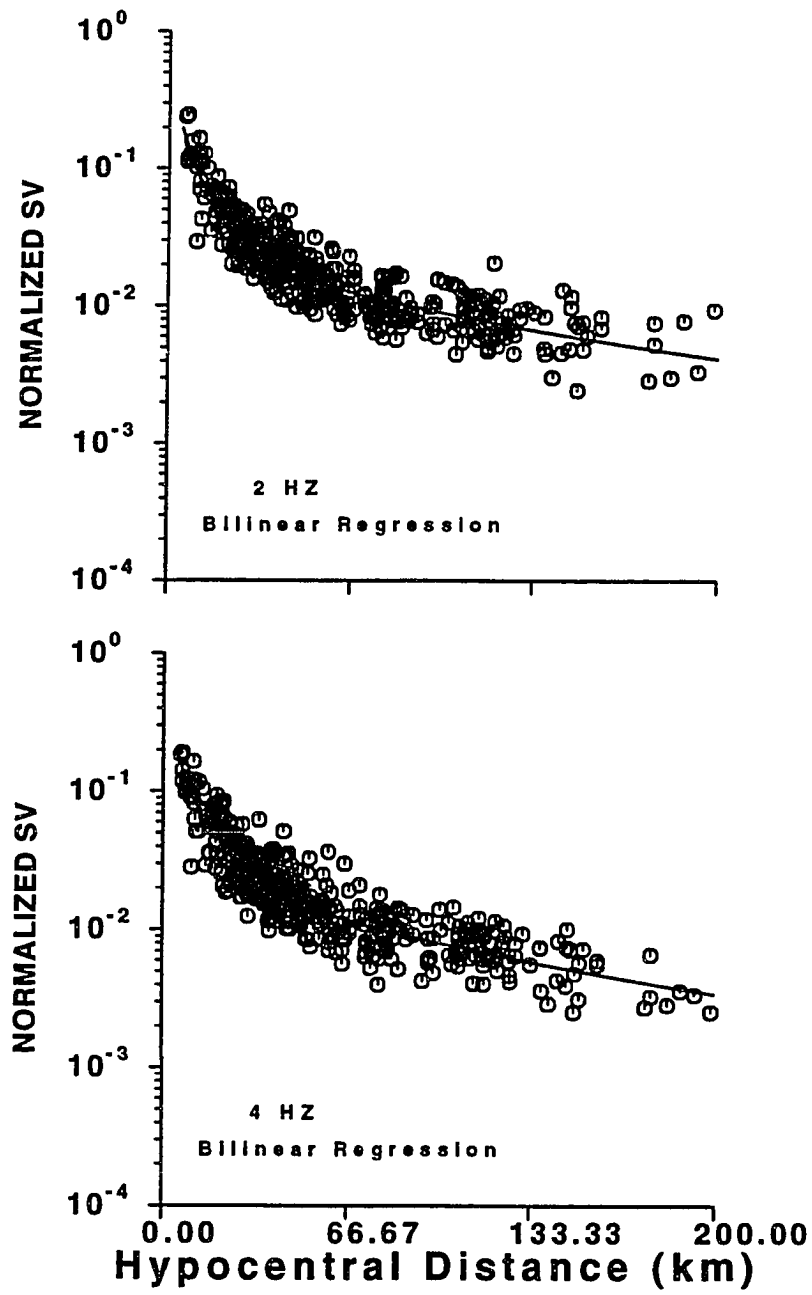


Figure 3.5a Trilinear regression fit to SV data for 2 and 4 Hz.

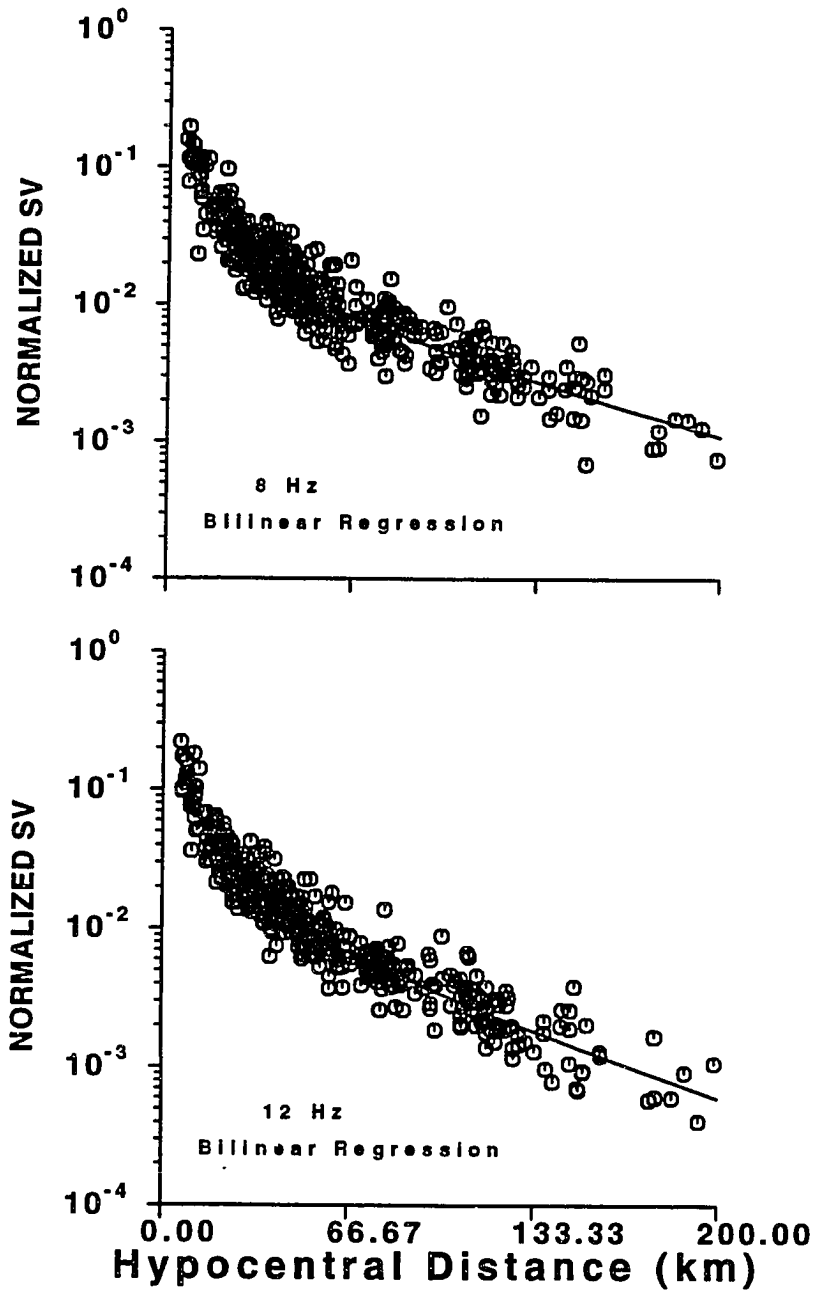


Figure 3.5b Trilinear regression fit to SV data for 8 and 12 Hz.

TABLE 3.2

**Trilinear regression of PSRV data with
fixed geometrical spreading at large distances**

Freq (Hz)	γ ($\times 10^{-3}$)	$Q \pm \delta Q$	c_1	$c_2 \pm \delta c_2$	c_3
2	3.74	524 246	1.	0.55 0.19	0.83
3	3.62	812 352	1.	0.61 0.17	0.83
4	4.75	826 271	1.	0.53 0.17	0.83
5	5.97	821 212	1.	0.55 0.17	0.83
6	7.59	775 151	1.	0.49 0.16	0.83
7	7.41	927 184	1.	0.62 0.16	0.83
8	9.14	859 139	1.	0.59 0.16	0.83
10	12.03	815 99	1.	0.61 0.16	0.83
12	11.41	1032 124	1.	0.63 0.15	0.83
14	11.10	1238 158	1.	0.71 0.15	0.83
16	10.91	1438 189	1.	0.66 0.16	0.83
18	10.85	1629 226	1.	0.65 0.16	0.83
20	9.24	21255 341	1.	0.73 0.16	0.83

TABLE 3.3

Bilinear regression of PSRV data in SGB

Freq (Hz)	γ ($\times 10^{-3}$)	$Q \pm \delta Q$	c_1	$c_2 \pm \delta c_2$
2	3.74	525 200	1.	0.52 0.14
3	3.39	869 364	1.	0.54 0.14
4	4.58	857 285	1.	0.54 0.14
5	5.77	851 221	1.	0.63 0.15
6	7.15	823 150	1.	0.63 0.15
7	7.48	919 189	1.	0.63 0.15
8	9.74	807 128	1.	0.65 0.15
10	11.93	823 103	1.	0.65 0.15
12	12.41	949 109	1.	0.68 0.14
14	11.09	1239 167	1.	0.75 0.15
16	11.53	1362 177	1.	0.66 0.15
18	12.03	1469 193	1.	0.58 0.16
20	10.47	1876 278	1.	0.62 0.15

for both bilinear and trilinear regression of PSRV data are close and support a model in which Q is relatively frequency independent for frequencies less than 8 Hz, $Q \approx 600 f^{0.15}$. For frequencies greater than 8 Hz Q can be approximated by $Q = 150 f^{0.8}$. Rogers *et al.* (1987) calculated large values of Q at lower frequencies from band passed data. Their conclusion was geometrical spreading of $c = 0.833$, and a $Q = 700f^{0.05}$. In their analysis any S-wave energy propagates similar to Lg wave. Our results supports their conclusions if we simply assume that waves propagate with the same geometrical spreading throughout the distance range of this study. However, our results support a segmented geometrical spreading which implies that the nature of propagating elastic wave changes at around twice the thickness of the crust. Bilinear and a trilinear regression produce for greater distances results which are in agreement within the error estimate of the technique. A geometrical spreading of 0.5 to 0.7 for wave propagation beyond 60 km hypocentral distance can explain the slow decay of amplitude beyond 60 km. Our analysis emphasizes the important role of proper application of geometrical spreading in ground motion studies when network data are used. Many synthetic studies have predicted a complex behavior of geometrical spreading at distance range of roughly twice the thickness of the crust (Ou and Herrmann, 1990; Frankel *et al.* 1990). These findings are in agreement with Burger *et al.* (1987), that postcritical reflections from the Moho discontinuity play

a major role in determining the values of attenuation.

More recently, Atkinson and Mereu (1992), studied a large data set of Fourier amplitudes in southeastern Canada. They performed a series of iterated hinged trilinear regressions and concluded that geometrical spreading in their study was independent of frequency and that the attenuation curves can be explained by a different geometrical spreading which is greater than body wave spreading at short distances, i.e. $c_1 > 1$. They also show that a bilinear form of geometrical spreading with a frequency dependent Q and a linear ($\frac{1}{r}$ for all distances) geometrical spreading with a constant $Q = 2000$ also provides a satisfactory fit to their data. For the Southern Great Basin data a bilinear form of r^{-1} for $r < 60$ km and r^{-c_2} , $0.75 > c_2 > 0.5$ results in a Q model that is close to the values calculated by Rogers *et al.* (1987). Our results differ from Rogers *et al.* (1987) in that they assumed that the main ground motion propagates as Lg waves and our interpretation of the wave propagation is quite different.

We summarize the results of regression analysis of the ground motion as measured by response spectra as follows:

1. A segmented geometrical spreading is preferred to explain the peak motion of S waves in the distance range of 0 to 200 km.

2. A uniform geometrical spreading of r^{-c} throughout the distance range leads to very large values and negative of Q for frequencies $f < 6\text{Hz}$.
3. Geometrical spreading at short distances is best described by r^{-1} .
4. Time-domain data is more sensitive to geometrical spreading parameters than similar frequency-domain data. Q values at lower frequencies; $f < 6$ Hz are more sensitive to c_2 and c_3 . Values of Q for frequencies higher than 6 Hz do not show great variation with c_2 and c_3 . c_2 varies between 0.5 to 0.7 and c_3 varies between 0.7 to 0.9.
5. Q values for the frequency range of 2 to 16 Hz are between 500 and 1400 indicating a moderate frequency dependence. A Q model of $Q \approx 600 f^{0.15}$ best describes our results for frequencies less than 8 Hz. For frequencies greater than 8 Hz, Q is more frequency dependent $Q \approx 150 f^{0.8}$

CHAPTER 4

CODA WAVE METHODS

4.1 Introduction

The tail of a seismogram that follows S waves is usually called the S-coda wave. Aki (1969), Aki and Chouet (1975), Rautian and Khalturin (1978), and many other investigators have utilized these waves to infer source path and site effect properties. The conclusions of these studies can be stated as follows:

1. The origin of coda is backscattering by heterogeneities distributed in the large region outside the zone of the path from the source to the receiver.
2. The power spectra of coda waves from different local earthquakes decays as a function of time (measured from the origin time of the earthquake) independent of the path between the source and the receiver.
3. The envelope of the coda as a function of time is independent of the source spectrum.
4. The coda excitation is a function of local geology of the receiver site. It can be up to eight times larger on sediment than on granite (Aki, 1969).

These properties can be expressed by the following relation for the power spectrum of coda waves at time t measured from the origin time:

$$P(f,t) = I^2(f) S^2(f) Z^2(f) t^{-n} \exp[-2\pi ft/Q]. \quad (4.1)$$

t^{-n} arises from the geometrical spreading consideration. For single scattering of body waves, $n = 2$, for surface waves $n = 1$, and for diffusion, $n = 1.5$ (Aki, 1969; Aki and Chouet, 1975; Kopynichev, 1975; and Rautian, 1976). The fractional loss of energy per cycle is $\frac{2\pi}{Q}$, and the apparent attenuation in power during the time period t is $\exp\left(-\frac{2\pi ft}{Q}\right)$. $I(f)$, $S(f)$ and $Z(f)$ express the effects of the instrument, the earthquake source and the site geology, respectively.

The amplitude of the coda waves at any given frequency is only a function of the total travel time,

$$A_c(f,t) = I(f) S(f) Z(f) \Phi(f,t). \quad (4.2)$$

$\Phi(f,t)$ then will be the same for all records if it is measured at the same frequency and t_c is greater than twice the shear wave travel time, t_s . In terms of (4.2), which is valid for $t_c > t_s$ the seismic coda is homogeneous in space. In other words, the difference in coda amplitude observed at two stations is attributed to the differences in site response and instrument response. A division of S-wave

amplitude by the coda amplitude can be used to clear any non-propagation effect, i.e. common source, site, instrument, and to compare only the path effect for each seismogram. This method, originally proposed by Aki (1980), was used by Frankel *et al.* (1990) as a tool to measure the attenuation of the direct high-frequency shear waves in New York State, South Africa, and California. In this chapter we will calculate the quality factor Q of the coda waves using the single scattering model. We will demonstrate that for our area of study, the Q measurement is relatively insensitive to lapse time. For a fixed lapse time we will calculate the attenuation and Q of shear waves for a frequency range of 2 to 16 Hz. The discussion as to why the spatial attenuation observed in Chapter 3 is different from temporal attenuation obtained from the coda of a single station will be postponed to Chapter 5.

4.2 Coda Q method

Coda Parametrization

The power spectrum of a band-passed signal with $P(f, t) = P$ (constant) for $f_2 < |f| < f_1$, and $P(f, t) = 0$ otherwise, can be approximated by

$$\langle a^2(t, f) \rangle = 2P(f, t) \Delta f \quad (4.3)$$

where $\langle a^2(t, f) \rangle$ is the mean square of the time series. If $A(f, t)$ represents twice of the root mean square of the signal, then

$$A(f, t) = 2 \sqrt{\langle a^2(f, t) \rangle} = 2 \sqrt{2P\Delta f} \quad (4.4)$$

and Equation (4.1) leads to

$$A(f, t) = 2 I(f) S(f) Z(f) (2 \Delta f)^{\frac{n}{2}} t^{\frac{-n}{2}} e^{\frac{-\pi f t}{Q}}. \quad (4.5)$$

After taking the logarithm of both sides and incorporating all the constant terms into an equivalent source term $S(f)$, this equation can be written as

$$a_{ijk}(f) = S_j(f) + C_i(f) - n \log_{10} t_{ijk} - \frac{\pi f t_{ijk}}{Q} \log_{10} e, \quad (4.6)$$

where i and j indices represent receiver and earthquake, respectively. The index k represents the lapse time used. i.e. for i 'th station of the j 'th earthquake we will notice several lapse times and different corresponding amplitudes. The lapse time used in this analysis and most coda studies is usually taken to be greater than twice the S-wave travel-time. In matrix form (4.6) can be written as

$$\mathbf{d} = \mathbf{M} \mathbf{x}. \quad (4.7)$$

The matrix \mathbf{M} in this case will be substantially larger in dimension than the one used for the regression of response spectra data. because of the many time windows used. There will be K rows (K number of time intervals for each record) per station per event. The matrix \mathbf{M} is

8.6 km. The distance range for these records are from 15 to 52 km. Figure 4.1b shows seismograms of a 9.8 km deep earthquake with epicentral distance range of 50 to 153 km. In Figure 4.1c we show a shallow earthquake with depth of 0.5 km. The epicentral distances of the six records shown range from 120 km to 190 km. The coda lengths are usually shorter than 50 seconds but they are long enough for our coda wave analysis. Each time history was passed through a narrow-bandpass Butterworth filter. The center frequencies were $f_c=2,3,4,6,8,10,12,14$, and 16 Hz, and the highpass and the lowpass cut were given by $f_{low} = 0.707f_c$ and $f_{high} = 1.414f_c$. The bandpassed data then were corrected for the instrument response at the filter center frequency. A moving window of 5 sec was recorded with 5% overlap being used to determine the coda average amplitude. The rms band-passed noise corrected for the instrument was subtracted from the rms of the moving window. Only time windows with lapse times greater than twice the S wave travel time were used. This data base for the entire 450 records was inverted according to the inversion technique discussed in Chapter 3.

4.3 Coda Q measurements

Table 4.1 gives the values of Q computed at different frequencies by assuming that $n = 2$ in (4.1). The results show remarkable stability of the solutions. The standard deviations are very small. Q, as a function of frequency, can be written as

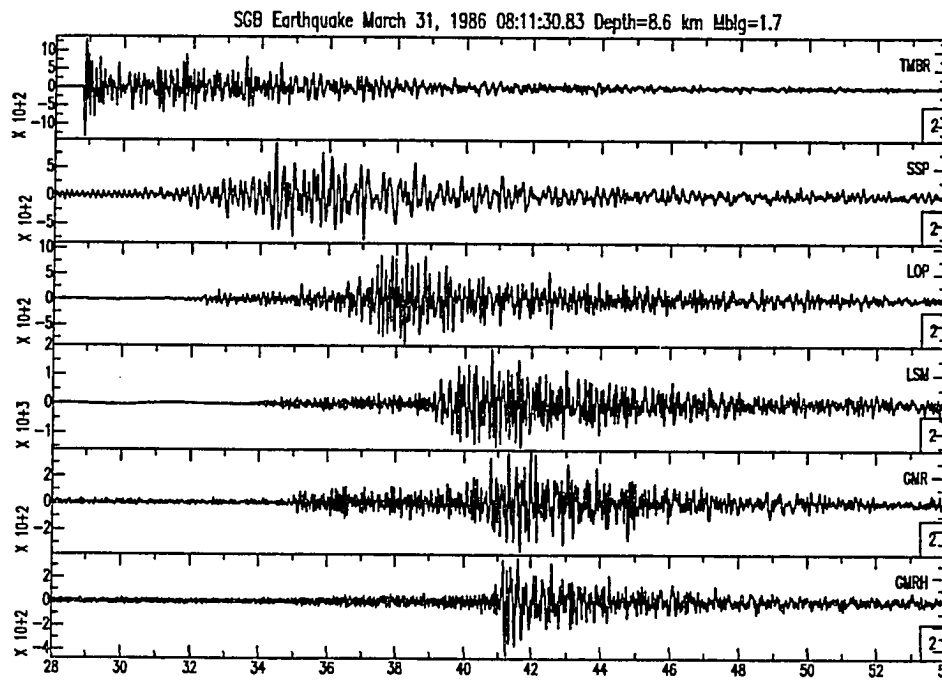


Figure 4.1a. Seismograms of earthquake 5 of Table 1.1 recorded at six stations with epicentral distances of 16 km, on the top, to 56 km, on the bottom.

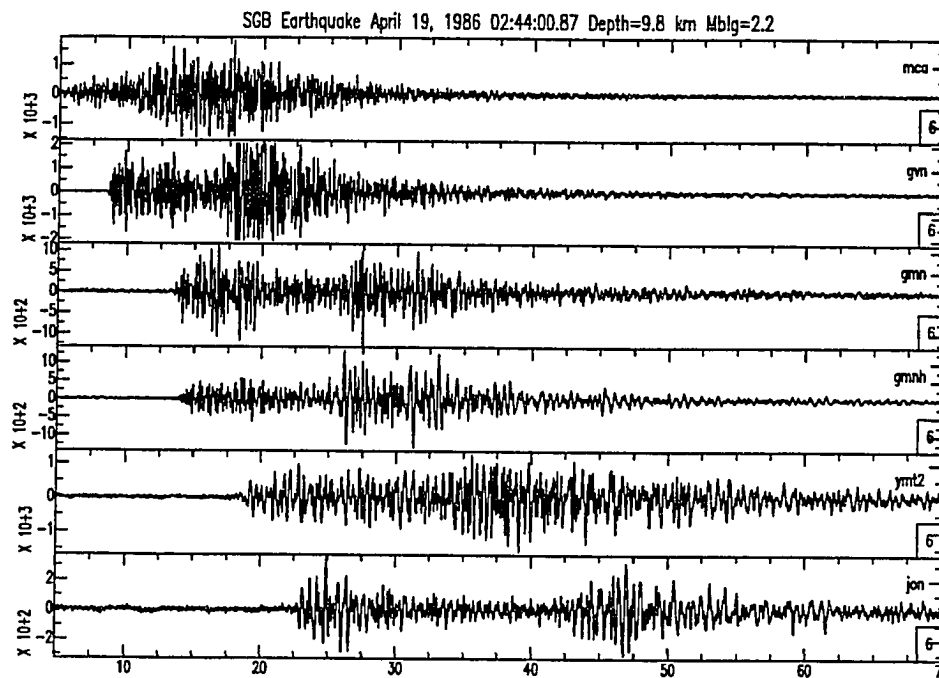


Figure 4.1b. Seismograms of earthquake 17 of Table 1.1 recorded at six stations with epicentral distances ranging from 48 km, on the top, to 153 km, on the bottom.

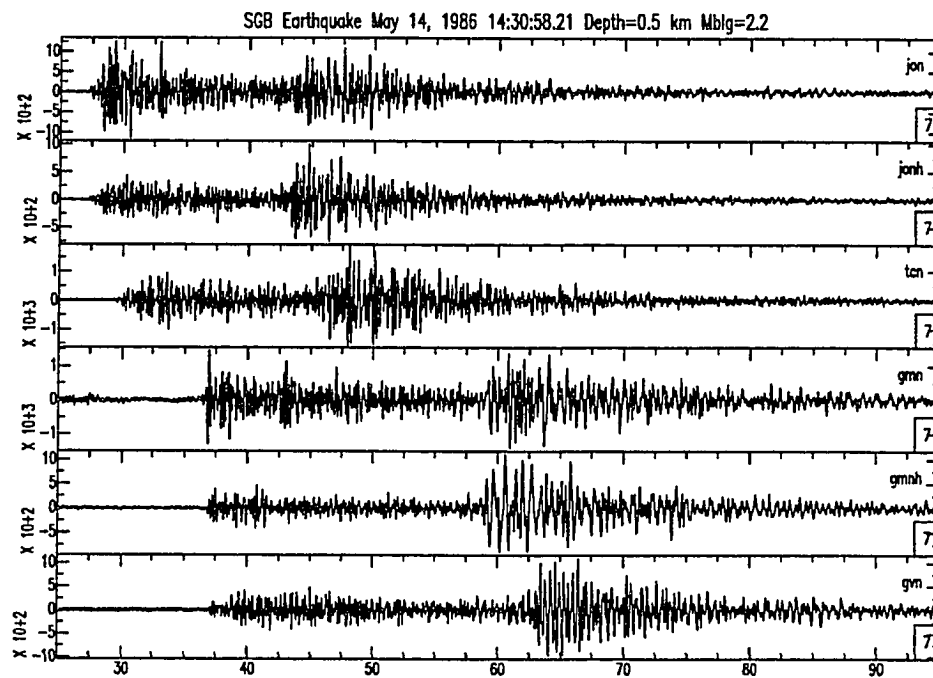


Figure 4.1c. Seismograms of earthquake 31 of Table 1.1 recorded at six stations with epicentral distances ranging from 120 km, on the top, to 187 km, on the bottom.

$$Q = 150 f^{0.9}, \quad (4.8)$$

in sharp contrast to the Q calculated from our peak motion studies which were approximately $Q(f) = 700 f^{0.2}$. We will discuss the reasons for this difference later. We repeated the process using amplitudes only after 2.5 times the S wave travel time. There are no significant change in values of Q .

4.4 Q of S waves using coda normalization method

The spectral amplitude $A_s(f,r)$ of the shear wave (S or Lg) can be expressed as

$$A_s(f,r) = R_{\theta\phi} I(f) S(f) Z(f) r^{-n} e^{-\pi f r / Q \beta}. \quad (4.9)$$

Here f is the frequency, r is hypocentral distance, $R_{\theta\phi}$ is the radiation pattern, β is the average S wave velocity, $S(f)$ the source excitation, $Z(f)$ represents the site amplification, and n is the exponent of the geometrical spreading factor. Q here represents the effective Q of the crust and may be caused by scattering or anelasticity, or both. The coda wave spectral amplitude $A_c(f,t_c)$ at time t_c after the origin time of the earthquake can be represented as

$$A_c(f,t_c) = I(f) S(f) Z(f) \Phi(f,t_c) \quad (4.10)$$

where $\Phi(f,t)$ represent the coda envelope that describe the decay of coda amplitude with lapse time on the seismogram. Empirically, it has been established that the coda envelope function of $\Phi(f,t_c)$ is

TABLE 4.1**Coda Q values of the Southern Great Basin**

Freq (Hz)	Q ± δQ
2	292.7 7.2
3	317.1 5.5
4	392.1 6.4
6	569.6 9.4
8	753.5 12.8
10	962.0 17.1
12	1214.2 24.0
14	1517.5 34.1
16	1866.7 46.5

independent of the source, site, and the distance between the source and the site, for t_c greater than twice the direct S time (Aki, 1969; Aki and Chouet, 1975). Later in this work, we will demonstrate that the site amplification term $Z(f)$ is the same for the direct shear waves and the coda waves. This is also confirmed by the earlier work of Tsujiura (1978).

Dividing (9) by (10), we find that

$$A_s(f,r)/A_c(f,t_c) = R_{\theta\phi} r^{-n} e^{-\pi r/Q\beta} / \Phi(f,t_c). \quad (4.11)$$

Our approach in this study is to combine all the normalized amplitudes from different earthquakes recorded at different stations on a single plot. This is done for frequencies from 2 Hz to 16 Hz. The coda normalization method does not remove $R_{\theta\phi}$, which represents a composite radiation pattern of the rays with different takeoff angles. A combined representation of the normalized amplitude will average out the radiation pattern term.

We band-pass the seismograms using narrow band-pass zero-phase Butterworth filters for frequencies of 2 to 16 Hz. For each filtered trace, a root mean squared amplitude in a 5 second moving window from the onset of S wave to the end of the seismograms is computed. This represents the amplitude of the envelope of the seismogram $A(t)$. We assume that the maximum amplitude of the envelope, is representative of the peak amplitude of direct S

or Lg phase, $A_s(f,r)$. Here f is the center frequency of the band-pass filter. The coda amplitude is determined by sampling the envelope at some later time, t_c . For this method to work, all stations recording a given earthquake must be normalized using the same t_c time. Of course t_c may be different for different data sets. There are cases that the signal to noise ratio is small for $A_c(f,t_c)$ for $t_c > 2t_s$. For these cases shorter t_c were used. In other cases, where the hypocentral distance is short for some seismograms, the coda amplitudes approaches the noise level after 30 seconds. Yet in many other cases the recording stops at 100 seconds and this would not allow the coda waves of greater than $2t_c$ to be recorded. Following Aki (1980) we introduce a correction factor into the coda amplitude measured at t_c to extrapolate all the measurements and to bring them to the same reference time, t_{ref} .

This is done by extrapolating the coda envelope formula from t_c to t_{ref}

$$A_c(f, t_{ref}) = (t_c/t_{ref})^n \exp[-f(t_{ref}-t_c)/Q_c] A_c(f, t_c) , \quad (4.12)$$

where Q_c are values of coda Q from Table 4.1 and $n = 1$ for the coda.

We plot the coda normalized S wave amplitudes at frequencies 2, 3, 4, 6, 8, 10, 12, 14, and 16 Hz for the Southern Great Basin Seismic Network against distance in Figure 4.2. We note that for

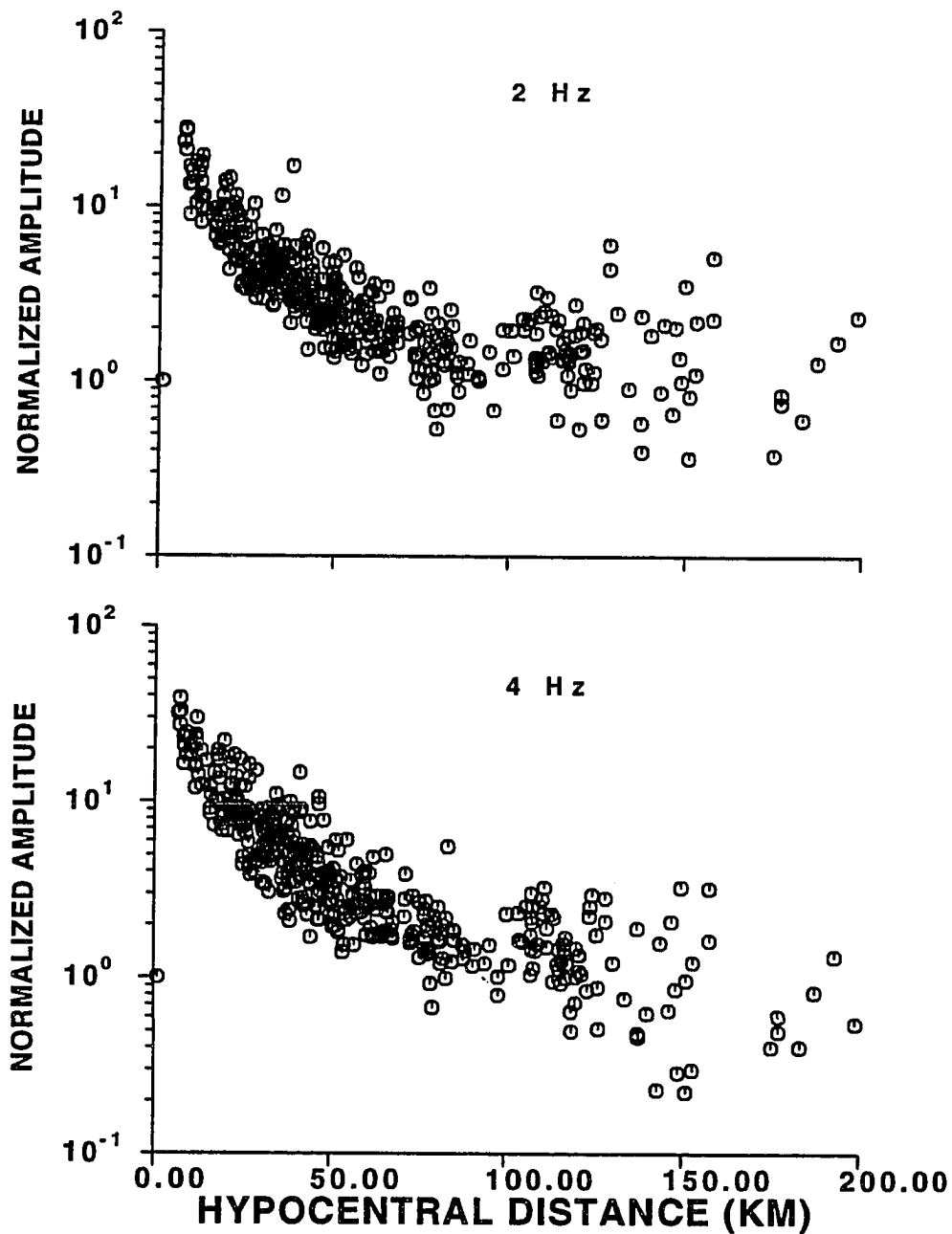


Figure 4.2a. Coda normalized amplitudes versus distance for 2 Hz, on top, and 4 Hz on the bottom.

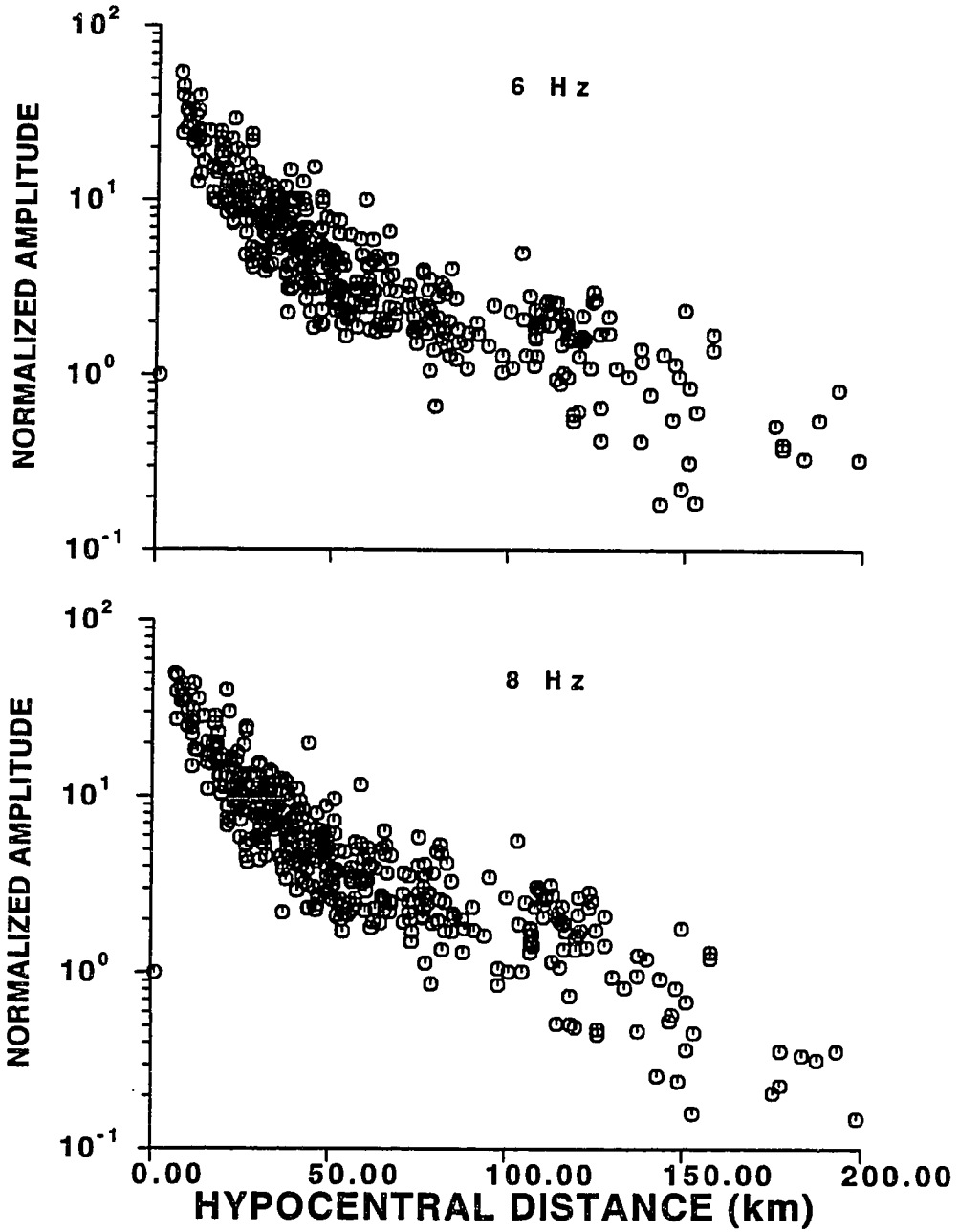


Figure 4.2b. Coda normalized amplitudes versus distance for 6 Hz and 8 Hz.

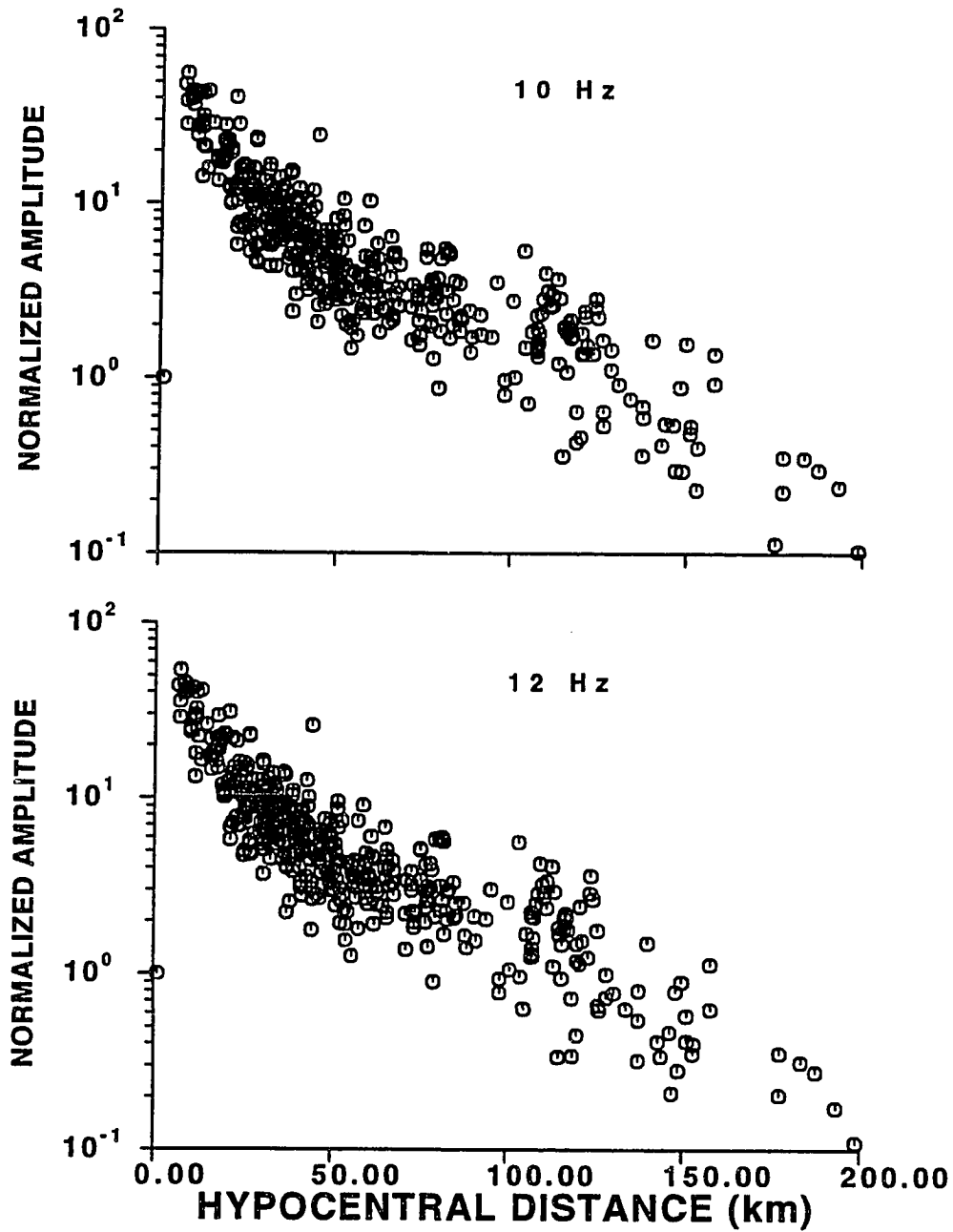


Figure 4.2c. Coda normalized amplitudes versus distance for 10 Hz and 12 Hz.

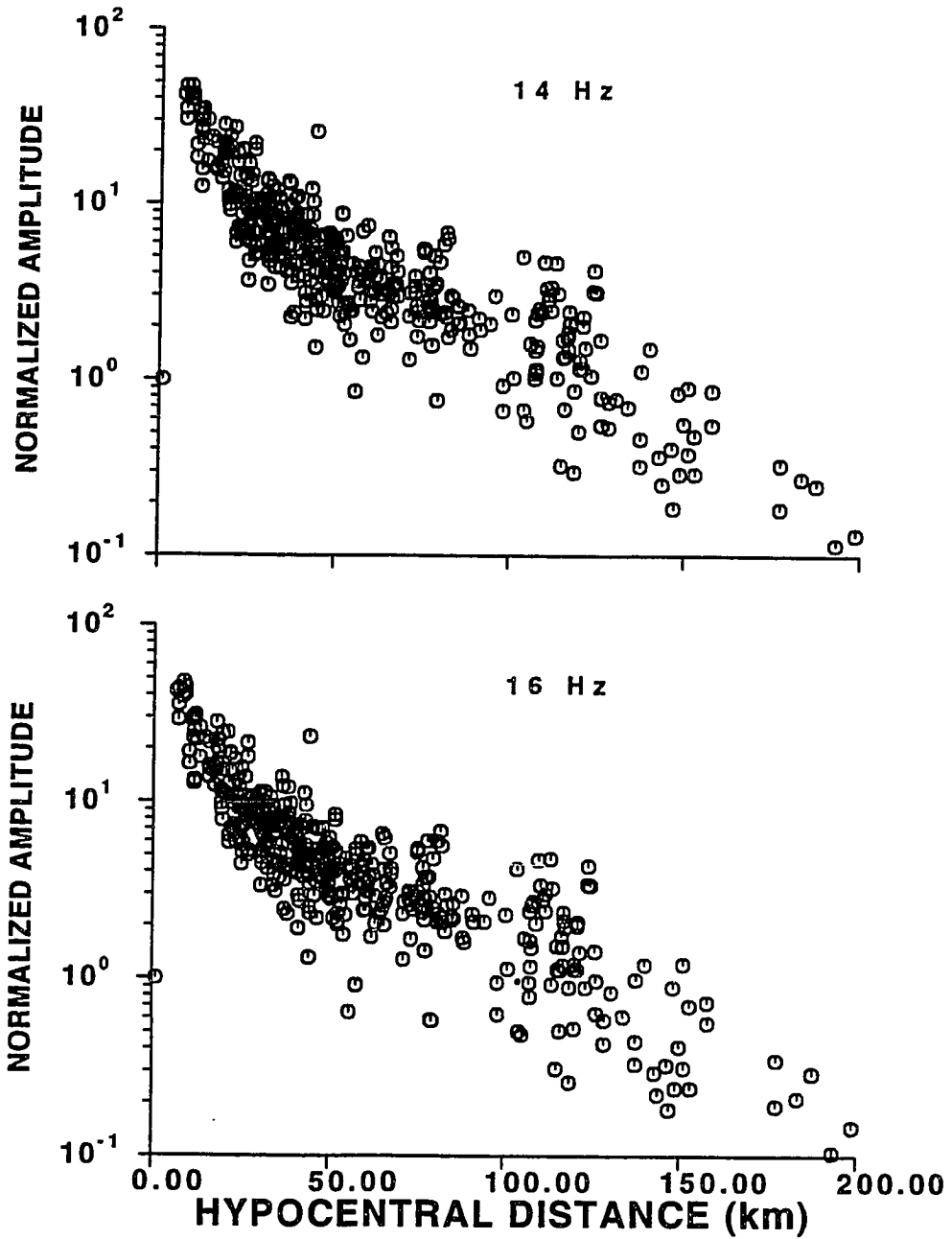


Figure 4.2d. Coda normalized amplitudes versus distance for 14 Hz and 16 Hz.

filter frequencies of 2, 3 and 4 Hz there is an apparent change in the slope at a distance of about 60 km. The amplitudes decrease rapidly as hypocentral distance increases up to 60 km. The decay rate moderates between 80 to 120 km, there is a local peak at 120 km, and after 120 km the normalized amplitude decays more rapidly. Reflection from the Moho probably contributes to this change of character of amplitudes. For frequencies greater than 4 Hz, the amplitude-distance plots decay uniformly and the change of slope is less noticeable.

4.5 Parametrization of the attenuation problem

We parametrize the attenuation of the main ground motion in the distance range of 1 to 200 km using a frequency-dependent Q . Our previous regression methods resulted in an attenuation model moderately dependent on frequency which means the quality factor Q is function of frequency. In a similar study, Frankel *et al.* (1990) assumed a frequency-independent Q . This study differs from others in the sense that we allow the geometrical spreading exponent of c in r^{-c} to take different values in the three distance ranges. The normalized amplitude data show changes in the character of spatial attenuation for hypocentral distances less than about 60 km, between 60 km and 120 km and greater 120 km. We allow three different c values related to these critical distances, $d_1 = 60$ km and $d_2 = 120$ km.

The new equation is written to preserve continuity of amplitude versus distance.

$$\begin{aligned}
 \ln A_i(f_j) &= b_j - \frac{\pi f_j r_{ij}}{\beta Q(f_j)} - c_1 \ln r_{ij} && \text{for } r_{ij} \leq d_1 \\
 \ln A_i(f_j) &= b_j - \frac{\pi f_j r_{ij}}{\beta Q(f_j)} - c_1 \ln d_1 - c_2 \ln \frac{r_{ij}}{d_1} && \text{for } d_1 < r_{ij} \leq d_2 \\
 \ln A_i(f_j) &= b_j - \frac{\pi f_j r_{ij}}{\beta Q(f_j)} - c_1 \ln d_1 - c_2 \ln \frac{d_2}{d_1} - c_3 \ln \frac{r_{ij}}{d_2} && \text{for } r_{ij} > d_2 .
 \end{aligned} \tag{4.13}$$

In (4.13) $A_i(f_j)$ represents the i 'th normalized amplitude for frequency f_j , r_{ij} is the source-receiver distance for the i 'th amplitude measurement at frequency f_j , b_j is the y -intercept on the plots of amplitude versus distance, and β is the average shear wave velocity of the medium here taken to be 3.2 km/s. Notice that the model solution of this matrix equation yields frequency-dependent Q , geometrical spreading parameters segmented into three distance ranges, and intercepts which are function of frequency. The equation can also be reduced to the case of frequency-independent Q . For the case of a frequency-independent model with geometrical attenuation of $\frac{1}{r^n}$ in the distance range of $d_2 > r \geq d_1$, the matrix equation for two frequencies, f_1 and f_2 can be written as

$$\begin{bmatrix}
 -\pi f_1 r_{11}/\beta & -\ln r_{11} & 1 & 0 \\
 -\pi f_1 r_{21}/\beta & -\ln r_{21} & 1 & 0 \\
 \cdot & \cdot & \cdot & \cdot \\
 \cdot & \cdot & \cdot & \cdot \\
 -\pi f_2 r_{12}/\beta & -\ln r_{12} & 0 & 1 \\
 -\pi f_2 r_{22}/\beta & -\ln r_{22} & 0 & 1 \\
 \cdot & \cdot & \cdot & \cdot \\
 \cdot & \cdot & \cdot & \cdot
 \end{bmatrix}
 \begin{bmatrix}
 Q^{-1} \\
 n \\
 b_1 \\
 b_2
 \end{bmatrix}
 =
 \begin{bmatrix}
 \ln A_1(f_1) \\
 \ln A_2(f_1) \\
 \cdot \\
 \cdot \\
 \ln A_1(f_2) \\
 \ln A_2(f_2) \\
 \cdot \\
 \cdot
 \end{bmatrix}
 \quad (4.14)$$

where b_1 and b_2 are the intercepts of the plots of amplitudes versus distance for frequencies f_1 and f_2 , respectively.

4.6 Attenuation measurements

We apply the matrix inversion to the data comprising of 470 records of 41 events in the SGBSN. We disregard those recordings where the noise level of the signal before the onset of P arrival is equal to or greater than twice of the coda amplitude measured at t_c . t_{ref} is chosen to be equal to 30 seconds. The matrix inversion based on the stochastic inverse method is performed for all frequencies from 2 Hz to 16 Hz simultaneously. We estimate attenuation using a frequency-dependent Q as well as a frequency-independent Q .

Frequency-dependent Q model. A frequency-dependent Q model will result from inversion of matrix equation (4.13). A uniform geometrical spreading model of $\frac{1}{r^c}$ for all distance ranges resulted in very large to negative values of Q for frequencies less than 6 Hz. A bilinear and a trilinear geometrical spreading therefore seemed

more suitable, as is obvious from Figure 4.2. When we tried a trilinear regression, values of geometrical spreading for $r > 120$ km converge to $\frac{1}{r^2}$ which is a much larger geometrical attenuation than all theoretical models predict for the Lg wave in this distance range. A geometrical spreading of $r^{-0.83}$ for $r > 120$ km was forced and the Q values were calculated. Table 4.2 shows the trilinear Q values along with the Q values for a bilinear regression with the critical distance of $r_c = 60$ km. The values calculated from the bilinear fit are very close to the bilinear regression of SV in Chapter 3 with the geometrical spreading of $\frac{1}{r}$ for $r < 60$ km and $\frac{1}{r^{0.58}}$ for $r > 60$ km. Figure 4.3 shows the bilinear fit to the coda normalized data.

We also calculated Q and geometrical for the direct S waves for distance range $r \leq 60$ km assuming a uniform geometrical spreading of $\frac{1}{r}$. Q values, listed in Table 4.3 are highly frequency dependent and are very close to Q_c .

Frequency-independent Q model. We calculated attenuation based on a frequency-independent Q model of (4.14). We found that a constant $Q=1660$ with geometrical spreading of $\frac{1}{r^{0.98}}$ provides a reasonable fit. If we fix the the geometrical spreading at $\frac{1}{r}$ a constant $Q=1550$ is the preferred model. Figure 4.4 shows the Q-geometrical

TABLE 4.2**Q of the coda normalized S-wave data**

Freq (Hz)	Q \pm δ Q		Q \pm δ	
	Trilinear fit		Bilinear fit	
2	585	125	1913	1480
3	417	42	624	105
4	448	37	610	75
6	553	37	708	68
8	641	38	792	64
10	765	43	935	71
12	894	49	1087	80
14	1042	57	1266	93
16	1205	66	1467	109

Trilinear: $c_1=1.$, $c_2=0.22 \pm 0.07$ and $c_3=0.83$

Bilinear: $c_1=1.$ and $c_2=0.59 \pm 0.07$

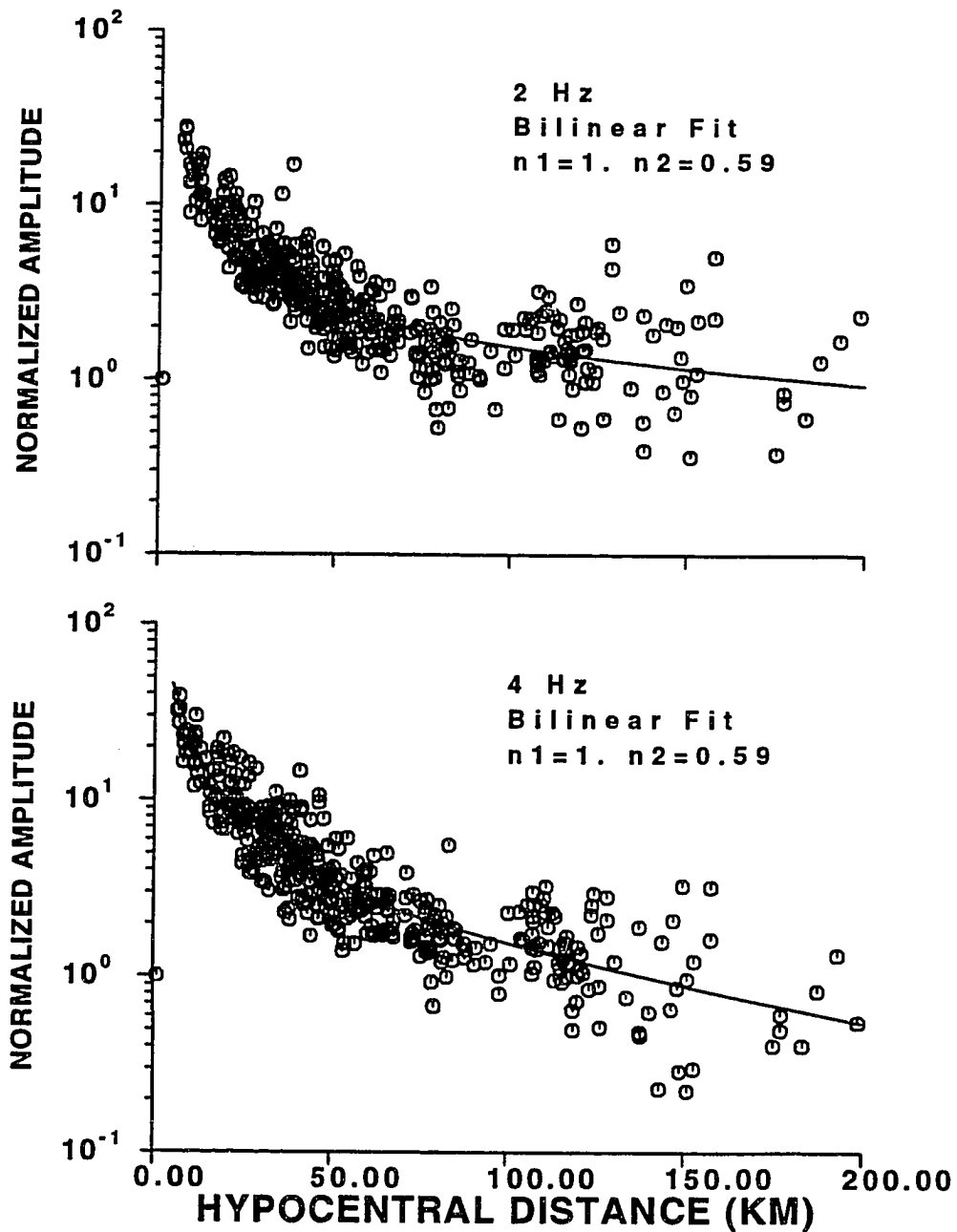


Figure 4.3a. Bilinear regression fit to the coda normalized data for 2 Hz and 4 Hz. Values of geometrical spreading for the two distance ranges are shown.

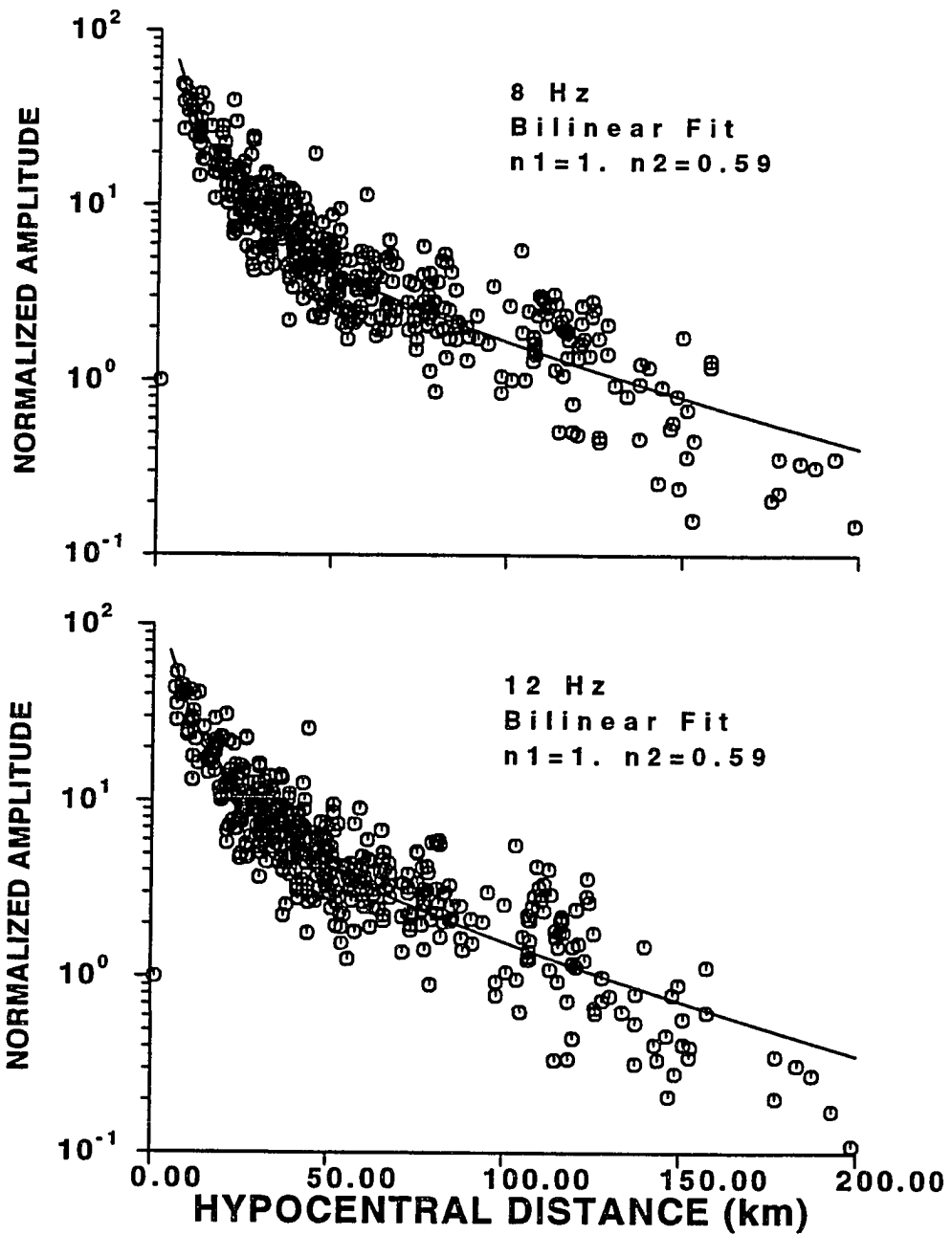


Figure 4.3b. Same as Figure 4.2b but for 8 Hz and 12 Hz.

TABLE 4.3
Q values of direct S-wave

Freq (Hz)	$Q \pm \delta Q$	
2	322	113
3	415	125
4	521	148
6	627	143
8	732	146
10	956	199
12	1183	254
14	1402	306
16	1629	363

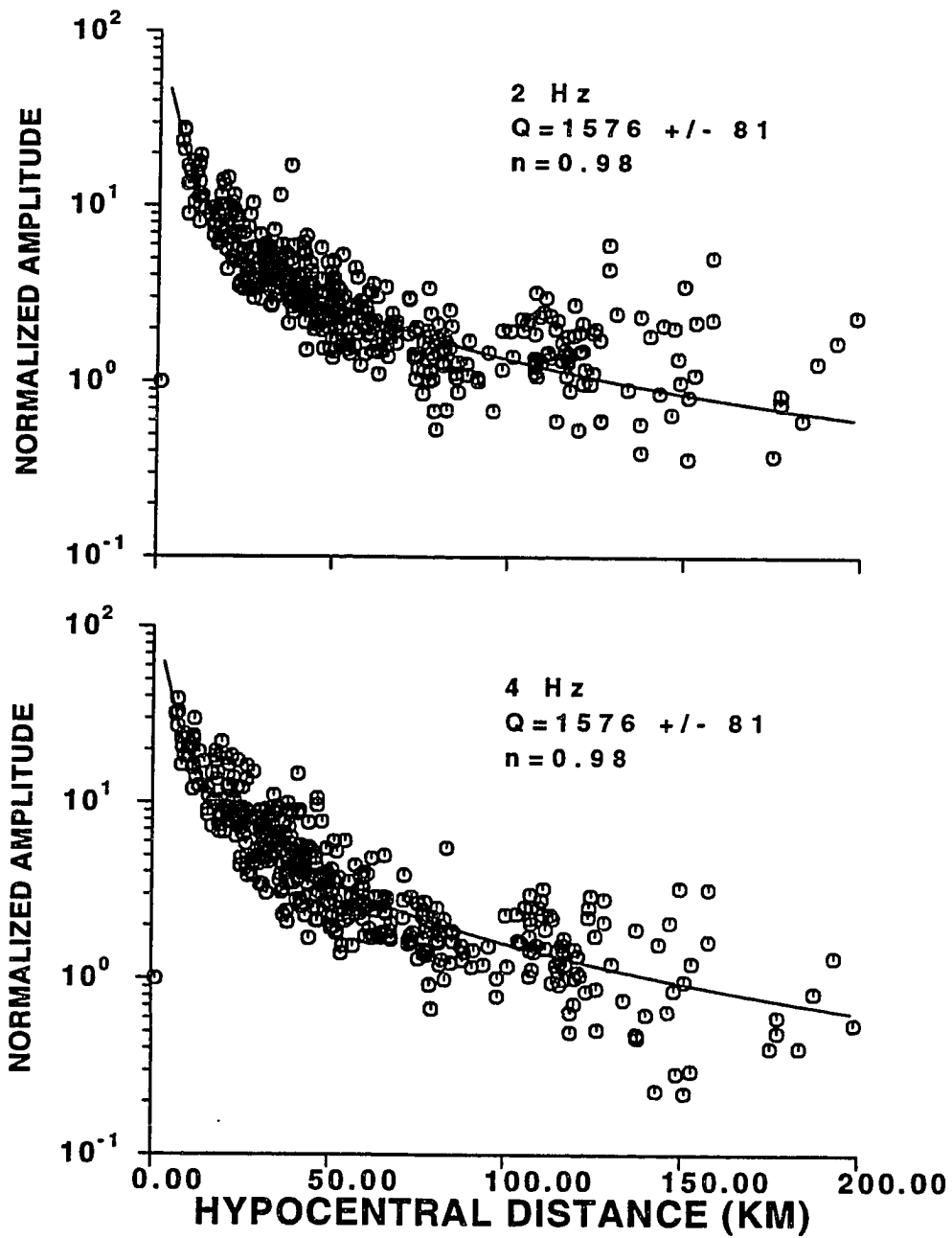


Figure 4.4a. Frequency independent Q model fit to the coda normalized amplitude data for 2Hz and 4 Hz.

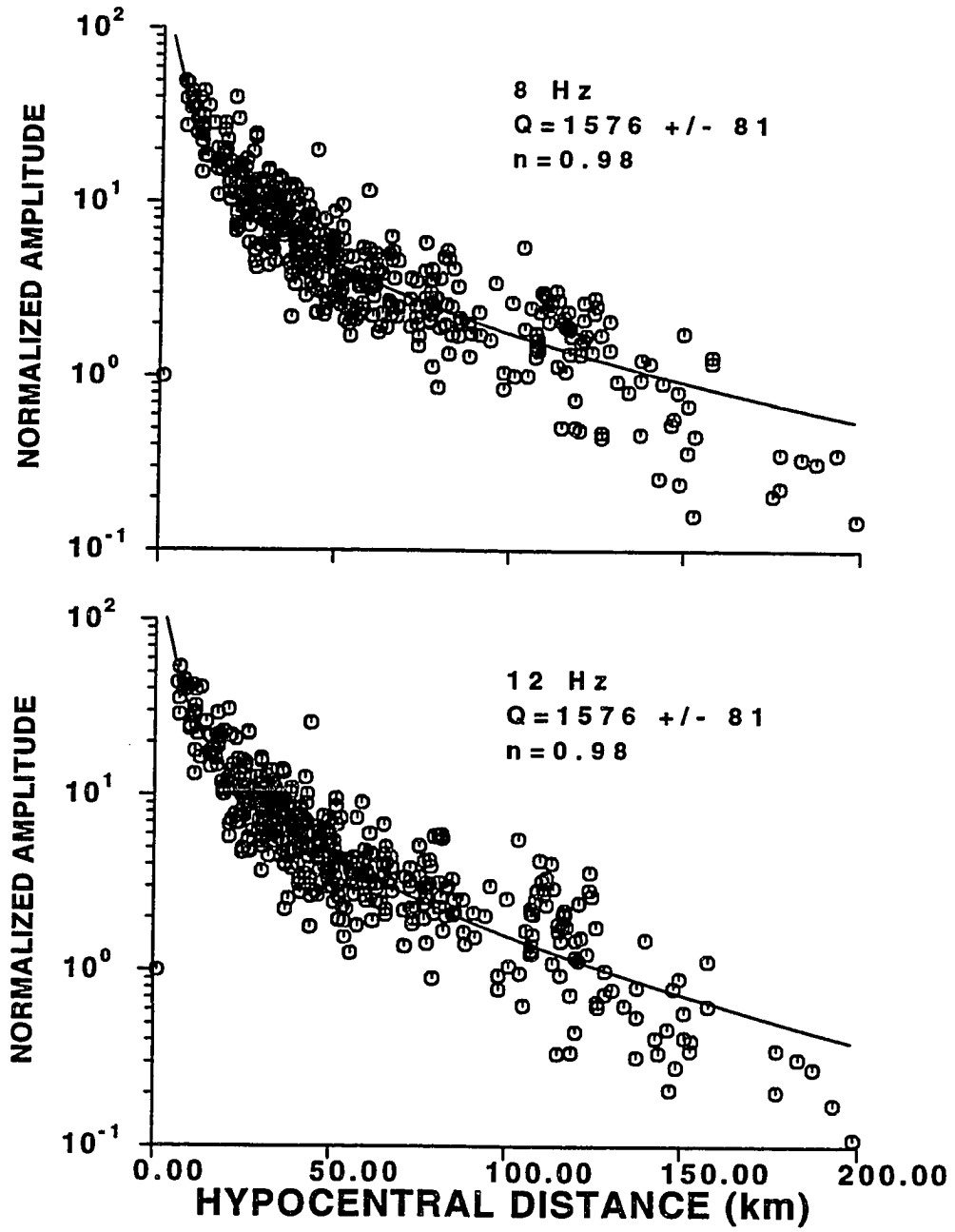


Figure 4.4b. Same as Figure 4.2a but for 8 Hz and 12 Hz.

spreading model fit with the data for frequencies 2,4,8, and 12 Hz. For the direct S waves, a constant $Q=1122 \pm 96$ fits the data best for $r < 60$ km. For $120 \text{ km} > r > 60 \text{ km}$, a $Q = 1414 \pm 239$ with the geometrical spreading of $\frac{1}{r^{0.55}}$ is the best fit.

4.7 Discussion and conclusions

The coda Q values calculated based on the Single Scattering Model are lower than apparent values of Q from the regression analysis of the main ground motion for frequencies less than 6 Hz. For frequencies 2 Hz and 3 Hz, Q_c are less than half of Q_{sv} . For frequencies greater than 12 Hz, the coda values are slightly higher than the Q values of the main ground motion. Many investigators have reported that the coda Q values measured from the decay of corrected amplitudes of the coda versus time increase with lapse-time. For lapse-times of 20 to 90 seconds, the coda Q is independent of lapse-time in the Southern Great Basin measurements.

In a study by Rogers *et al.* (1987), calculated Q_{Lg} values are generally very high for frequencies less than 6 Hz and are relatively frequency- independent. Their Q values are very large and physically unacceptable for $f < 3\text{Hz}$ if the geometrical spreading is assumed $\frac{1}{r}$. Our conclusion, as in Chapter 3, supports our general

conclusion that any network data that covers a distance range from few kilometers to few hundred kilometers cannot be used in a simple regression with the assumption of uniform geometrical spreading attenuation and frequency-dependent Q . A distance-dependent geometrical corresponding to body wave spreading from 0 to 60 km and surface waves spreading at distances greater than 60 km yields Q values moderately dependent on frequency if Q is expressed as $Q = Q_0 f^\eta$ then $Q_0 \approx 600$ and $\eta \approx 0.2$. This is in agreement with the results from the bilinear and trilinear regressions of the S waves where source and site were free variables. In addition, the agreement of these results also support the coda normalization method. A frequency-independent Q value of $Q = 1661 \pm 54$ with geometrical spreading of $\frac{1}{r}$ for $0 < r < 200$ km gives very satisfactory fit to the data. Frankel *et al.* (1990) applied a similar approach for attenuation of S waves with a single geometrical spreading of $\frac{1}{r^\eta}$ for New York State, southern California, and South Africa. Attenuation of S waves for distances less than 90 km is well described by a frequency-independent $Q = Q_0$. They found $Q_0 = 2100$ with $\eta = 1.3$ for New York State, $Q_0 = 1500$ and $\eta = 1.3$ for South Africa, and $Q_0 = 800$ with $\eta = 1.9$ for southern California. The Southern Great Basin results resemble those of South Africa.

Attenuation calculated for the direct S waves is greater than

that calculated for peak amplitudes of the S waves dominating the seismogram of locally recorded earthquakes. The immediate explanation is that the direct S waves suffers scattering during its propagation. In the distance range of $r < 60$ km, the intrinsic attenuation effect has a limited effect and scattering from small size heterogeneities can play a major role in diminishing amplitude strength. Most scattering models predict the coda wave attenuation as being dominated by intrinsic attenuation (Frankel, 1990; Wu and Aki, 1988). The results in this chapter and the next chapter support a model of the coda attenuation which is equally dominated by scattering and anelastic attenuation for frequencies less than 8 Hz and by anelastic attenuation at higher frequencies.

We summarize the results of the coda wave analysis as follows:

1. The coda Q values for the Southern Great Basin are highly frequency dependent and with $Q = 150 f^{0.9}$.
2. The coda normalized S waves amplitudes attenuate similar to the response spectra.
3. A bilinear regression of the coda-normalized data results in Q values ranging from 500 to 1500 for frequencies 3 Hz to 16 Hz. The geometrical spreading factor was determined to be r^{-1} for distances less than 60 km and $r^{-0.59}$ for distances greater than 60 km.

3. A frequency-independent $Q = 1576$ with the geometrical spreading of r^{-1} gives a reasonable fit to the data.
4. The direct S waves Q values are closer to the coda Q values. A frequency-independent $Q = 1122$ is the preferred model for the direct S waves.

CHAPTER 5
ATTENUATION, SCATTERING, AND CODA Q FOR THE
SOUTHERN GREAT BASIN BETWEEN 2 AND 16 HZ

5.1 Introduction

The ground motion A at frequency f of distance r from the source can be described by the equation

$$A(r,f) = S(f) Z(f) G(r) e^{-\pi fr/Qv}. \quad (5.1)$$

In (5.1) S represents the signal excitation by the source and v is the seismic wave velocity. The factor $G(r)$ represents the geometrical spreading due to the propagation of motion in a perfectly elastic medium without random scattering. The exponential decay term describes the effect of attenuation due to anelastic attenuation of the medium and random scattering. More recent theories of wave scattering in absorbing and heterogeneous media indicate that the spectral density, as defined by energy per unit solid angle, of waves propagated through a medium, varies with distance in a much more complicated manner when multiple scattering is considered (Wu, 1984, 1985; Wu and Aki, 1988). The shape of the intensity-distance curve is controlled by seismic albedo B_0 of the medium defined as

$$B_o = \frac{\eta_s}{\eta_e} = \frac{\eta_s}{\eta_s + \eta_a}, \quad (5.2)$$

where η_a is the energy absorption coefficient due to anelasticity and η_s is the scattering coefficient. η_s is defined as the total scattered power by a unit volume of random medium per unit incident power flux density. For a perfect scattering medium $B_o=1$ and for a purely absorbing medium with no scattering $B_o=0$.

In practice, the measurement of Q is usually based on modeling data by an equation of the form of (5.1). This operational definition of Q may not be the same as the physical definition of Q and measurements based on (5.1) may result in different values. If a short pulse travels through a medium in which both scattering and anelasticity occur, then the total Q_t is (Dainty, 1981)

$$Q_t^{-1} = Q_i^{-1} + Q_s^{-1}, \quad (5.3)$$

where Q_s^{-1} is due to scattering and Q_i^{-1} is intrinsic attenuation due to anelasticity of medium. The loss of energy due to scattering and anelasticity can be described by

$$Q_s^{-1} = k^{-1}\eta_s \text{ and } Q_i^{-1} = k^{-1}\eta_a, \quad (5.4)$$

where k is the wavenumber. Unless some model for each of the two Q components is used they cannot be separated.

The scattered energy represented by Q_s is only redistributed and not lost from the wavefield. Measurements of Q which examine

a substantial time window of the seismogram will include some of this energy. Here we present two methods of measurement of Q by examining a large time window of the seismogram. In both approaches, Wu's (1985) method, based on the Radiative Transfer Theory (Ishimaru, 1978) allows an estimation of the relative contribution of scattering and anelastic attenuation from the dependence of the total S-wave energy on hypocentral distance. Our first method is based on the energy density calculated from the Fourier spectrum of a large time window of seismogram (Wu and Aki, 1988; Mayeda *et al.*, 1991; McSweeney *et al.*, 1991). The other approach measures energy density using an interpretation of the attenuation of ground motion. Toksöz *et al.* (1988) applied this method for the strong ground motion data in the northeastern United States and eastern Canada.

5.2 Review of the Radiative Transfer Energy Theory

The Radiative Transfer Energy Theory is based on the earlier work of Chandrasekhar (1960) and Ishimaru (1978). Wu (1985) derived an equation for the normalized energy distribution of seismic waves in a randomly inhomogeneous medium for an isotropic point source with unit energy,

$$4\pi r^2 E(r) = \eta_e P_d r \exp(-\eta_e d_o r) + \eta_e r \int_0^1 f(\xi, B_o) \exp(-\eta_e r/\xi) d\xi / \xi^2 \quad (5.5)$$

$$=4\pi r^2(E_d+E_c) ,$$

where P_d and $f(\xi, B_o)$ are defined as

$$P_d = \frac{2d_o^2(1-d_o^2)}{B_o(d_o^2+B_o-1)} ,$$

where d_o is defined by the relation

$$\frac{B_o}{2d_o} \ln \left(\frac{1+d_o}{1-d_o} \right) = 1$$

and

$$f(\xi, B_o) = [(1-B_o\xi \tanh^{-1}\xi)^2 + \left(\frac{\pi}{2} B_o \xi \right)^2]^{-1}.$$

The first term in (5.5) is the diffusive term $4\pi r^2 E_d$ a contribution due to the multiple scattering. The second term is the coherent term $4\pi r^2 E_c$, which represents the coherent part of the energy density.

In Figure 5.1, the normalized energy $4\pi r^2 E(r)$ is plotted versus distance for the extinction length $L_e = 30$ km, where L_e is defined by $L_e = \frac{1}{\eta_e}$. If there is no scattering and absorption, $4\pi r^2 E(r)$ should be a constant line having a value equal to 1. For a purely absorbing medium, $B_o=0$ and the energy decreases as a straight line on a semilogarithmic plot. In the presence of scattering, the energy distribution curve deviates from a straight line and becomes B_o -dependent. A careful matching of observed energy-distance and the theoretical model based on (5.5) can be used to

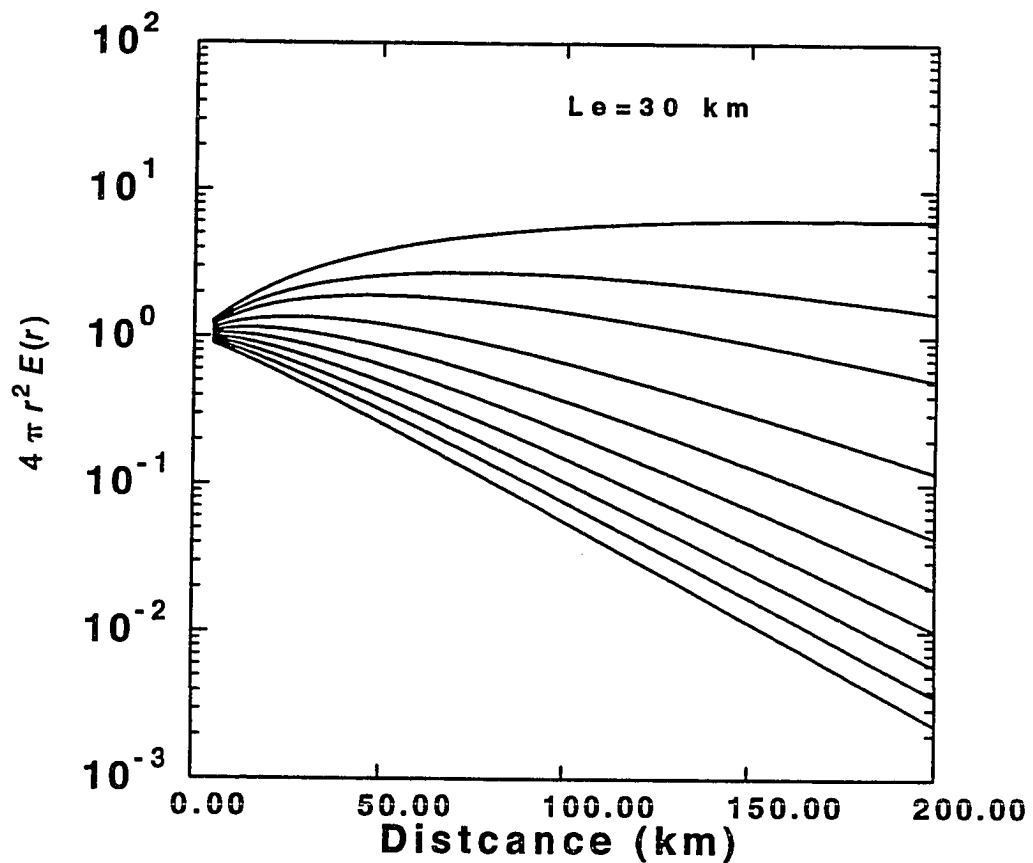


Figure 5.1 Theoretical prediction of the Radiative Transfer Energy. Vertical axis is $4 \pi r^2 E(r)$, where $E(r)$ is the total energy measured for a long time window of the seismogram. Seismic albedo B_0 varies from 0.99 to 0.2 for the curve on the top to for the curve on the bottom, respectively.

obtain values of B_o and L_e of the medium and thereby separate the scattering effect from the intrinsic absorption of the medium. The energy-distance curve in general is not a simple exponential curve as in the case of anelastic attenuation. Only in two cases can the curve be approximated by exponential decay forms. In the case of $B_o \gg 0.5$ and L_e large, the diffusive term is dominant in equation (5.5) and the apparent attenuation of energy versus distance is measured by

$$\gamma = d_o \eta_e = d_o (\eta_a + \eta_s). \quad (5.6)$$

The other case is when $B_o \ll 0.5$, i.e., $\eta_a \gg \eta_s$. In this case the absorption attenuation dominates and the apparent attenuation coefficient is

$$\gamma = \eta_a + \eta_s. \quad (5.7)$$

Hoshiha (1991) developed another method called multiple lapse time analysis to estimate the scattering and intrinsic Q^{-1} by considering energy for three consecutive time windows as a function of hypocentral distance. The shapes of the three energy curves as a function of source-receiver separation are simultaneously fit to Monte-Carlo simulation using homogeneously distributed scatterers in a full-space with uniform anelastic attenuation and isotropic multiple scattering for various B_o and L_e (Hoshiha, 1991).

5.3. Methods for measurement of energy density

In order to apply the Radiative Transfer Theory, we need to obtain energy as a function of hypocentral distance. This can be done in two ways.

Fourier energy

To normalize all records to a common source and site, the Fourier transform of the seismogram is taken from the onset of the S wave to $3 t_s$ after initial S arrival, where t_s is the travel time of S wave. This time window contains the main ground motion and a substantial part of the coda waves. The amplitude of waves after this window is generally smaller than the noise level prior to the onset of the P wave. The Fourier transform of this time window represents the entire, direct and scattered, S-wave energy. We call the squared of Fourier transform of the time window of the record the total S wave energy, $|F(f)|^2$. Our normalization to a common source and site is based on the empirically established fundamental separability of source, site, and path effects on the coda waves. Aki (1969) and Rautian and Khalturian (1978) have demonstrated that the coda amplitude decay rate measured after $2 t_s$ is independent of source, azimuth, site, and hypocentral distance. Our normalization then is accomplished by dividing $|F(f)|^2$ by the coda energy of a short window of coda at a fixed time reference, t_{ref} , such that

$$t_{\text{ref}} > 2 t_s.$$

Coda normalization is valid if the coda amplitude at a fixed lapse time is uniform for all the records after being corrected for the source and the site terms. Koyanagi *et al.* (1991); and Mayeda (1991) reported case studies of the coda amplitude in the island of Hawaii, in which the assumed uniformity of coda energy was not confirmed.

The procedure by which we calculated the coda amplitude in Chapter 4 offers a simple method to calculate corrected coda amplitudes and to test the uniformity of coda energy versus distance for different reference times of the coda waves. We want to find out how the coda energy is distributed in space at different frequencies. If the coda energy for a given lapse time decreases with hypocentral distance, the normalization of S wave energy using the coda energy will overestimate the energy. In Figure 5.2 we have plotted the averaged corrected coda amplitude for the four lapse times of 30 seconds, 40 seconds, 50 seconds, and 60 seconds against hypocentral distance. In each case the corrected coda amplitude was averaged in a time window of 5 seconds around the four lapse times for normalization. For any record, if $t_{\text{lapse}} < 2 T_s$, then that record was not used. The corrected amplitude values were averaged in a 10 kilometer window with 50 % overlapping. 50 sec and 60 sec lapse time windows are less stable and decrease substantially with

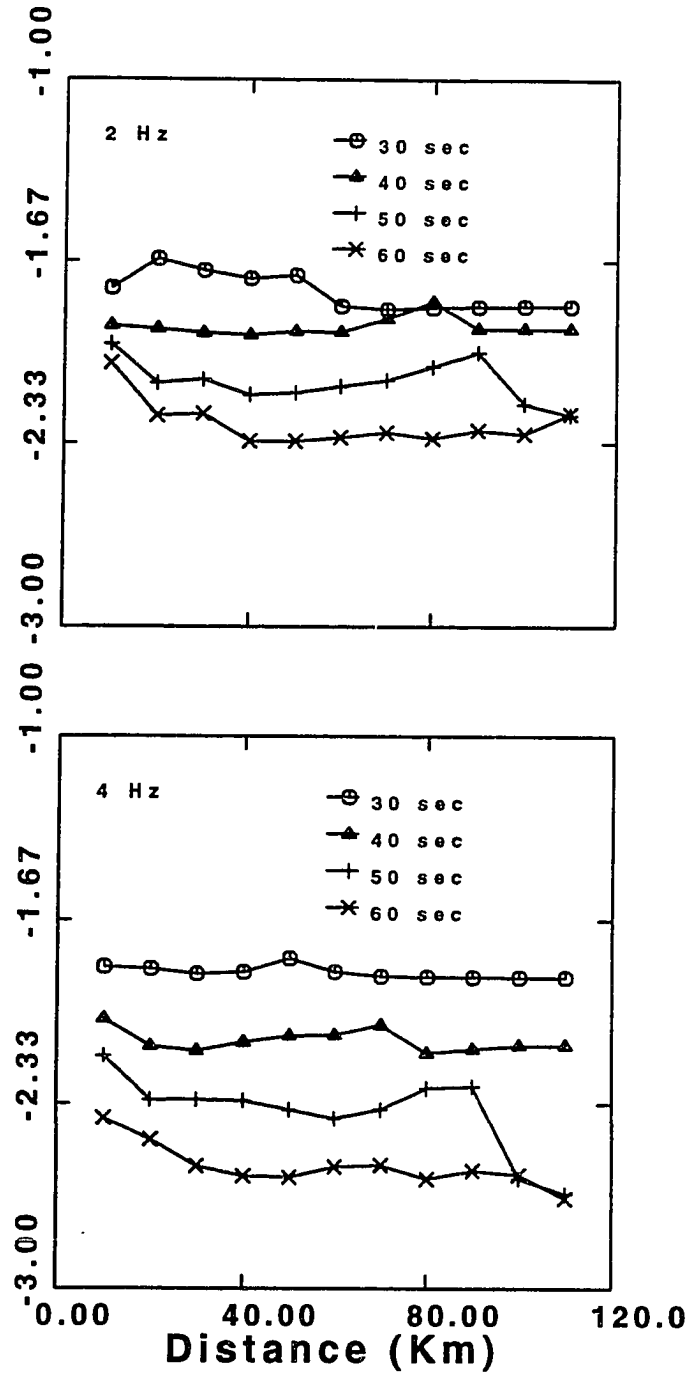


Figure 5.2a. Site and source corrected coda energy averaged over 10 km spacing for 2 Hz and 4 Hz at 30, 40, 50, and 60 seconds lapse time.

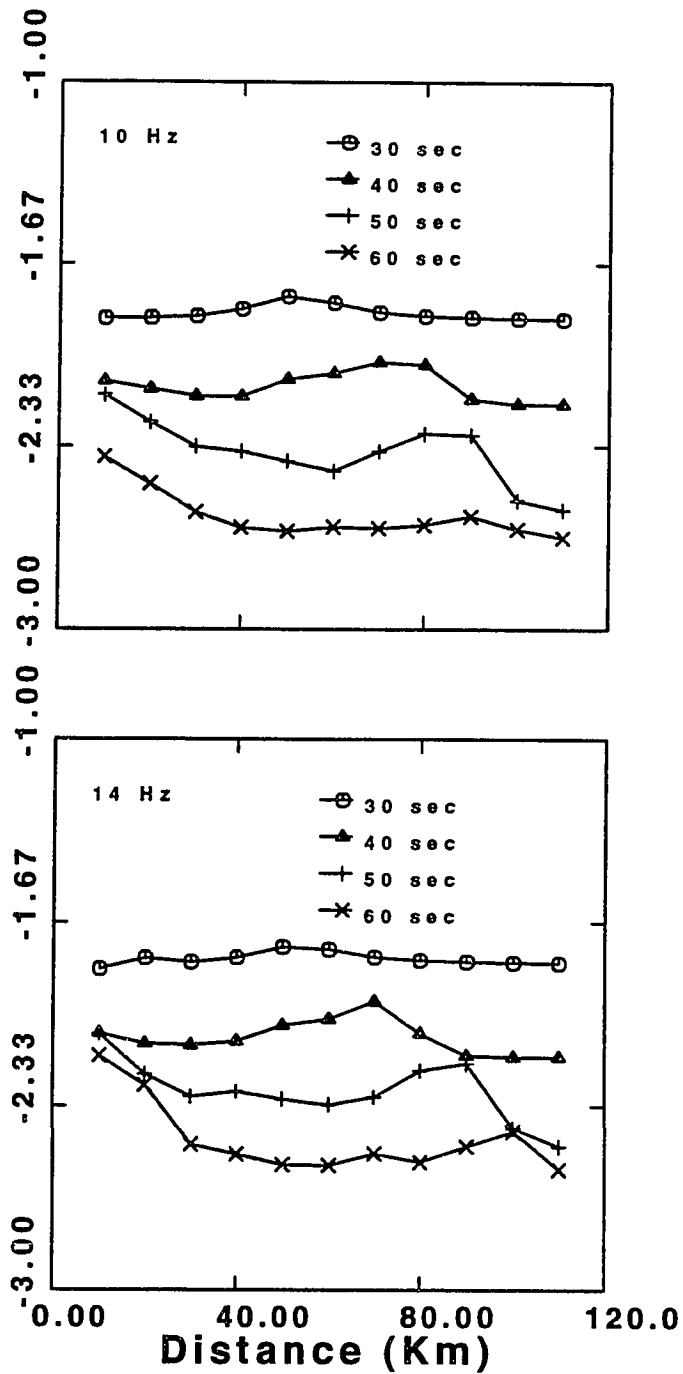


Figure 5.2b. Same as Figure 5.2a but for 10 Hz and 14 Hz. Notice the homogeneity of the coda energy for 30 second lapse time.

distance. The coda energy shows greater uniformity at the various frequencies for 30 sec and 40 sec lapse times. The reference coda time was chosen to be $t_c = 30$ seconds if $2 t_s < 30$. If $2 t_s > 30$ sec then, $t_c = 2 t_s$ was taken as the onset of the normalizing coda window and the power spectrum of the coda measured at $t = t_c$ was extrapolated to the reference time $t_{ref} = 30$ seconds by using

$$P(f, t_{ref}) = P(f, t_c) \left(\frac{t_c}{t_{ref}} \right) \exp \left[- \frac{\pi f}{Q_c} (t_{ref} - t_c) \right], \quad (5.8)$$

where Q_c is the coda Q calculated in Chapter 4.

Both S wave energy and the coda energy were corrected for noise by subtracting the power spectrum of the noise prior to the onset of the P-wave arrival from the power spectrum of S-wave and the coda waves. Finally, to normalize the S-wave energy of all the records to the same source and site, we divide the noise corrected power spectrum of the total S wave by the noise corrected power spectrum of the 5 second window of coda from the reference time, $|F(f)|^2 / |F_c(f)|^2$ to normalize all events to the same source strength and to remove the local site effect.

Results are presented in Figure 5.3. The normalized $4\pi r^2 E(r)$ are plotted as a function of hypocentral distance for frequencies 2,3,4,6,8,10, 12,14, and 16 Hz. For each frequency bands, a 50% overlapping window of 10 km was used to average all the power spectral ratios within that distance range. A non-linear least square

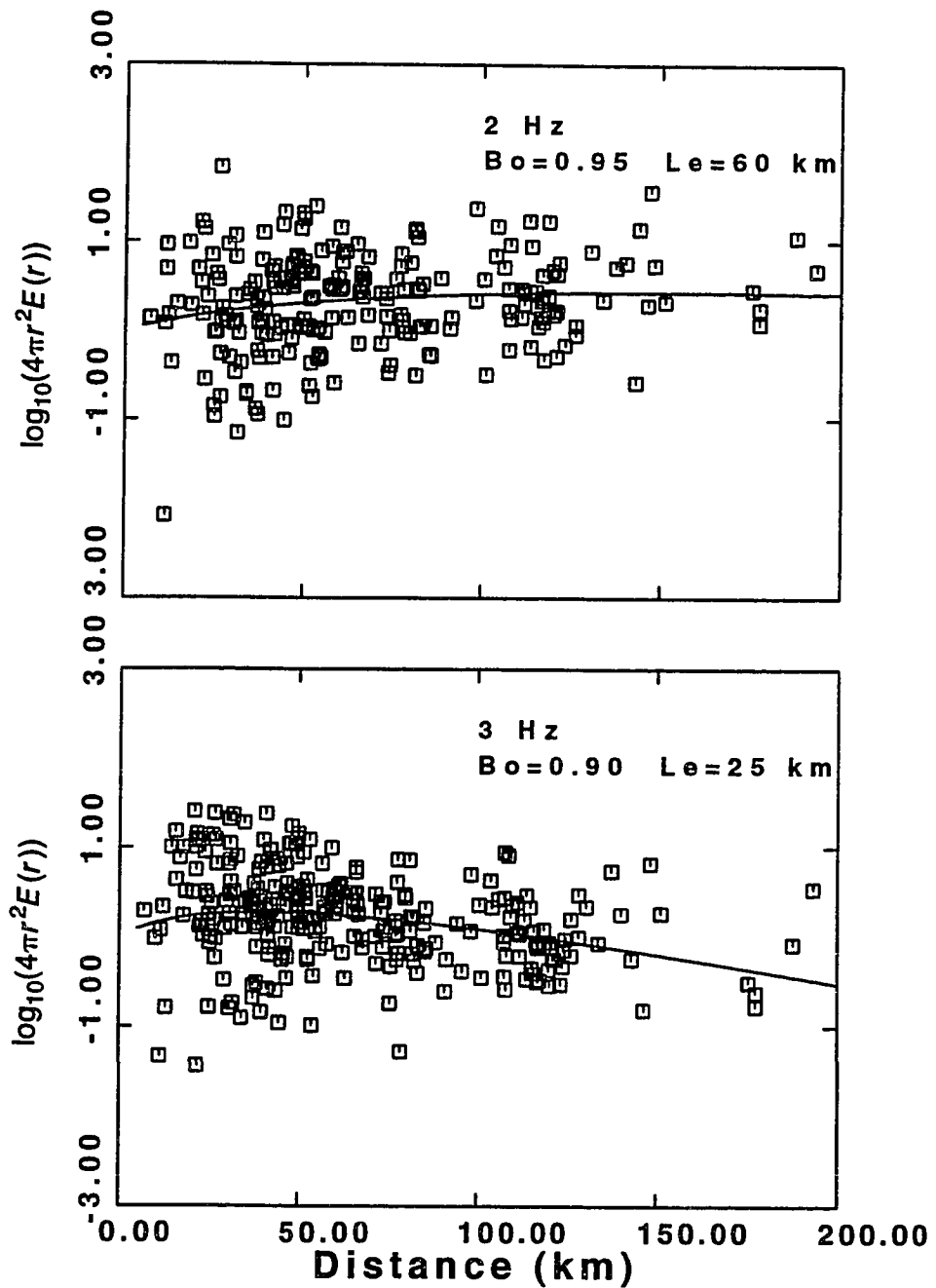


Figure 5.3a. Plot of normalized S-wave energy corrected for geometrical spreading for 2 Hz and 3 Hz. The theoretical curve from the Radiative Transfer Energy is shown by the solid line.

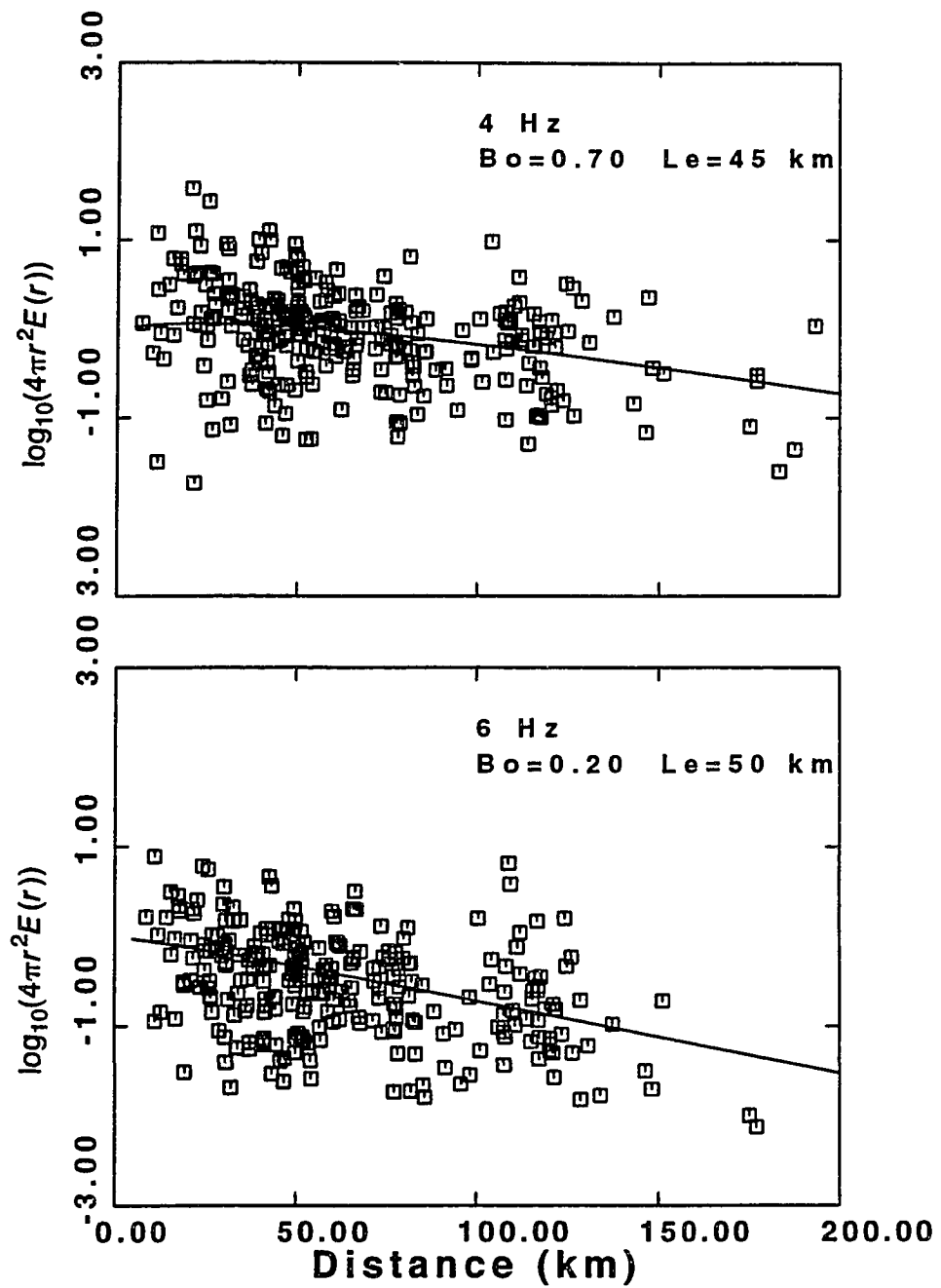


Figure 5.3b. Same as Figure 5.3a but for 4 Hz and 6 Hz.

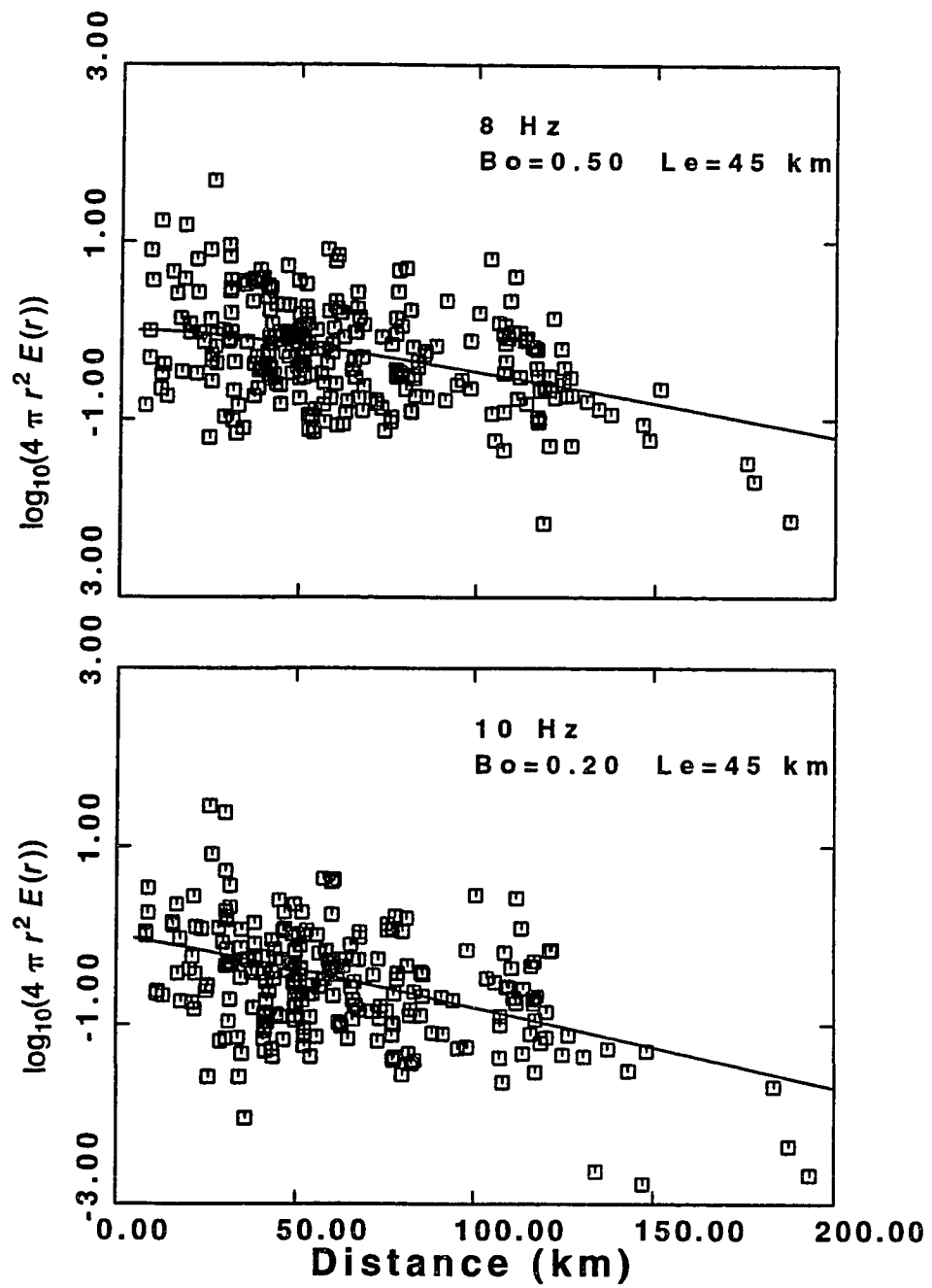


Figure 5.3c. Same as Figure 5.3a but for 8 Hz and 10 Hz.

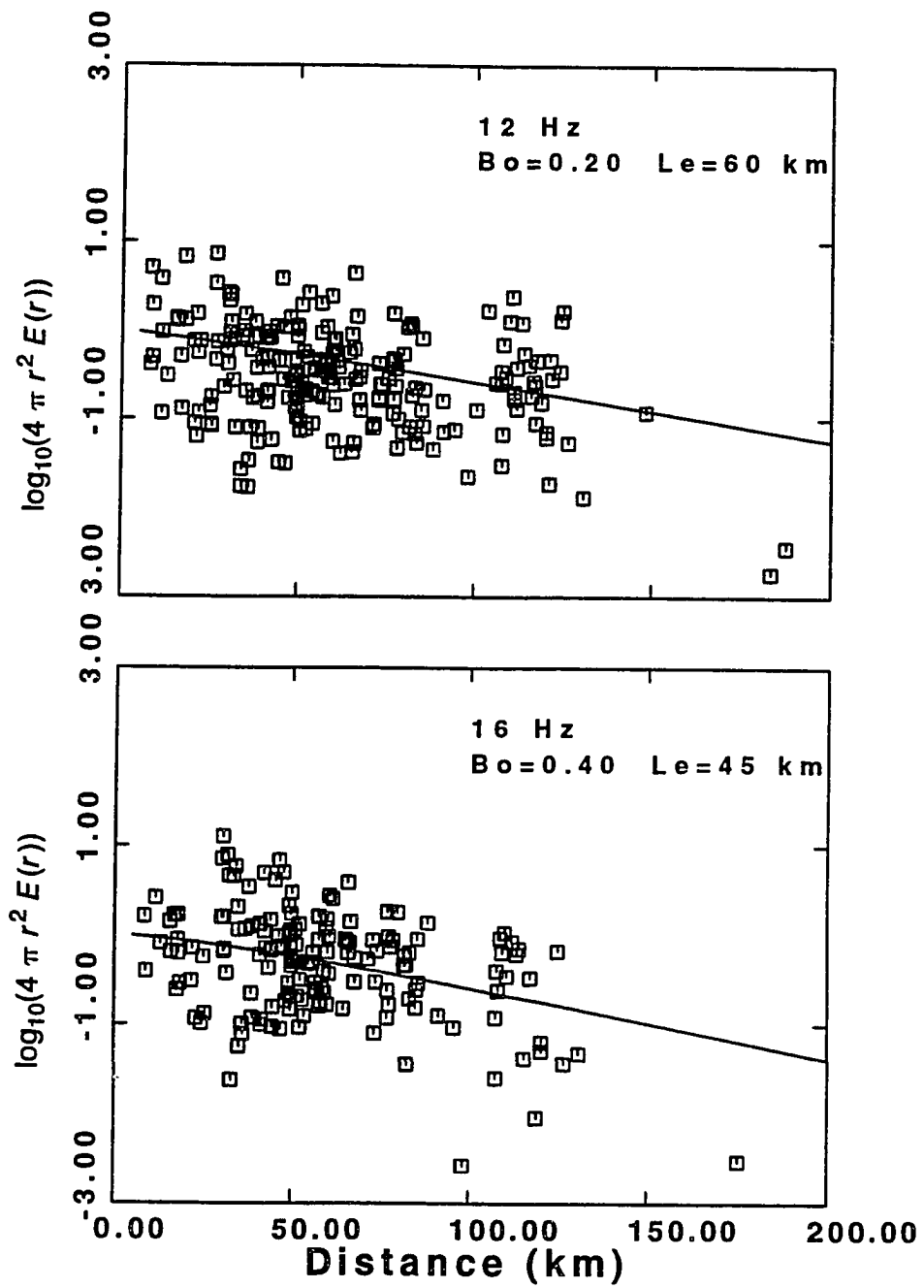


Figure 5.3d. Same as Figure 5.3a but for 12 Hz and 16 Hz.

procedure was used to find L_e and B_o in (5.5) to match the observed average power spectral ratios.

Energy as measured by response spectra

As shown in Appendix A, pseudo relative velocity spectrum, PSRV, and velocity response spectrum can be used to measure energy over the duration of ground motion. In particular $PSRV^2$ is the maximum strain energy stored in the spring-mass system of a simple damped harmonic oscillator placed at the receiver. Since an integration over the duration of ground motion is carried in this measure, the strain energy including scattered energy is measured.

To avoid any *a priori* assumption about geometrical spreading that might bias calculation of energy-distance curve, a non-parametric approach was determined to be more appropriate. For a fixed frequency f , the amplitude can be represented by

$$A_i(f,r) = S_i(f)D(f,r), \quad (5.9)$$

This procedure is very similar to the regression on PSRV data. The PSRV of each record is corrected for the site and the source, where site terms are the values calculated from the regression analysis of the main ground motion and are independent of geometrical spreading assumptions. This correction for the source and site is equivalent to the normalization by the coda method in the previous section. The source and site corrected PSRV is then corrected for

the geometrical spreading by multiplying by $4\pi r^2$. Figure 5.4 presents plots of $4\pi r^2 \text{PSRV}^2$ versus the hypocentral distances for frequency bands of 2,3,4,6,8,10,12,14, and 16 Hz. The averaged energy- distance curves are obtained by using 10 km windows with 10% overlap. Equation (5.5) is evaluated for values of B_o and L_e in the ranges 0.1-0.99 and 10-100 km respectively. For each pair of values of B_o and L_e , the sum of the mean squared difference between the average observed and the calculated values of corrected energy from equation (5.5) is obtained. The B_o and L_e of the medium are found by performing a non-linear least-squares inversion for each frequency band.

5.4 Measurements of scattering and anelastic attenuation

In this section we calculate Q^{-1} and its scattering and intrinsic components. The scattering and intrinsic coefficients are

$$\eta_s = \frac{B_o}{L_e}$$

and

$$\eta_e = \frac{1-B_o}{L_e} . \quad (5.10)$$

Then

$$Q_s^{-1} = k \eta_s$$

and

$$Q_i^{-1} = k \eta_i , \quad (5.11)$$

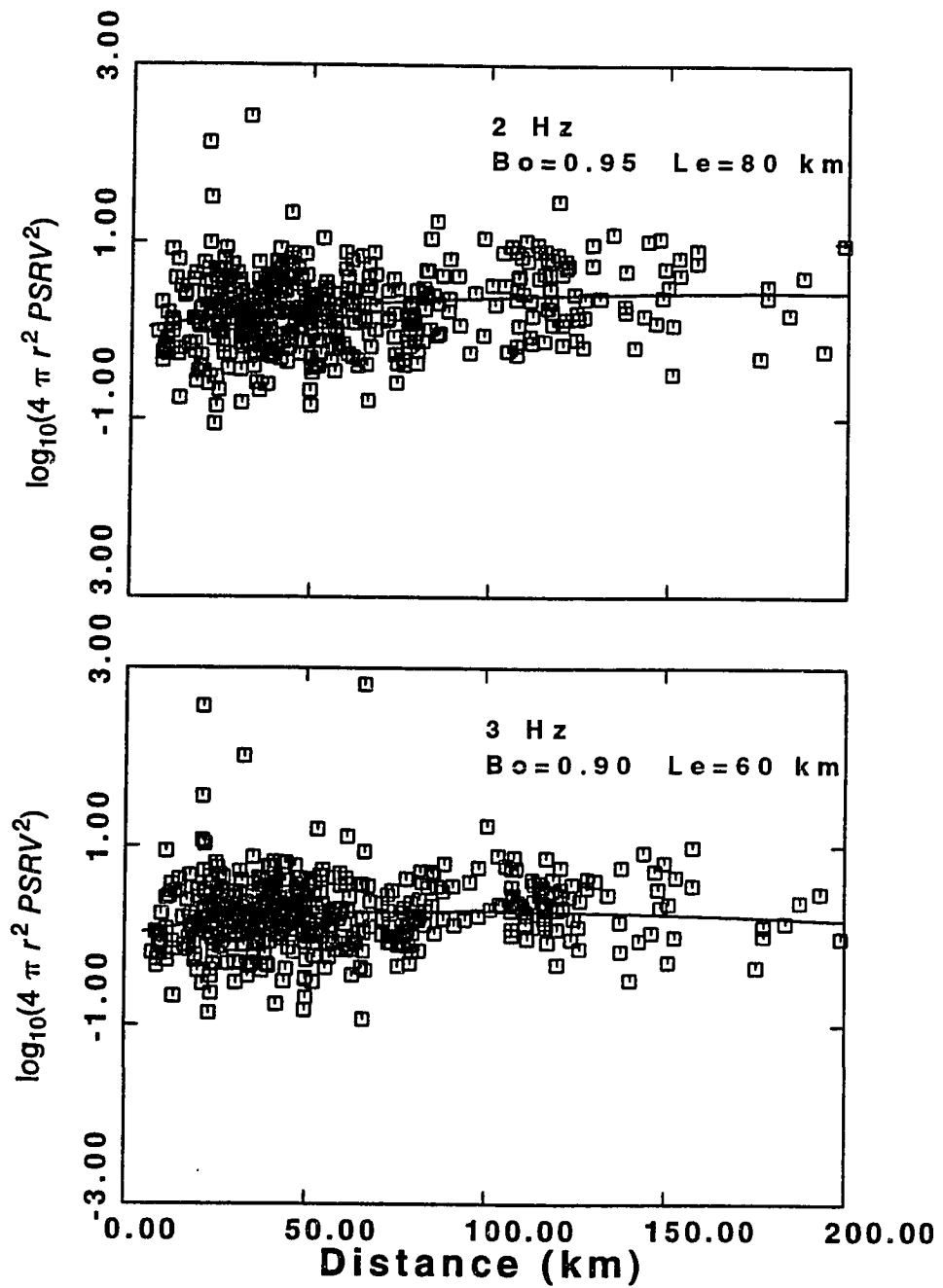


Figure 5.4a. Plot of $4\pi r^2 \text{PSRV}^2$ versus distance and the corresponding fit to the Radiative Transfer Energy for 2 Hz and 3 Hz. PSRV data are corrected for source and site effect terms. The corresponding model parameters are listed in Table 5.1.

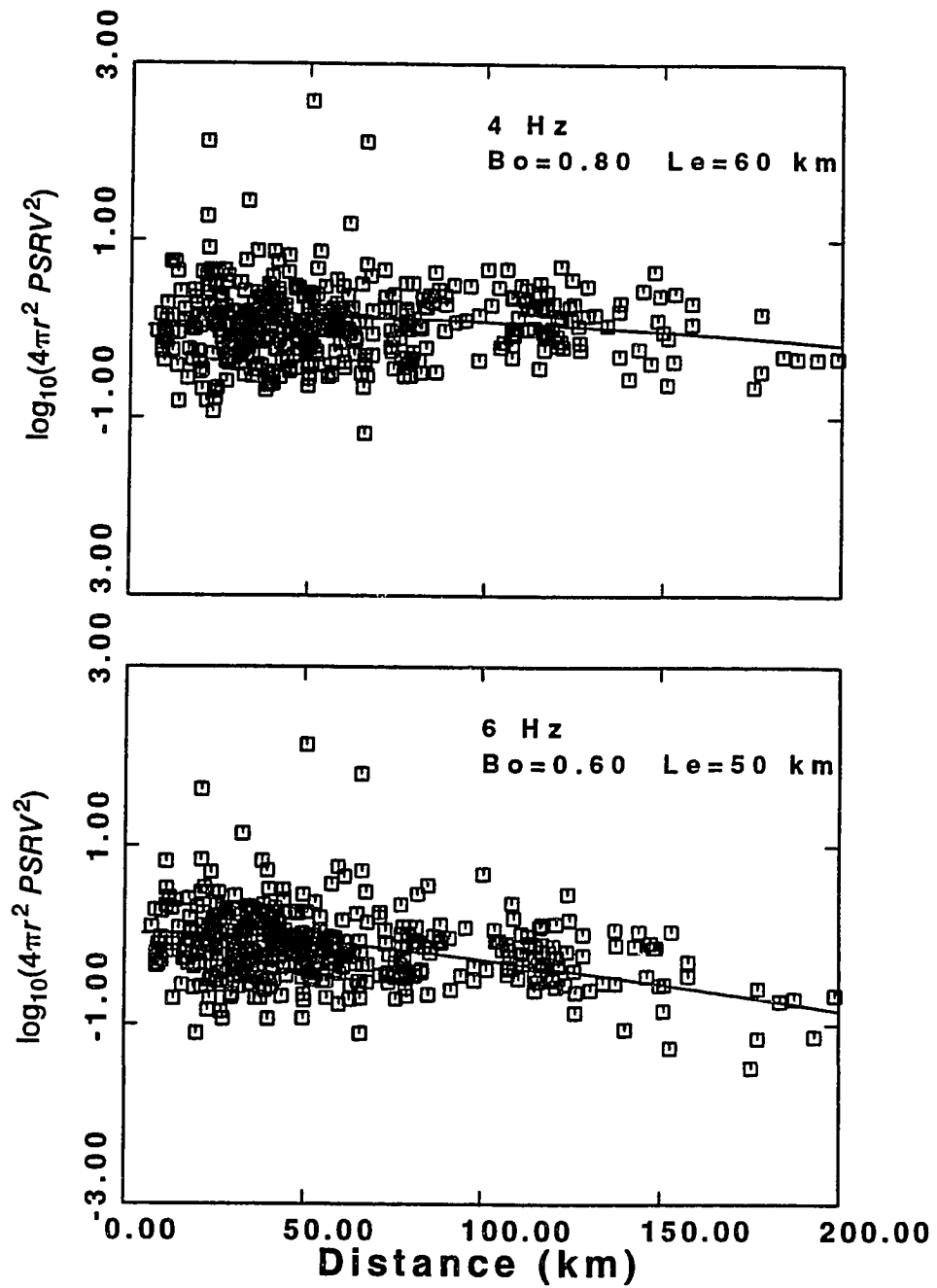


Figure 5.4b. Same as Figure 5.4a but for 4 Hz and 6 Hz.

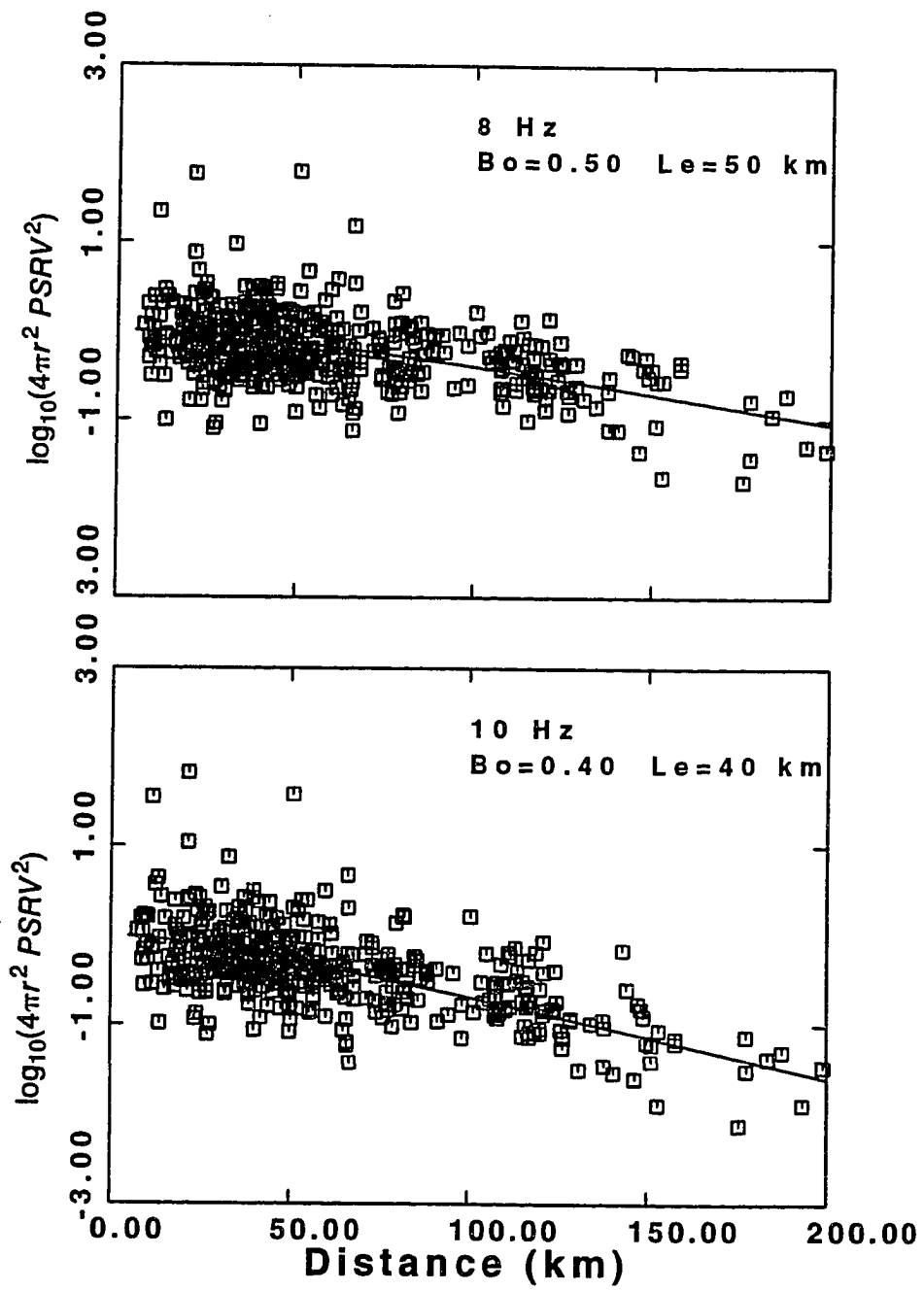


Figure 5.4c. Same as Figure 5.4a but for 8 Hz and 10 Hz.

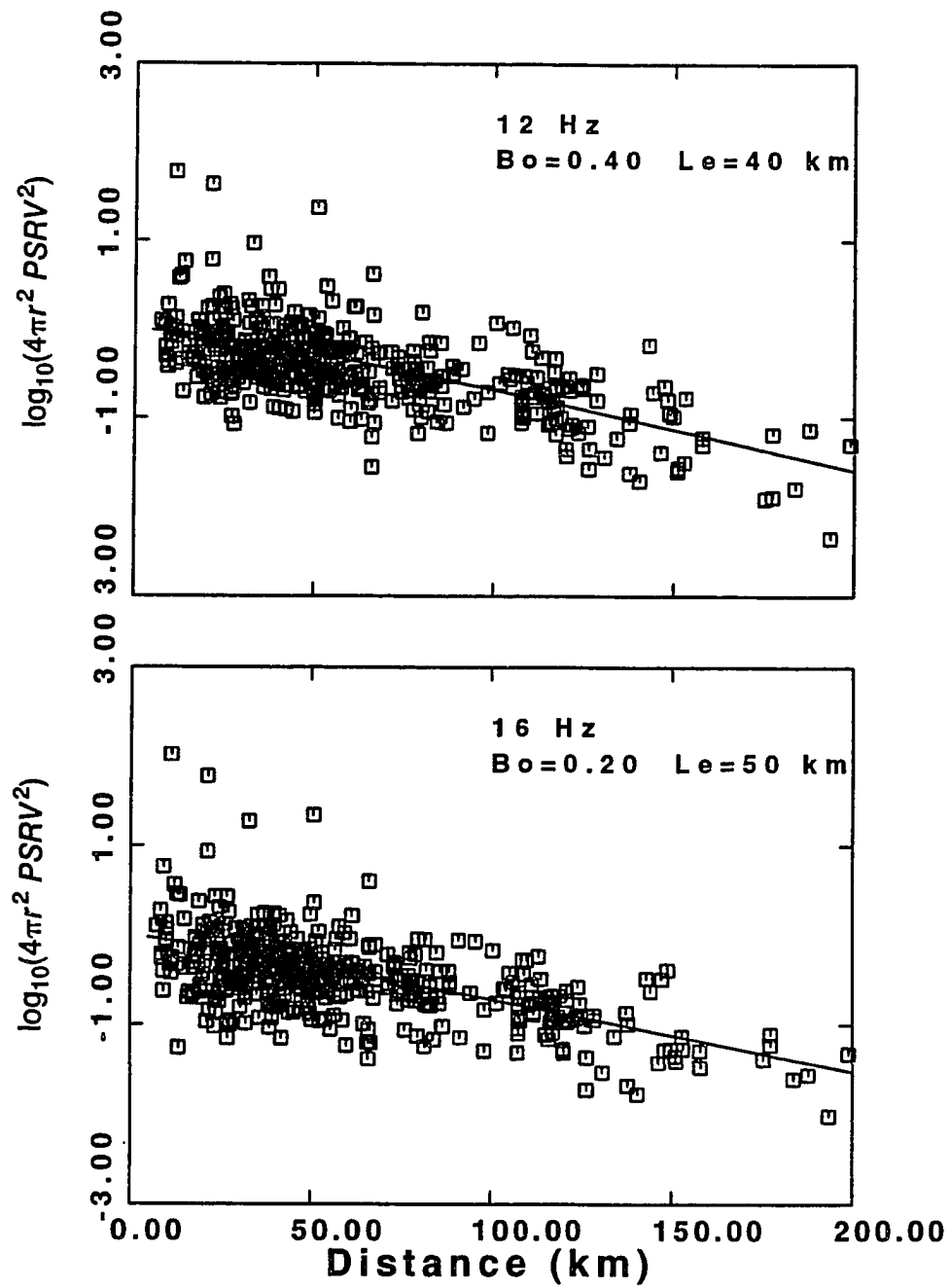


Figure 5.4d. Same as Figure 5.4a but for 12 Hz and 16 Hz.

where $k = \frac{v}{2\pi f}$ is the wave number of wave traveling with velocity v . The two sets of values of (B_o, L_e) are in general agreement at low frequencies. There are some differences at higher frequencies, mainly due lack of enough data points at distances beyond 100 km for the Fourier energy method. This is mainly due to the noise criterion which we imposed. There is also the problem of non-uniform coda energy versus distance. Many studies suggest a decrease in Q_c^{-1} with lapse time (Roeker *et al.* 1982). A lapse-time dependent Q_c^{-1} can explain this non-uniformity. The selection of the time window for estimating energy is very important (Hoshiba, 1991). In energy estimation using PSRV, we integrate over the entire duration of seismogram which is always larger than the Fourier spectrum of the seismogram. The subsequent normalization of PSRV based on regression analysis indiscriminately removes the source and site effects for the distance range 0-200 km. The coda normalization, on the other hand, is less reliable for distances greater than 100 km. We use B_o and L_e calculated based on the energy estimates of PSRV to determine the attenuation parameters.

Q_s and Q_i are calculated using (5.11). The results are shown in Table 5.1 Also shown are Q_c , Q_t , and Q_{psrv} , where $Q_t^{-1} = Q_i^{-1} + Q_s^{-1}$ and Q_{psrv} is the apparent Q calculated from the trilinear regression PSRV data from Table 3.1.

TABLE 5.1**Intrinsic and scattering Q parameters of SGB**

Freq (Hz)	B_o	L (km)	Q_i	Q_s	Q_t	Q_{psrv}	Q_c
2	0.95	80	6280	331	314	492	293
3	0.9	60	3533	393	354	784	317
4	0.8	60	2355	589	471	836	392
6	0.6	50	1472	961	581	790	569
8	0.5	50	1570	1570	785	868	753
10	0.4	40	1308	1963	785	824	962
12	0.4	40	1570	2355	942	1024	1214
14	0.2	45	1547	6189	1238	1243	1518
16	0.2	50	1964	7850	1571	1434	1867

According to the results in Table 5.1, Q_s is closer to Q_c for frequencies less than 6 Hz. For $12 > f > 6$ Hz $Q_t \approx Q_c$. For $f > 12$ Hz $Q_t \approx Q_i$. This is in agreement with results obtained by Mayeda *et al.* 1992), Mayada *et al.* (1991), and McSweeney *et al.* (1991). Q_{psrv} is very sensitive to the geometrical spreading model, but in general the observed apparent attenuation of the S wave is lower than that of the coda waves and apparently is dominated more by intrinsic attenuation than the coda waves. A frequency-independent Q of S waves $Q_s = 1600$ calculated for S phases in Chapter 3 is very close to the calculated values of Q_i .

5.5 Discussion and conclusions

Energy plots at 2 and 3 Hz increase with hypocentral distance, roughly to 100 km. This can be seen from both methods. The increase in energy with distance could be due to surface wave energy which becomes important at distances around five times the source depth. In our case of depths usually less than 10 km, this will be about 50 Km. The surface wave energy applies only to long period estimates because high frequency surface waves are not generated unless scattered by topography or by shallow heterogeneity. Another explanation for the increase of energy could be anisotropic scattering due to strong layering, such as volcanic flows. Finally at large distances of about 100 km, depth sampling becomes important. Any depth-dependent scattering and anelastic Q^{-1} in the

lithosphere, will deviate from our idealized model of homogeneous scattering and uniform anelastic attenuation. Assumption of homogeneous scattering for high frequencies is an acceptable approximation but at lower frequencies such homogeneity may not be acceptable.

Figure 5.5 shows Q_s^{-1} , Q_i^{-1} , and Q_t^{-1} for the Southern Great Basin. The strong frequency-dependent Q_s^{-1} is consistent with theoretical results which predict decreasing Q_s^{-1} with frequencies greater than a critical value corresponding to the dominant scale length of the heterogeneity of the medium (Wu, 1982; Sato, 1982; Frankel and Clayton; 1986). Q_s^{-1} decreases as f^{-2} whereas Q_i^{-1} is relatively frequency independent. Our results are consistent with the results obtained by Mayeda *et al.* (1992) in Central California, Long Valley California , and Hawaii.

Most theoretical studies predict that the coda Q values are measurements of anelastic Q of the medium (Frankel and Wenerberg, 1987; Wu, 1985). Other Q measurements suggest phenomenological coincidence between Q_c^{-1} and Q_β^{-1} (e.g. Aki, 1980). Frankel and Wenerberg (1987) developed a model of coda based on elastic energy conservation during scattering. This energy flux model (EFM) predicts that the coda decay is a measurement of the intrinsic attenuation and is insensitive to the scattering Q. According to this model the coda amplitude for body wave

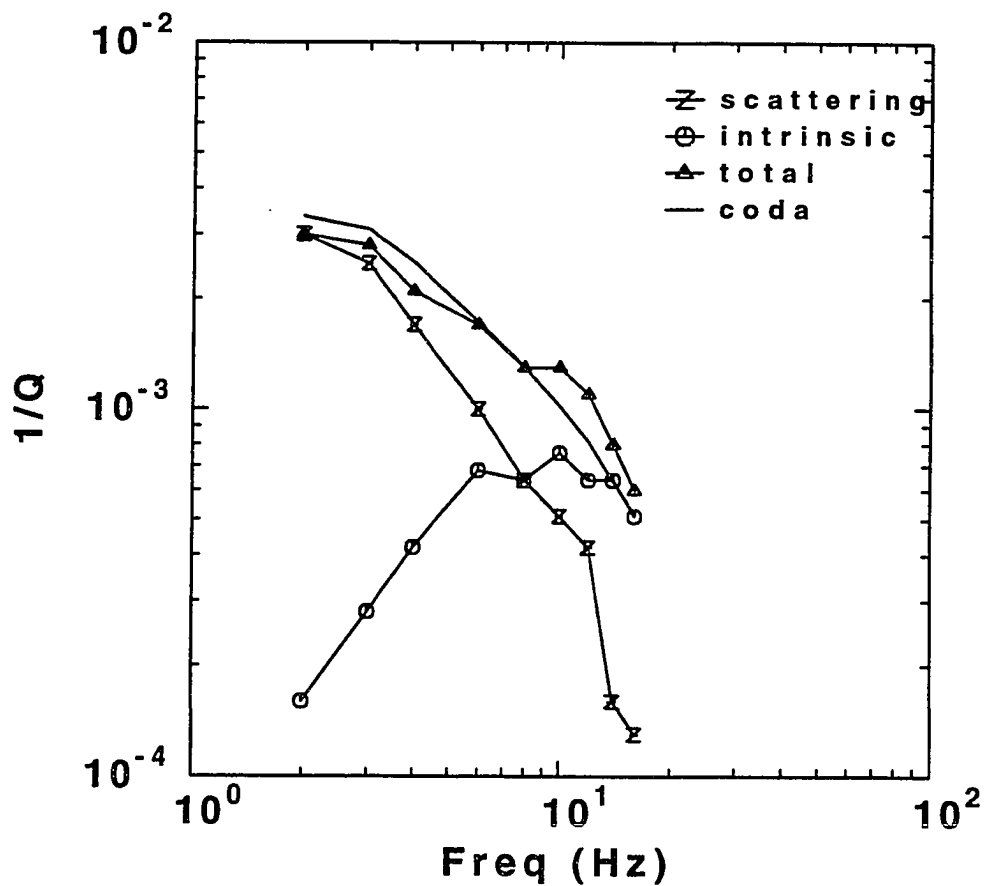


Figure 5.5. Values of Q_s^{-1} , Q_i^{-1} , and Q_t^{-1} predicted from the Radiative Transfer Energy for the Southern Great Basin are plotted versus frequency. Also shown is Q_c^{-1} . Notice that Q_c^{-1} and Q_t^{-1} are very close from 2 to 16 Hz.

scattering is proportional to $t^{-3/2} e^{-\omega t/2Q_s} (1 - e^{-\omega t/Q_s})^{1/2}$. The coda decay is no longer exponentially related to the scattering Q and, therefore, coda is not very sensitive to Q_s . The key measurement in this model, is the relative decay of the coda and the direct S wave with respect to lapse time at high frequency and low frequency. One measurement is to compare the absolute decay of the coda envelope to that of the S wave. If the coda and the S wave decay with the same rate at a given frequency this is indicative of the importance of anelastic attenuation for that frequency. If scattering attenuation was important, it would cause the S wave to decay faster than the coda waves (Frankel, 1991).

We calculated the coda envelope of all the records normalized to a common source. The coda envelopes of frequencies of 2 to 16 Hz were then averaged for each lapse time. To compare the decay of the coda with that of the S wave, we used S wave amplitudes normalized to common source calculated in Chapter 4. Both amplitudes are plotted versus time. For the S wave this time represents the travel time, corresponding to a 3.2 km/s travel time, and for the coda time is the lapse time measured from the origin time. Figure 5.6 compares decay of amplitude for the coda and the S waves versus time for frequencies 2 Hz and 16 Hz. At 2 Hz the coda and S wave decay with equal rate out to 20 seconds. The coda decay continues with the same rate but the S wave decay increases

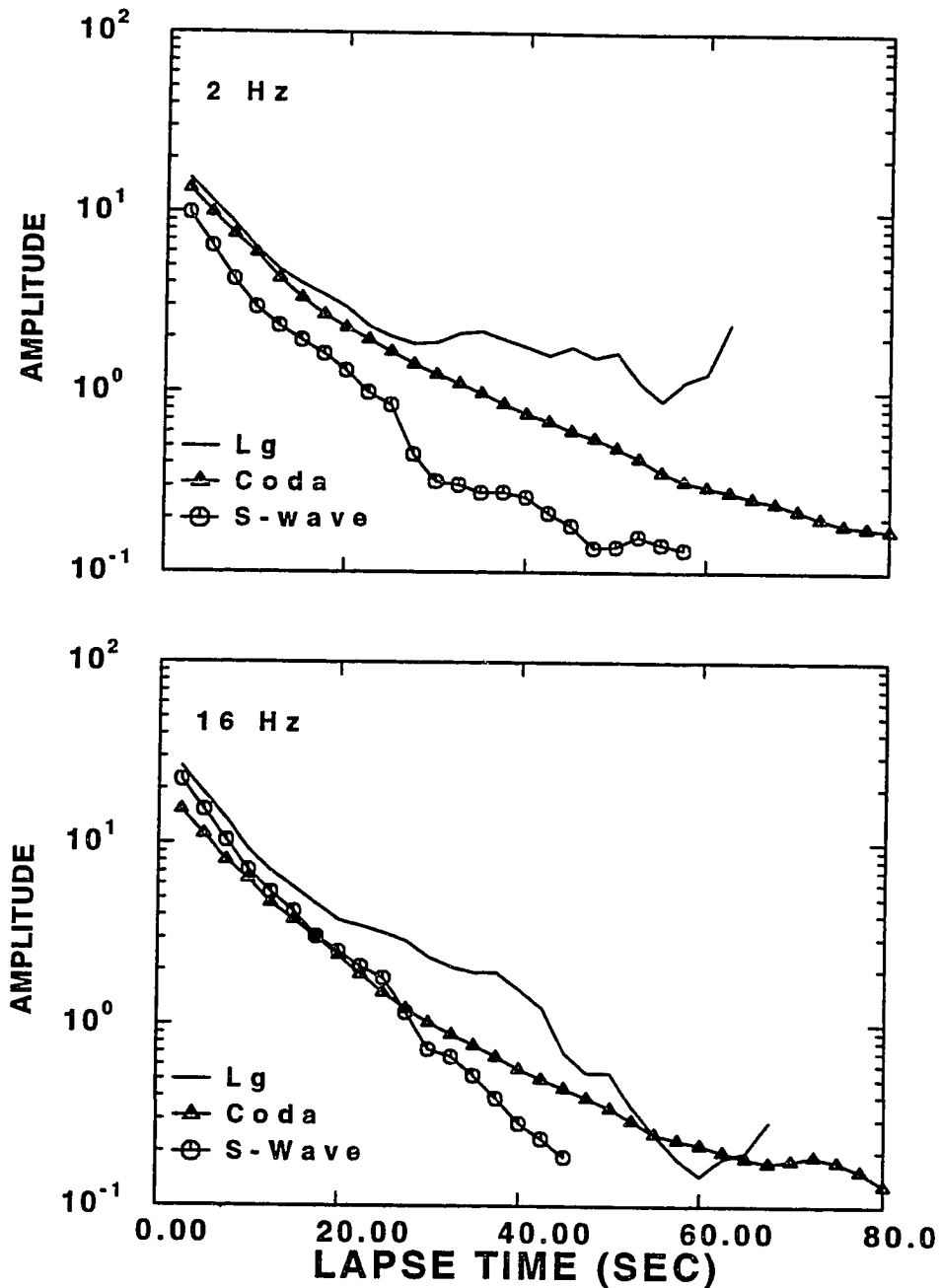


Figure 5.6. Average coda envelopes, Lg amplitude, and first S waves at 2 Hz and 16 Hz. Lg and S-wave amplitudes are coda-normalized. For coda envelopes, time is lapse time in seismogram after origin time. For Lg and S wave amplitudes, time is travel time.

considerably. According to the *Energy Flux Model* this implies the dominance of intrinsic attenuation over scattering attenuation for this frequency. At 16 Hz the decay of the coda and S-wave are closer to each other. An alternative explanation which is more consistent with our observations is that early S-wave phases are scattered strongly and some of the energy is transferred into the later part of the S wave or Lg phase. The decay of the coda resembles that of the early S wave because both are scattered similarly. The emergence of the Moho reflected phases cannot explain all of our observations.

Based on these energy considerations we make the following conclusions.

1. Scattering attenuation is the dominant mechanism for frequencies less than 6 Hz.
2. The coda attenuation is dominated by scattering for frequencies less than 6 Hz.
3. The coda and S wave attenuation for frequencies greater than 6 Hz is best represented by $Q_c^{-1} = Q_i^{-1} + Q_s^{-1}$.
4. The temporal measurements of attenuation using coda phase and spatial attenuation of the S wave, are not necessarily equal and their phenomenological coincidence as reported by some investigators is not supported here.

CHAPTER 6

LOCAL SITE EFFECTS

6.1 Introduction

The site amplification has a great influence on ground motion by modifying the shape of the spectrum. We are interested in obtaining information about source and medium by using small earthquakes in the frequency range from 1 to 20 Hz. Site effects can influence these observations. Hanks (1982) believed that the f_{\max} of acceleration spectra at distances less than 100 km is controlled by site effects. Frankel (1982) observed that the corner frequencies of P waves and S waves are controlled in some degree by station affects. Since site amplification can effect moment calculation in the frequency range from 1 to 20 Hz, source studies of microearthquakes will be incomplete without considering these effects (Aki, 1969).

In this study, we notice significant differences among amplitudes of an earthquake recorded at stations that are very similar in distance although the geological description of each site may differ slightly in their immediate vicinity. As an example, in Figure 6.1, we show SV calculated for the two stations YMT1 and YMT5 in Yucca Mountain for Event 39 in Table 6.1. These stations are within 10 km from each other. The hypocentral distances for these three

recordings are 117.2 and 110.6 km respectively. We notice that the SV of YMT1 is about 10 times larger than of YMT5 in the 1 - 5 Hz frequency band. Radiation pattern and angle of emergence for waves arriving at these station sites cannot account for the difference of observed amplitudes.

Earlier studies on coda waves of local earthquakes showed that the coda excitation depends on the local geology of the station (Aki and Chouet, 1975). Aki (1969) observed that the site amplification can be 5-8 times larger on sediments than on granite. Phillips and Aki (1986) determined the site amplification of coda waves from local earthquakes in central California. They found that variations in the impedance are responsible for most site response differences at low frequencies. Amplification generally decreases with age for sedimentary units and is lowest for granite units. They also argued that changes in near-site attenuation are responsible for most variations of site amplification at high frequencies. The highest amplification is correlated with the lowest near-site attenuation, which is observed in granitic units. Phillips and Aki, (1986) processed U.S. Geological Survey Central California Network data and showed that amplitudes can vary up to a factor of 20 for different sites. His maps of site factors for 1.5 to 3.0 Hz correlate with surface geology. The pattern changes as the frequency increases. At 12 Hz the granite of the Gabilan range shows high amplification.

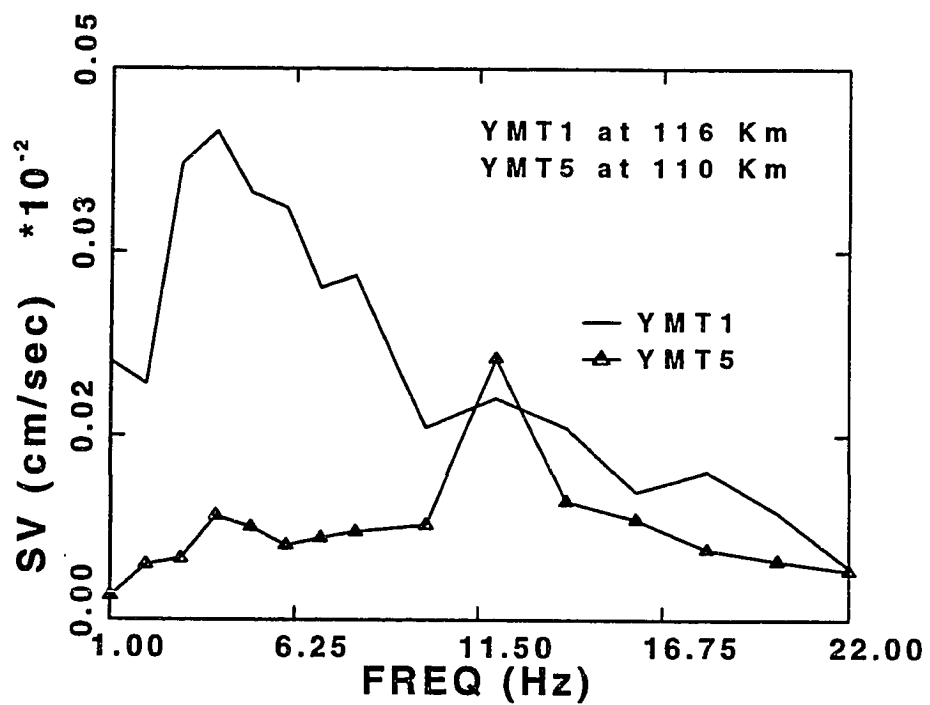


Figure 6.1. SV for YMT1 and YMT5 for the earthquake 39 of Table 1.1. Notice that SV at YMT1 is amplified ten times more than at YMT5 in the frequency range of 1-8 Hz.

Anderson and Hough (1984) estimated attenuation from source to receiver by modeling the spectral decay of the acceleration spectra by a term $e^{-\pi\kappa f}$. The spectral decay variable, κ , associated with attenuation, is parameterized as

$$\kappa = \kappa_1 + \kappa_0 \quad (6.1)$$

the sum of a distance dependent term, $\kappa_1(r)$, and a site term, κ_0 . Humphrey and Anderson (1992) found κ_0 for 30 stations located in Guerrero, Mexico on rock outcrops. They did not find reliable correlations between κ_0 and sample density, near surface shear velocity, or any other geologic characteristics of the individual sites. They calculated the average of differences between observed spectra to model event spectra corrected for and geometrical spreading. The frequency dependent site functions thus defined show significant amplification and deamplification effects for the hard-rock sites. In a recent study, Mayeda (1991) demonstrated that sites with similar geology do not necessarily produce similar ground amplification behavior, especially in complex volcanic regions. They found that subsurface structure and thickness of the surficial layer may have profound effects on the amplification.

If the coda waves are backscattered S waves from heterogeneities distributed uniformly in the lithosphere (Aki 1980b, 1981), we will expect the observed site effect on local earthquake coda waves for the frequency range 1 to 30 Hz to be very similar to the

site effects on S waves averaged over all directions (Tsujiura, 1978). Tsujiura (1978) and Tucker and King (1984) further concluded that using the coda waves results in more stable calculations of site amplification. Since coda waves are composed of many back-scattered shear waves from heterogeneities that have filled the volume between the source and the receiver, the propagation effects are averaged throughout the medium which means the separation of the coda amplitude into source-path-receiver operators is guaranteed.

Our goal here is to examine different methods for measuring the low-strain site-effect, to evaluate their stability, relative ease of computation, and agreement or disagreement among them. In this study we will investigate and calculate site response transfer functions using three methods.

1. Our first approach uses the coda amplitude to separate and calculate the average coda Q and geometrical spreading of the coda. Site terms are calculated by removing the whole path Q and source terms from the coda amplitude data.
2. In the second method, station terms are calculated from our general regression model of the ground motion using PSRV of records of local earthquakes. In this approach we do not impose any constraint on the high-frequency decay behavior of the source spectra, and therefore attenuation properties that

are common to all stations may map into the source term. We impose the constraint that the mean overall station frequency-dependent site response for each frequency is equal to one.

3. The final approach to evaluate the site amplification follows Humphrey and Anderson (1992) by modeling the observed spectrum as the product of source, Q operator, site attenuation operator (Anderson and Hough, 1984), and instrument response functions. The difference between observed spectrum and the modeled frequency amplitude is interpreted as the site amplification. We will apply a modified method in which the source parameters and the site attenuation will be calculated through an inversion. Averaged spectral residuals are calculated and compared with the site terms calculated from the direct inversion. The advantage of this approach is that it incorporates site attenuation as one of the active direct parameters of spectral amplitudes. The weak point of this approach is that it is based on an *a priori* assumption about the source.

6.2 Coda site amplification

As demonstrated, the logarithm of the amplitude of the coda waves at time t after the origin time for frequency f can be expressed as:

$$\ln A(f, t) = d_{ijk} = z_i + s_j + c(f, t_k) \quad (6.2)$$

where the z_i are the site terms, s_j the source terms, and c is the

coda shape function independent of source-receiver location. Indices i, j , and k denote the site, source, and lapse time respectively. To calculate $A(f, t)$ we bandpass the entire seismogram of interest with a narrow-band Butterworth filter. We calculate the root mean squared signal in a 5 second moving window beginning at the lapse time of twice the shear wave travel.

Since the coda energy is due to backscattered shear waves from heterogeneities distributed more or less uniformly throughout the volume between the source and the receiver, the coda shape $c(f, t_k)$, which is the path term, contains averaged regional properties and is common to all recordings of a given event. Thus if we take an average of d_{ijk} over all the sites at which the measurement is made while holding source and lapse time indices, j , and k , fixed and subtract it from d_{ijk} we can write

$$d_{ijk} - \bar{d}_{jk} = z_i - \bar{z} \quad (6.4)$$

where \bar{z} is the average z_i over all the stations recorded event j at time t_k . Following Su *et al.* (1992), we write $z_i = \sum_{m=1}^{\text{all}} \delta_{im} z_m$ and

$$\bar{z} = \frac{\sum_m I_m z_m}{N_{jk}} \quad \text{where } \delta_{im} \text{ is the Kroneker delta, } N_{jk} \text{ is the total}$$

number of usable stations for fixed indices j , and k and $I_m = 1$ if station m is used, otherwise $I_m = 0$. Therefore we solve the matrix equation

$$d_{ijk} - \bar{d}_{jk} = \sum_m (\delta_{im} - I_m / N_{jk}) z_m. \quad (6.5)$$

Writing equation (6.4) in matrix form:

$$\mathbf{M} \mathbf{z} = \mathbf{d} \quad (6.5)$$

where \mathbf{z} is the vector which contains the site amplifications. A stochastic inversion method similar to the method discussed in Chapter 3 is applied here.

Results

We show the site amplification terms for the SGB network with solid lines in Figure 6.2, along with the results from the other two methods. One of the characteristics of the site terms calculated from the coda wave analysis compared to the other methods is that they have smoother variation with frequency and any change with frequency is more gradual than for the other methods. The coda site terms are usually higher for the sites located on young volcanic rocks at lower frequencies of 1 to 8 Hz and gradually the the logarithm of amplifications becomes negative as frequency increases. For the same sites the amplifications are even greater for the sites with horizontal instruments. Older carbonate rocks and, in general, older bed rock sites have smaller amplification terms at lower frequencies with an increasing trend for frequencies greater than 10 Hz.

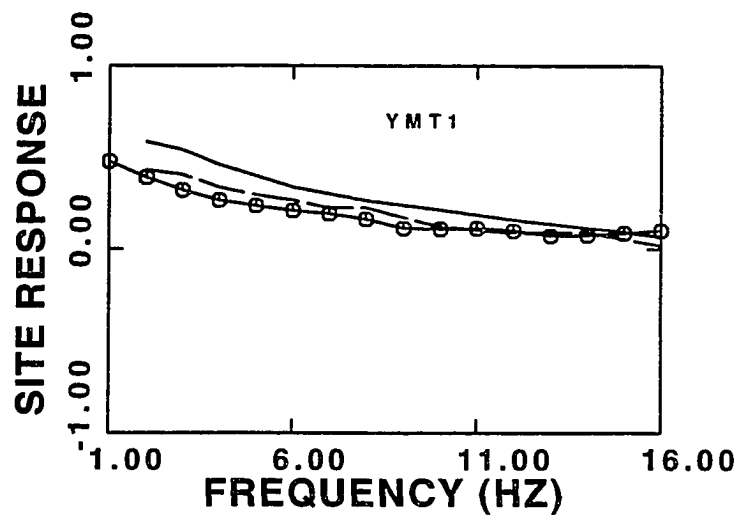


Figure 6.2a. The residuals of the observed spectrum and the modeled spectrum averaged for all events recorded at YMT1 are shown here by the line denoted by small circles. Site amplification terms calculated from the regression of SV data are shown by long broken line. The solid line represents the site amplification terms using the coda method. The vertical scale is $\log_{10}(\text{amplification})$.

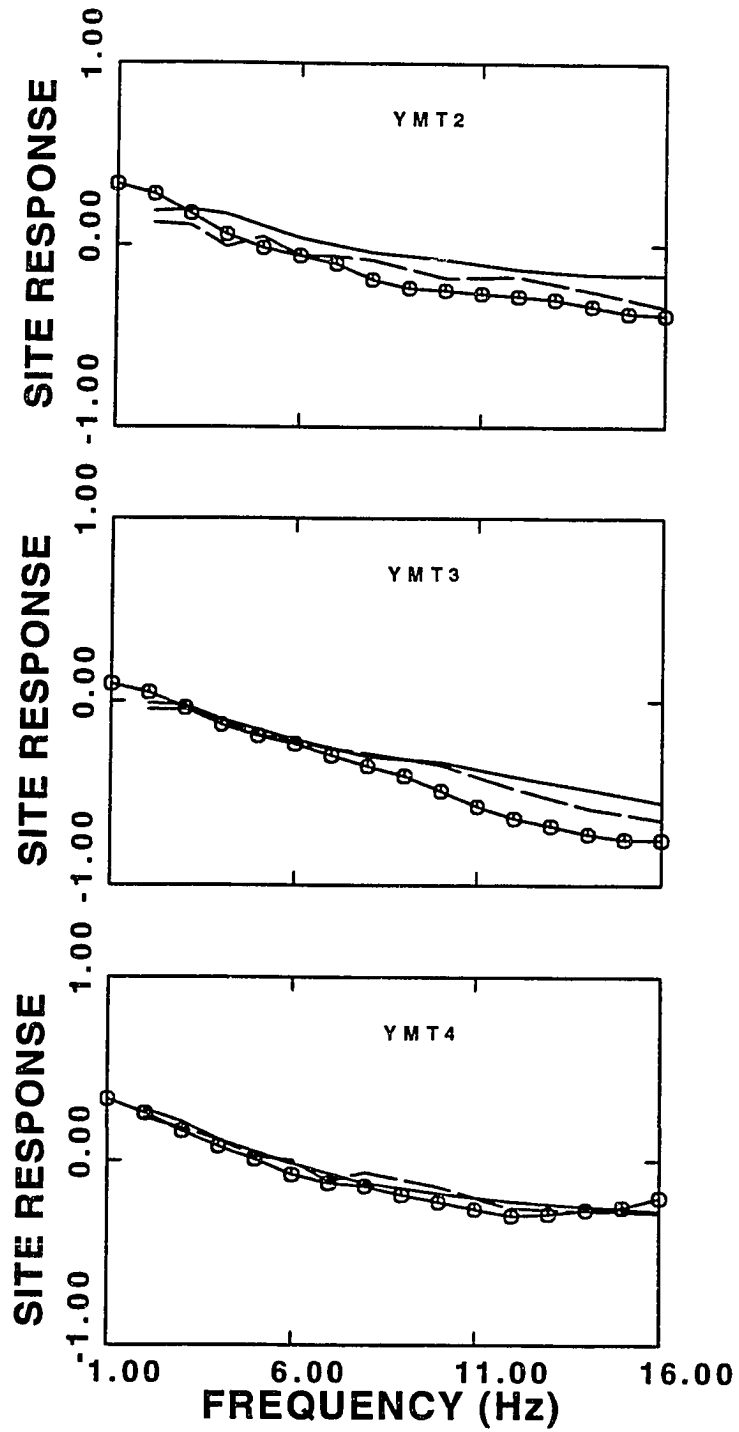


Figure 6.2b. Same as Figure 6.2a but for stations YMT2, YMT3, and YMT4.

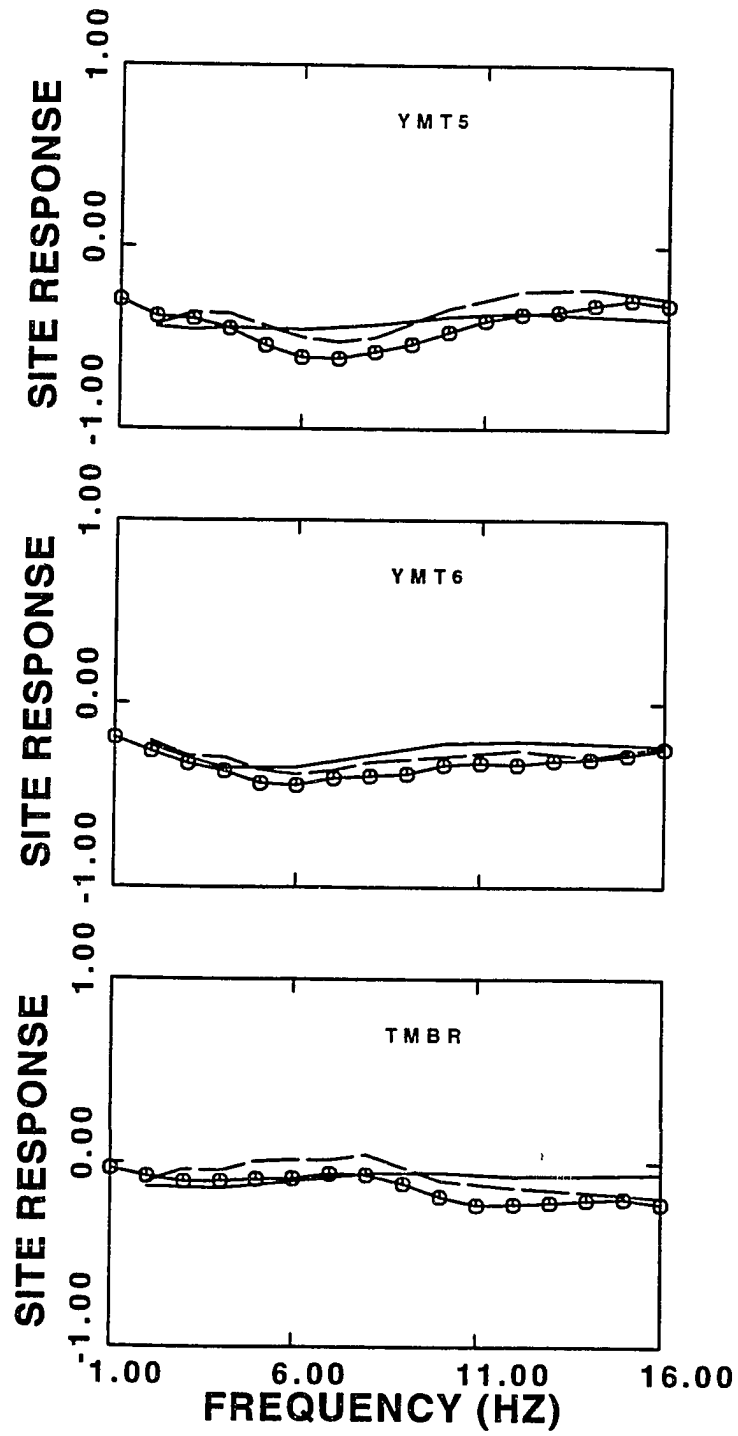


Figure 6.2c. Same as Figure 6.2a but for stations YMT5, YMT6, and TMBR.

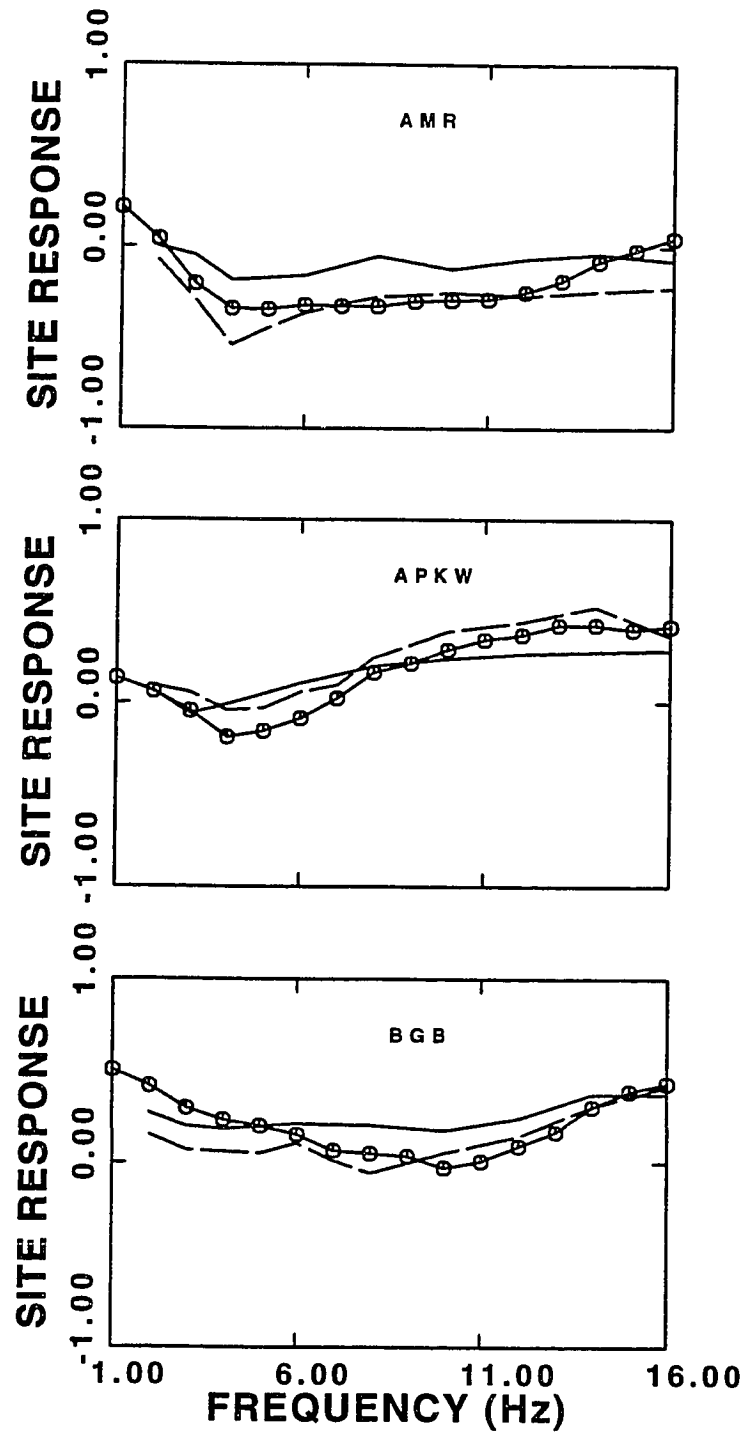


Figure 6.2d. Same as Figure 6.2a but for stations AMR, APKW, and BGB.

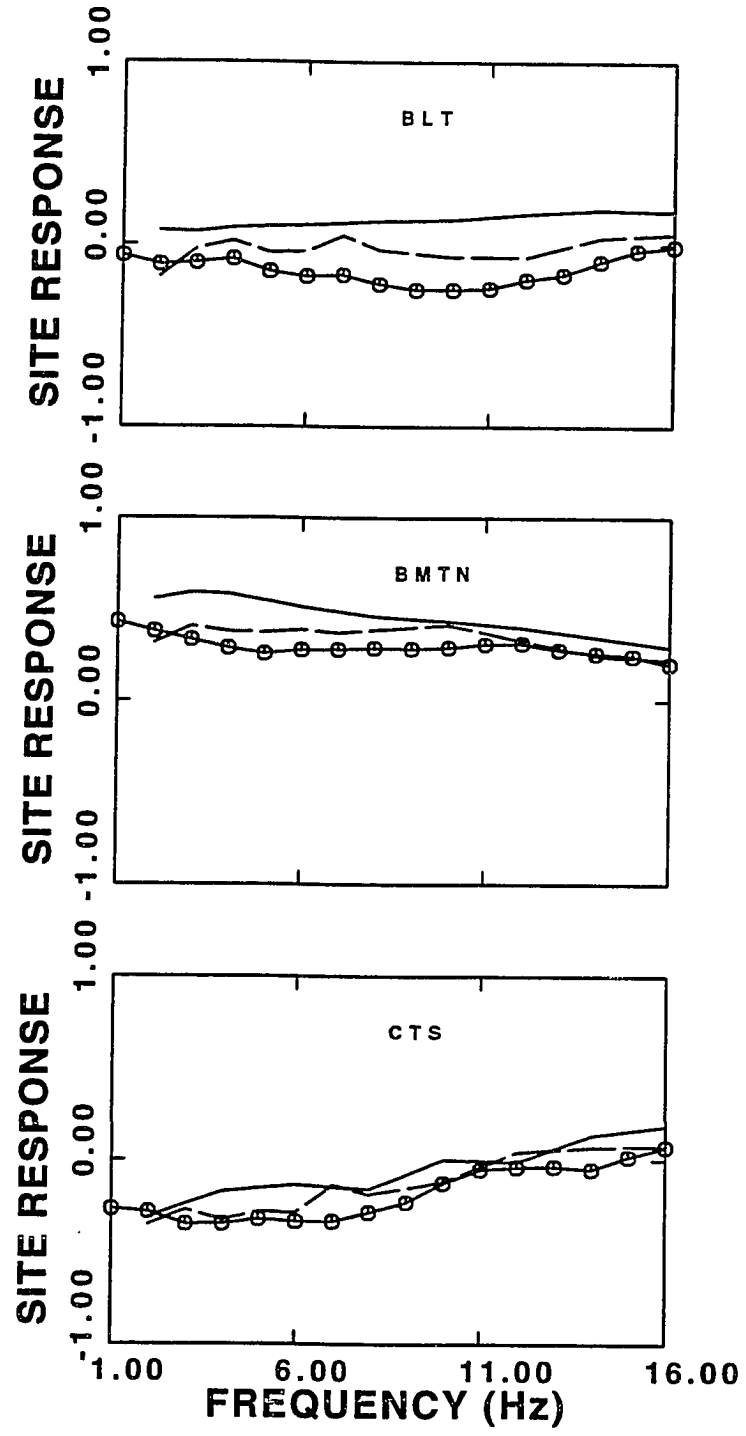


Figure 6.2e. Same as Figure 6.2a but for stations BLT, BMTN, and CTS.

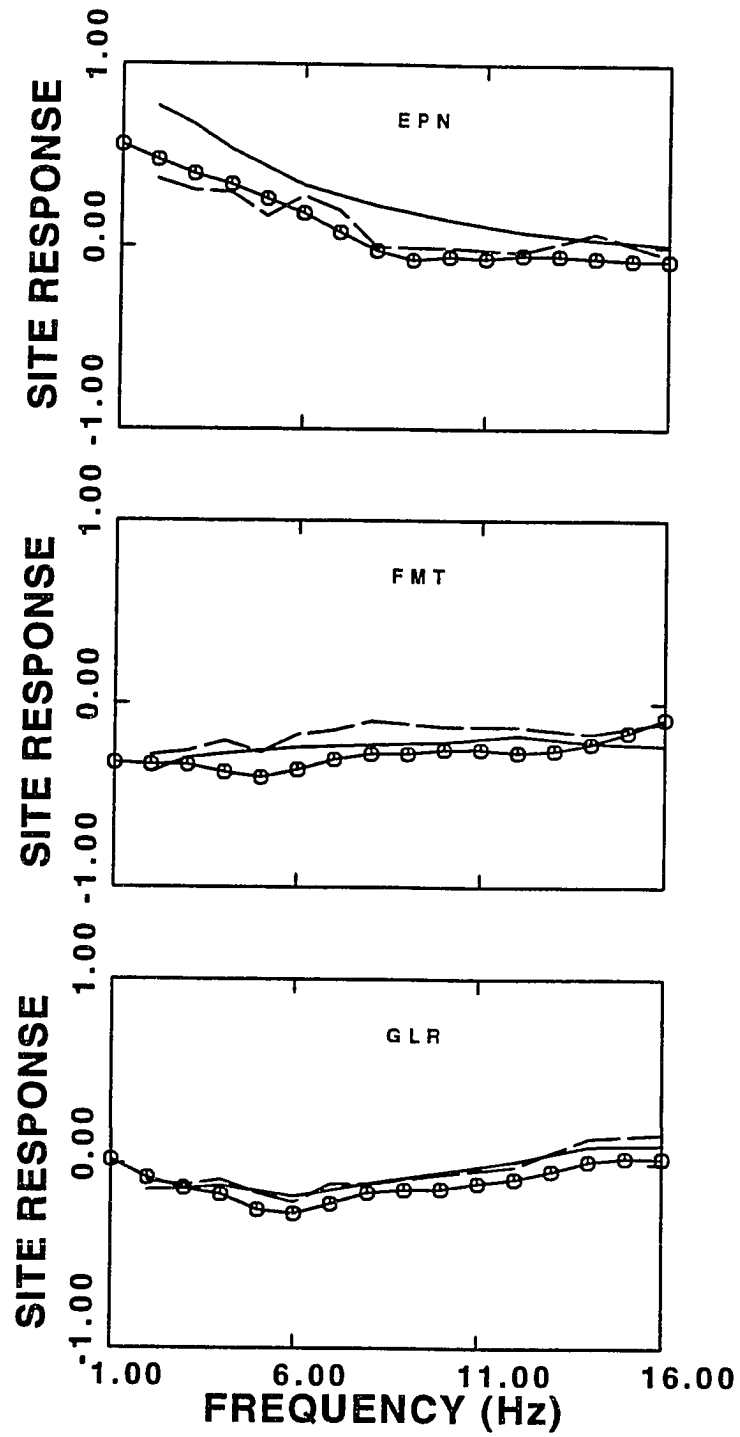


Figure 6.2f. Same as Figure 6.2a but for stations EPN, FMT, and GLR.

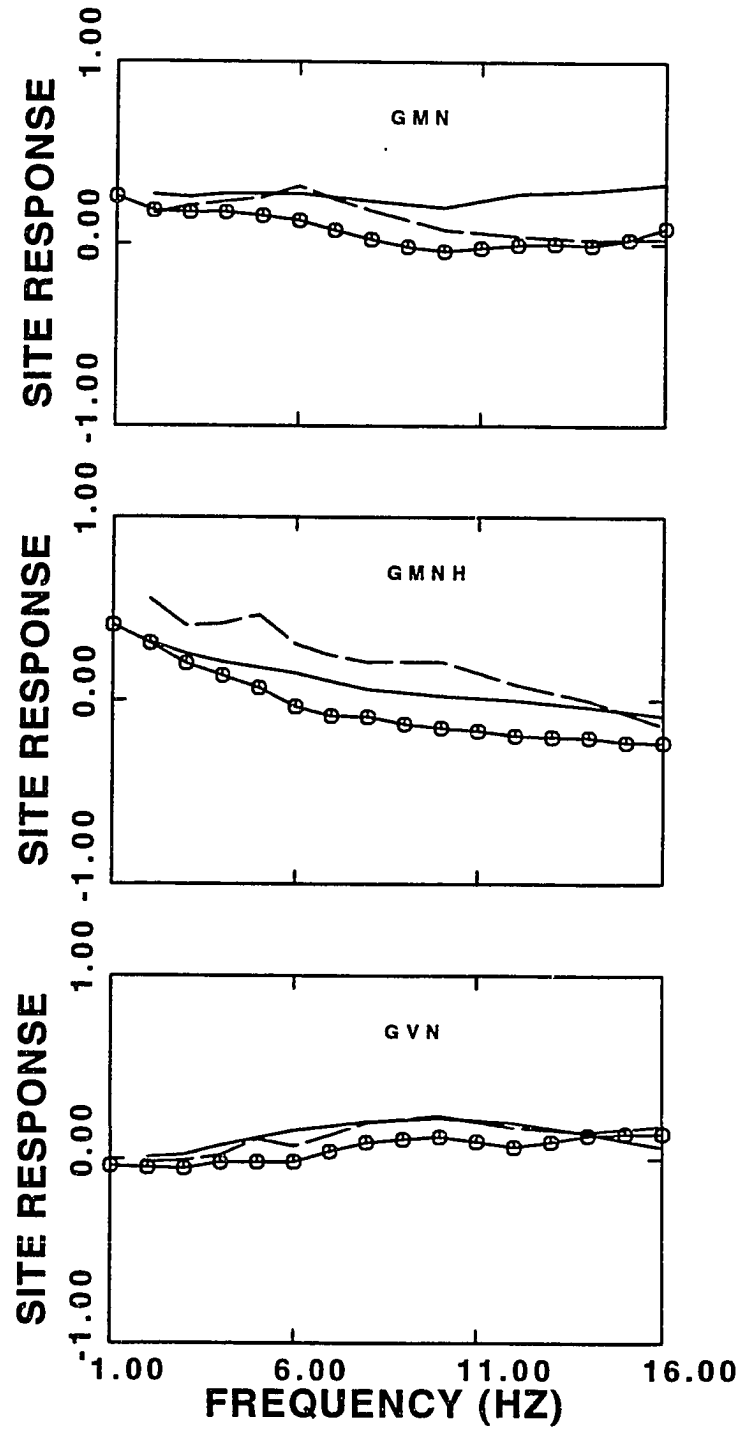


Figure 6.2g. Same as Figure 6.2a but for stations GMN, GMNH, and GVN.

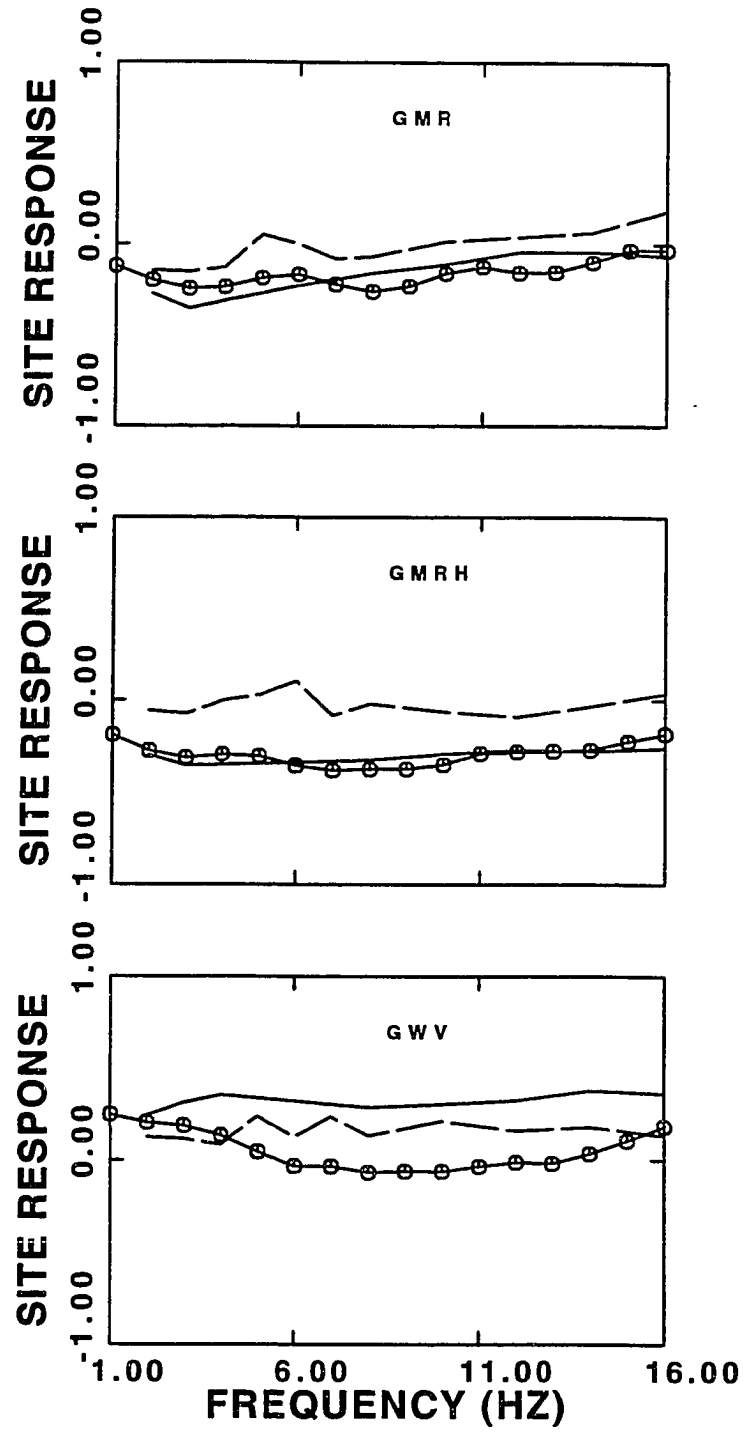


Figure 6.2h. Same as Figure 6.2a but for stations GMR, GMRH, and GWV.

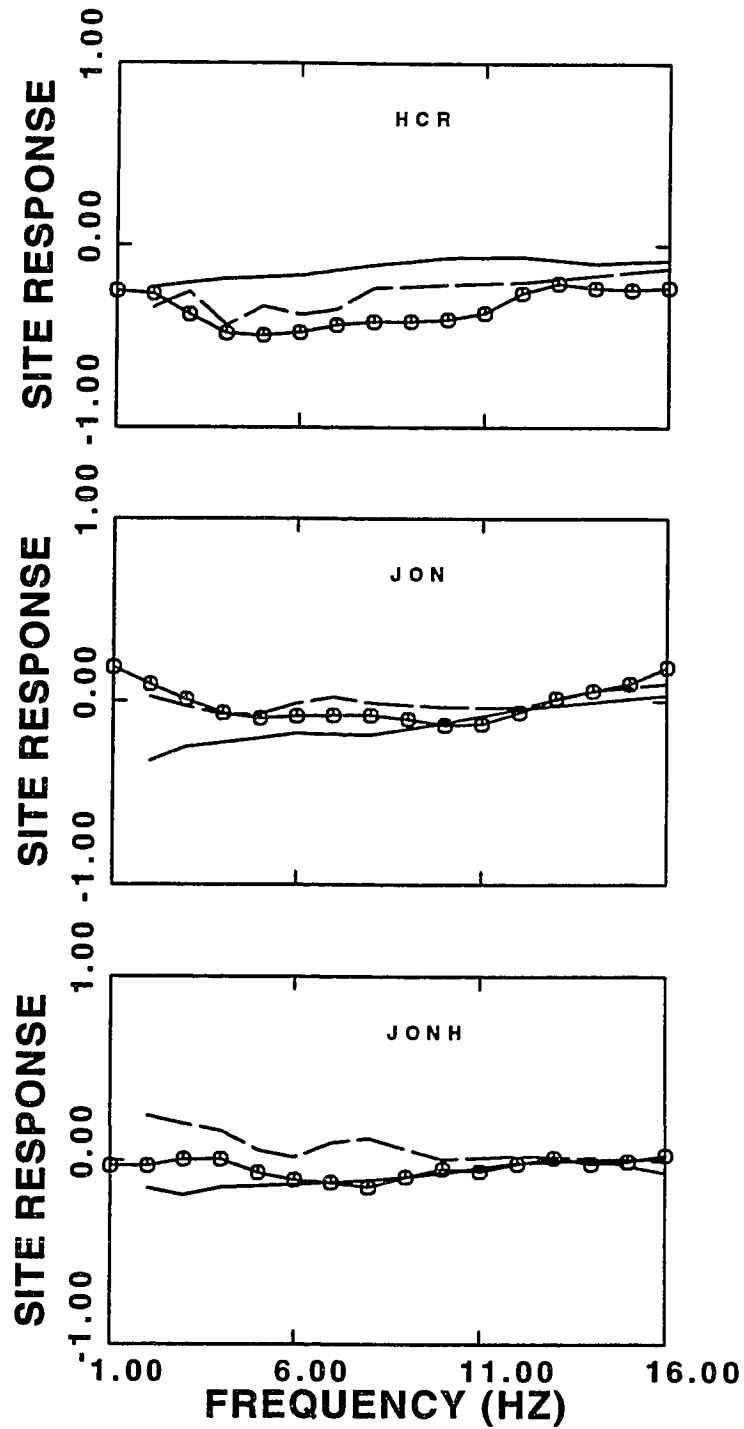


Figure 6.2i. Same as Figure 6.2a but for stations HCR, JON, and JONH.

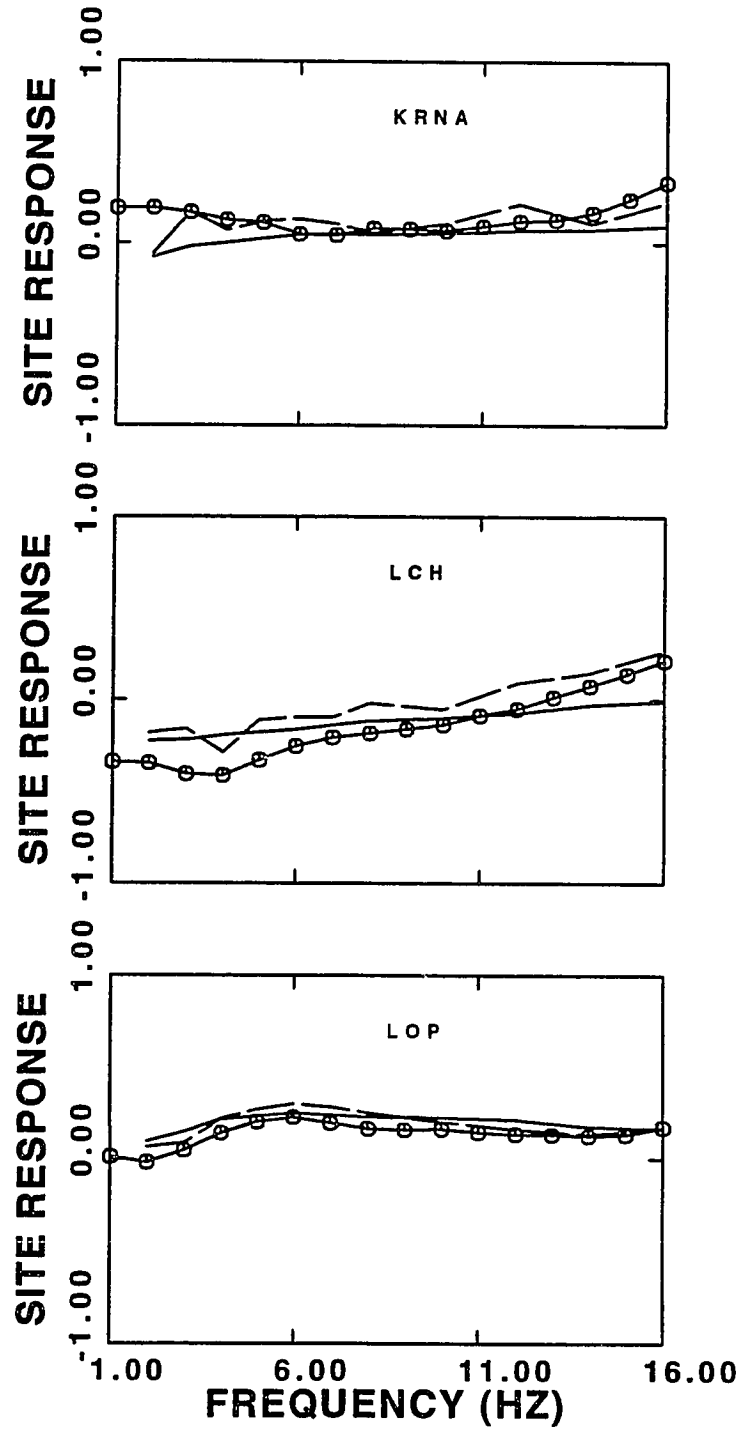


Figure 6.2j. Same as Figure 6.2a but for stations KRNA, LCH, and LOP.

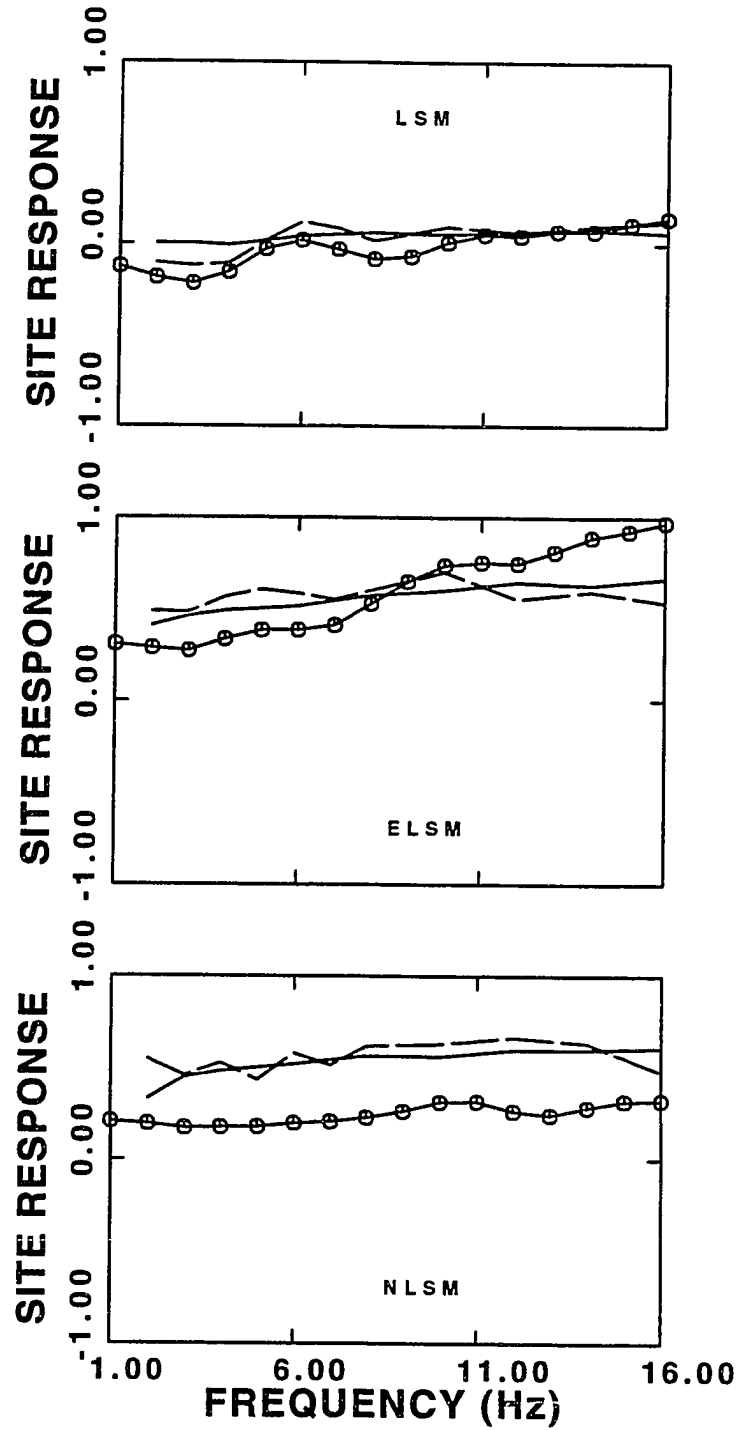


Figure 6.2k. Same as Figure 6.2a but for stations LSM, ELSM, and NLSM.

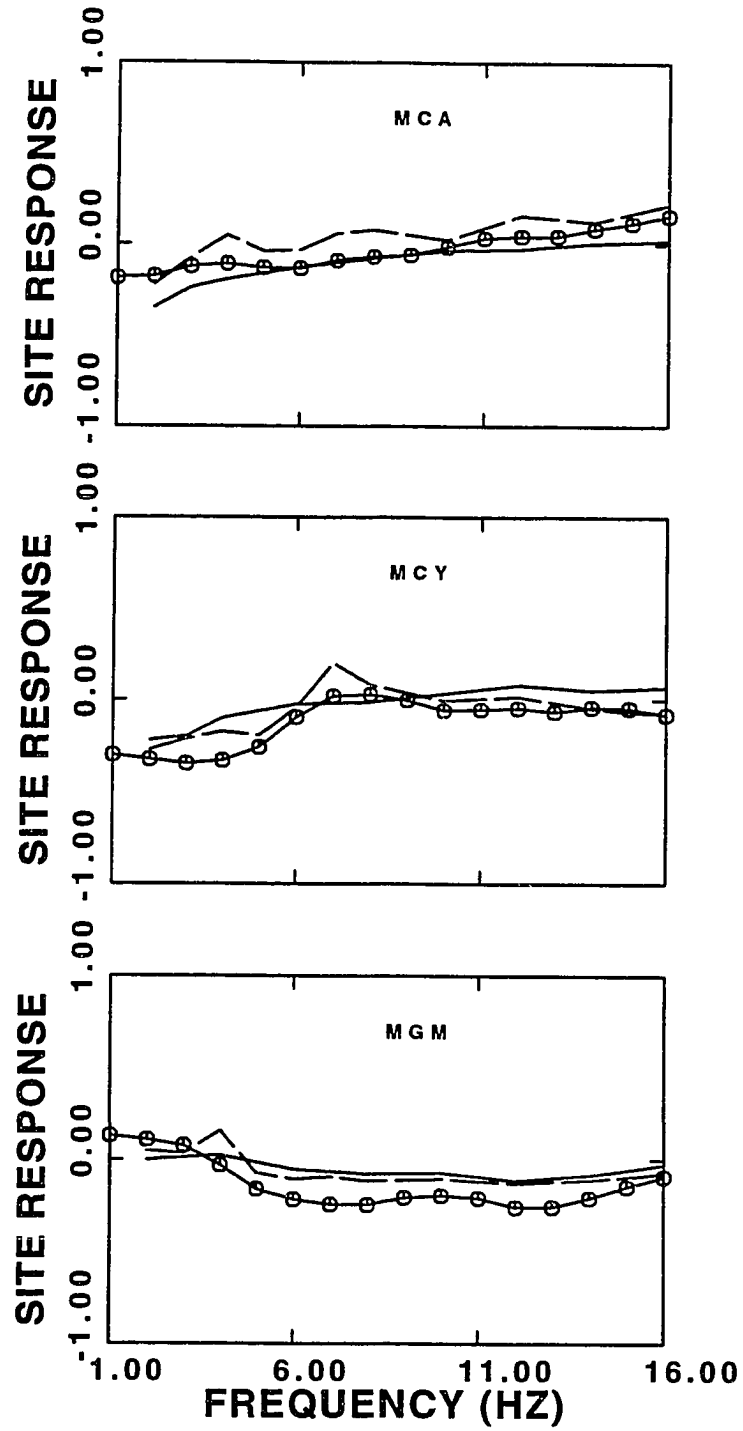


Figure 6.2l. Same as Figure 6.2a but for stations MCA, MCY, and MGM.

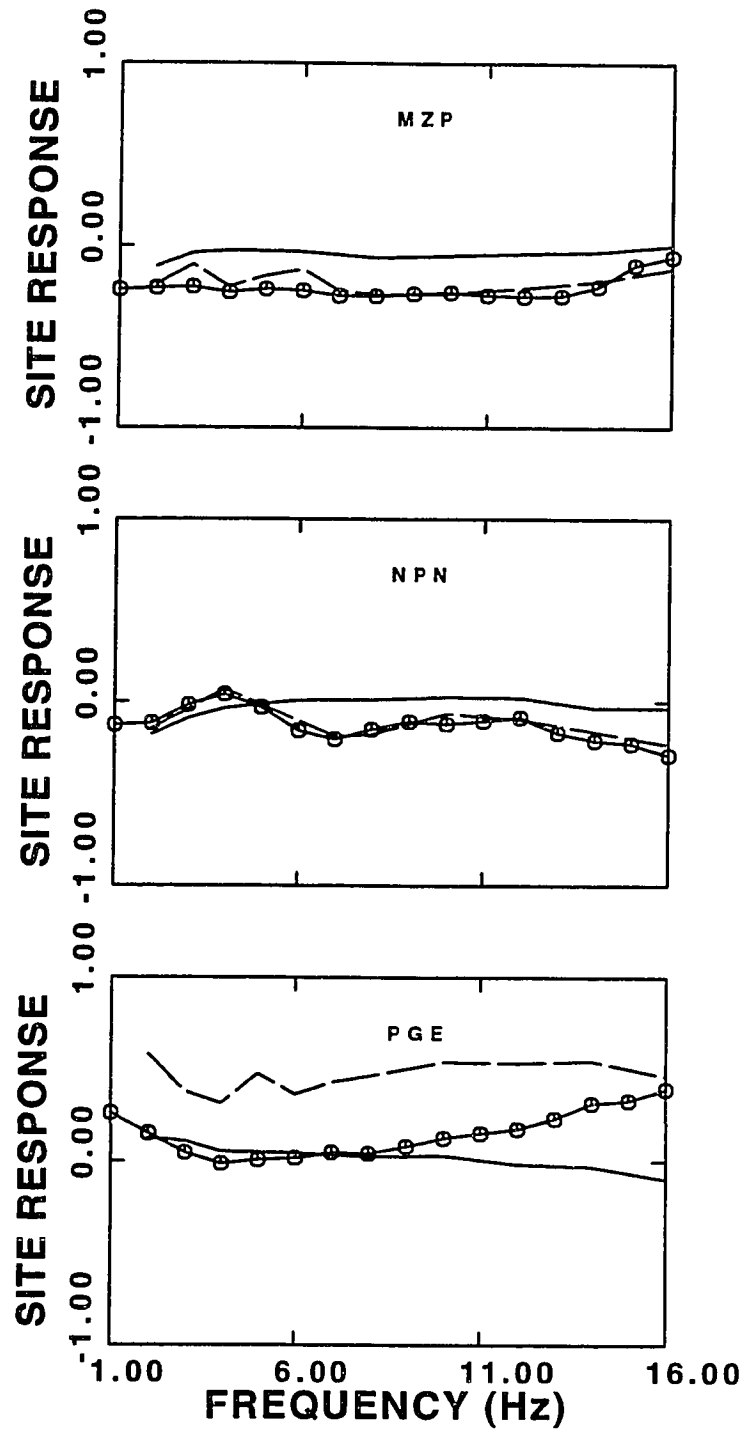


Figure 6.2m. Same as Figure 6.2a but for stations MZP, NPN, and PGE.

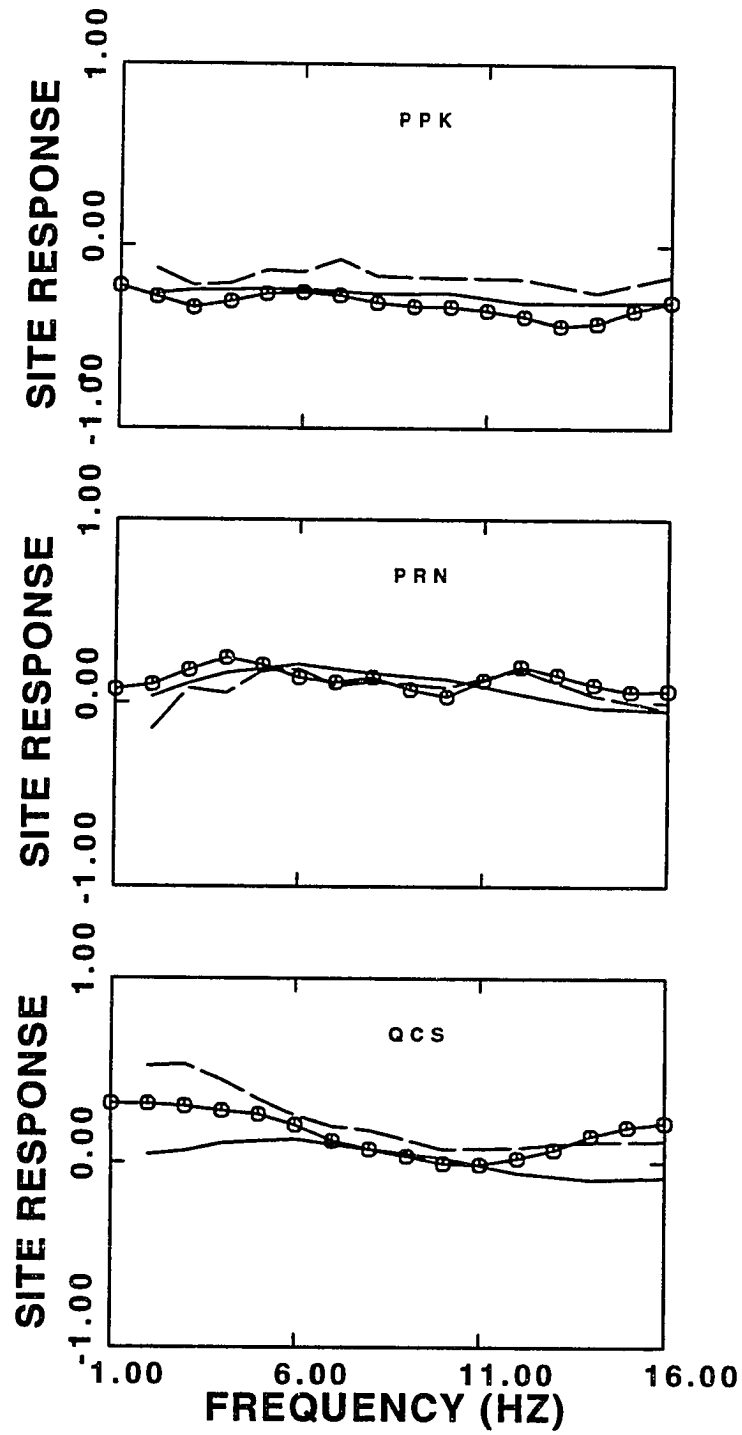


Figure 6.2n. Same as Figure 6.2a but for stations PPK, PRN, and QCS.

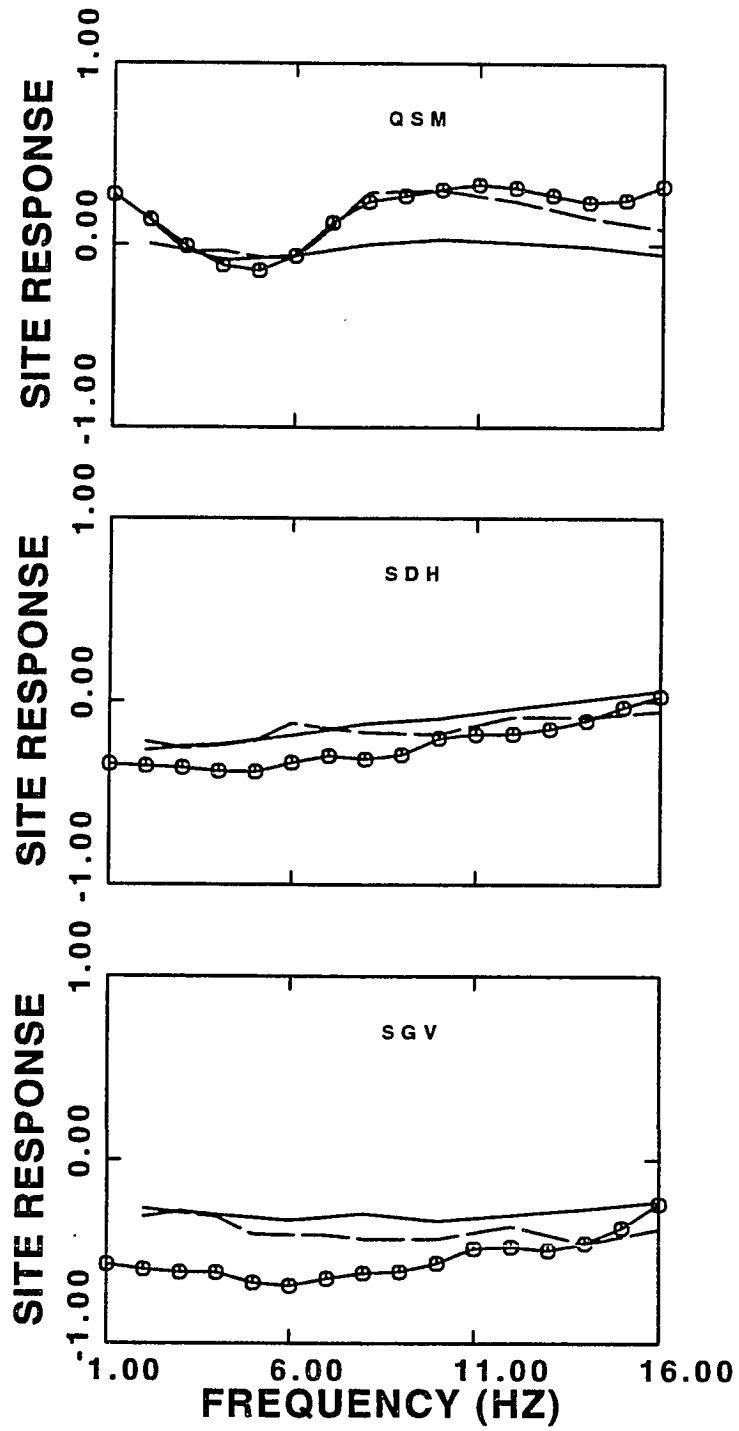


Figure 6.2o. Same as Figure 6.2a but for stations QSM, SDH, and SGV.

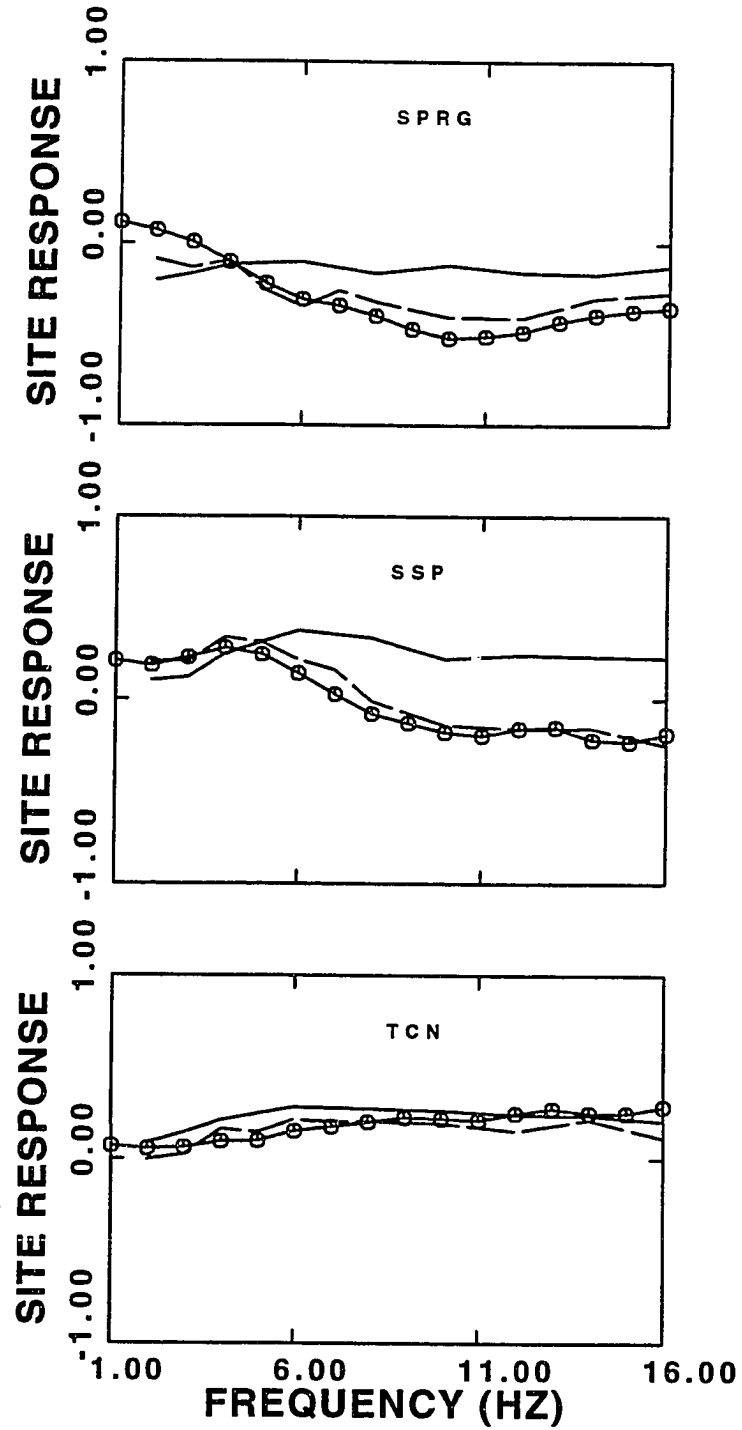


Figure 6.2p. Same as Figure 6.2a but for stations SPRG, SSP, and TCN.

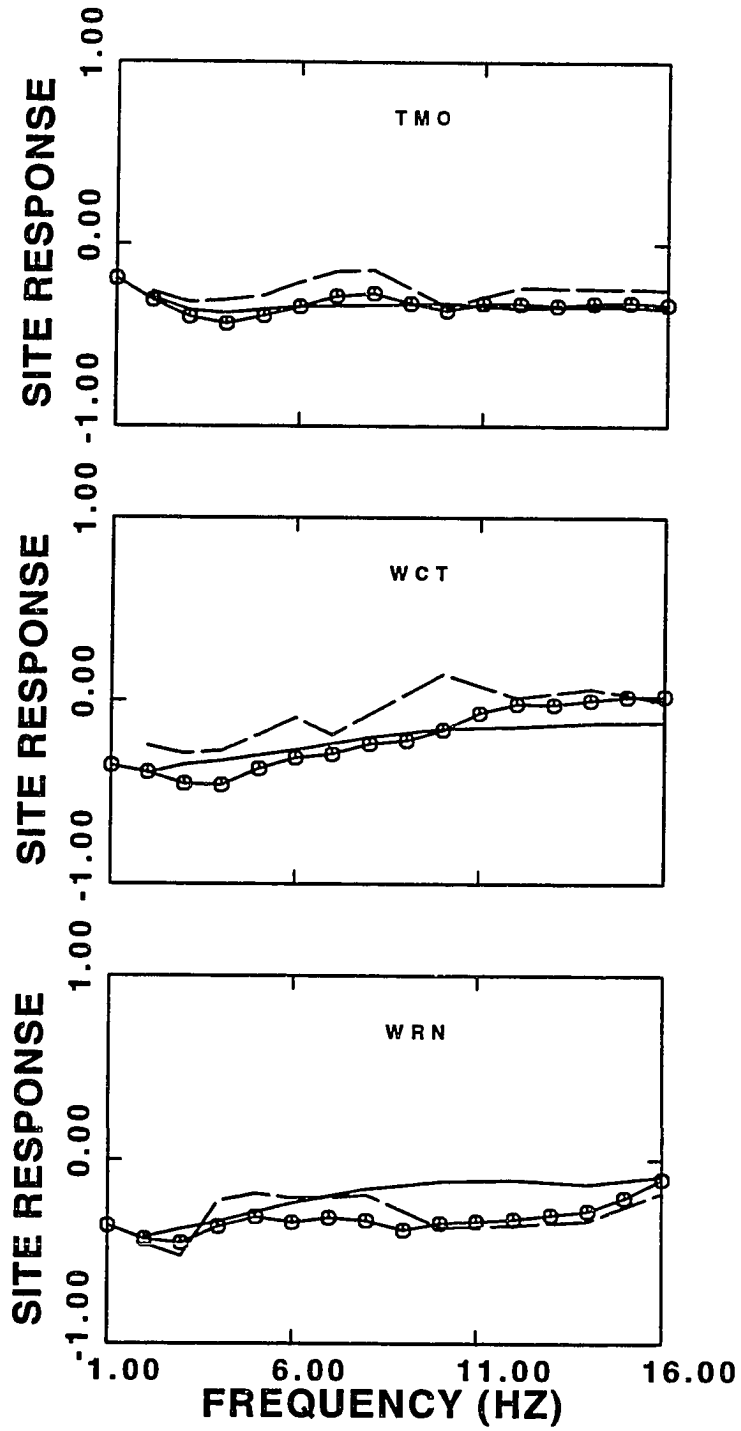


Figure 6.2q. Same as Figure 6.2a but for stations TMO, WCT, and WRN.

6.3 Site amplification from the S wave phases

The separability of source, site, and path effects of ground motion was utilized earlier in the calculation of whole path attenuation. The regression model

$$A(f,r) = S(f) Z(f) G(r) e^{-\gamma r} \quad (6)$$

is employed to invert for these parameters. We imposed the constraints of $\sum_{i=1}^N \log z_i = 0$, where N is the total number of stations on hard rocks used for the regression. Without this constraint an arbitrary function of frequency can be added to the logarithm of the site term and subtracted from the logarithm of the source term.

Results

The geometrical spreading factor, $G(r)$, plays a major role in calculating attenuation values. Different models of geometrical spreading were assumed and the site terms calculated are basically independent of the type of model used. We also calculated the source terms for frequencies 2 to 20 Hz for 42 earthquakes used in this study. In Figure 6.3 we show the source spectra for all earthquakes used in this study. The source terms are generally in agreement with a ω -squared source model in which the source spectrum is constant for frequencies less than a corner frequency, f_c and a falloff proportional to f^{-2} above f_c . We find $f_c \approx 10$ Hz for all earthquakes used for this study. The low frequency level of the source spectrum

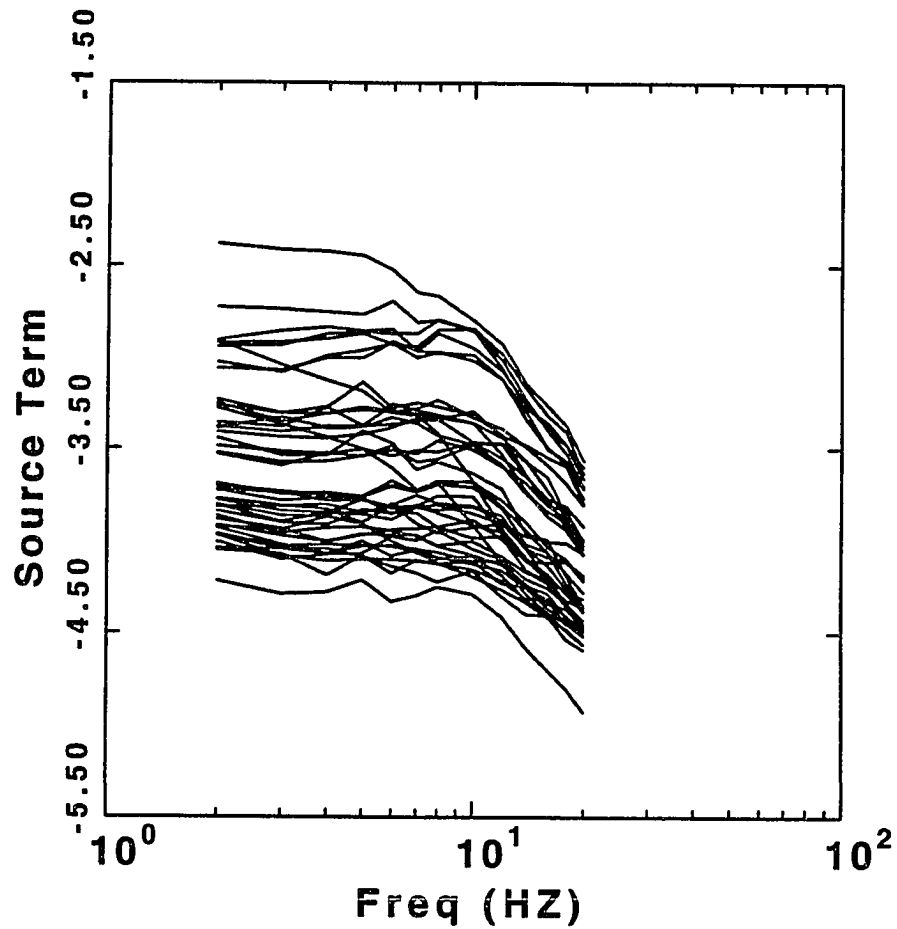


Figure 6.3. Source terms of all the events used for the regression of SV data. The source terms are adjusted to be proportional to displacements. Notice that the corner frequencies are between 8 to 12 Hz and that the asymptotic zero frequency source terms vary more than two order of magnitudes.

varies within two orders of magnitude while the high frequency level varies less. The m_{bLg} magnitudes for these events reported by Harmsen and Rogers (1987) are between 0.9 and 2.2 which is consistent with the low frequency variations.

6.4 Site effects using spectral model

A theoretical amplitude spectrum is described as a function of source, path, and receiver. The spectrum model, $A(f)$, is based on source model of Brune (1970) and is given by:

$$A(f,r) = \frac{F^{Z,R,orT} G(r) M_0}{4 \pi \rho \beta^3} \frac{(2\pi f)^2}{1 + (f/f_c)^2} e^{-\pi f \kappa} \quad (6.7)$$

In this equation, M_0 is the seismic moment, f_c is the source corner frequency, κ is the spectral decay parameter, r is the source to station distance, ρ is the average rock density near the source, β is the shear-wave velocity, $G(r)$ is the geometrical attenuation factor, and $I(f)$ is the instrument response at frequency f . $F^{Z,R,orT}$ is a factor accounts for the average shear-wave radiation pattern, amplification due to the free surface, and partitioning of energy into three components. We take the average of F for the three Z, R, and T components to be equal to 0.85.

The spectral decay parameter κ can be realized as a linear combination of a local term κ_0 plus a regional attenuation factor proportional to distance:

$$\kappa = \kappa_0 + r\kappa_2 . \quad (6.8)$$

The spectral decay operator can be written as

$$e^{-\pi\kappa f} = e^{-\pi\kappa_0 f} e^{-\pi f r \kappa_2} . \quad (6.9)$$

In this representation, κ_1 is related to the whole path attenuation $\gamma = \pi f \kappa_2$ or ,

$$e^{-\pi\kappa f} = e^{-\pi\kappa_0 f} e^{-\gamma R} , \quad (6.10)$$

where $\gamma = \pi f \kappa_1 = \pi f / Q\beta$.

After determining the source and path parameters, M_0 , f_c , κ_0 and γ through a non-linear inversion, the difference between the spectrum of a large time window of S-wave and the model spectrum based inversion on each individual record, is interpreted as the site amplification term (Humphrey and Anderson (1992)

$$Z_{i,j} = \log S_i(f) - \log A_j(f,r) . \quad (6.11)$$

The residual, $Z_{i,j}(f)$ represents the deviation from an idealized spectrum at station i recorded at distance r due to earthquake j at frequency f . We adopted a non-linear technique developed by Ou (1990). The value of γ calculated from the regression method in Chapter 3 is used here. We determine two source parameters, M_0 , f_c , and the site attenuation parameter κ_0 , by the non-linear Marquardt method (1963). In Figure 6.4 we show one example of this

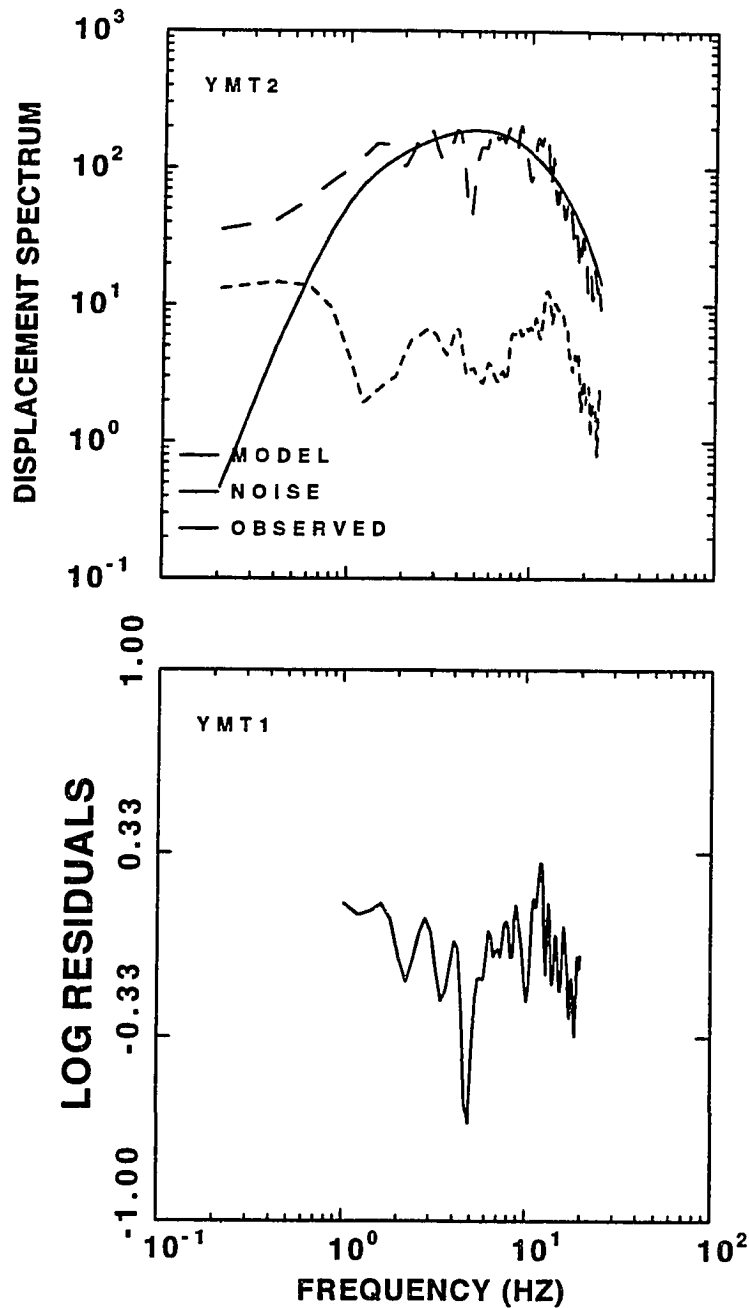


Figure 6.4. Displacement spectrum of S waves (top). The observed spectrum of S waves is shown by long broken lines, the noise spectrum by the short dashed lines, and the modeled spectrum by the solid line. The difference between the observed and the modeled spectrum is shown in the bottom figure.

procedure of one earthquake recorded at station YMT1. Figure 6.4a shows S-wave spectrum observed, modeled S-wave spectrum, and the noise spectrum. The difference between the observed and the modeled spectrum is shown at the bottom of Figure 6.4b.

Spectral parameters

The regional attenuation parameter, γ , was calculated using a linear regression analysis of the ground motion. An attempt is made to invert for M_0 , f_c and κ_0 for each record. In general the inversion on an individual record of a given earthquake did not converge to a single f_c . Usually, corner frequencies were scattered as much as 5 Hz to 15 Hz. Our linear regression of response spectra data, however, resulted in a very reasonable source term. This is demonstrated in Figure 6.3. The asymptotic zero frequency part of the source terms are proportional to M_0 , and the corner frequencies are between 8 to 12 Hz for all the earthquakes used in this study. We performed the inversion for all the records of a given earthquake leaving M_0 as a free parameter to be determined by the inversion. κ_0 was initially fixed at $\kappa_0 = 0.01$ seconds. The real effect of κ_0 on any calculation becomes significant at higher frequencies, $f > 10$ Hz. After the first round of inversion was performed on all the records of one earthquake, an average of M_0 was determined and supplied to the spectral model formula to calculate the model spectra. The residual of the observed spectrum and the model

spectrum of all recorded earthquakes at a given station was then averaged. This average residual is our initial estimate of the site terms.

After comparing the site terms from the linear regression method and the site terms calculated based on the residuals between observed and modeled spectra it was found that for frequencies greater than roughly 8 Hz the site response terms based on spectral modeling increase linearly with frequency for some stations. Any incorrect assumption about κ_0 in the operator $e^{-\pi f \kappa_0}$ can exaggerate this linear trend. The linear increase is more pronounced for stations located on Paleozoic and older rock. For these sites we adjust κ_0 accordingly. The non-linear inversion procedure is repeated with the revised values of κ_0 and the average residual calculated are interpreted as the site response for the network. This procedure is usually fast and because the κ_0 terms have minimum effect on low frequency end of the spectrum, adjustment of κ_0 does not alter the other spectral parameters. In Table 6.2, the site attenuation parameter, κ_0 is tabulated along with a brief geological description for all stations in the network.

TABLE 6.1

Site geology and site attenuation parameter of SGBSN

STATION NAME	ROCK ROCK	GEOLOGIC AGE	κ_o
AMR	Conglomerate	Tertiary	0.04
APKW	Limestone, dolomite	Paleozoic	0.01
BGB	Bedded tuff	Tertiary	0.03
BLT	Ash-flow tuff	Tertiary	0.02
BMTN	Trachyte lava	Tertiary	0.005
CDH1	Argillite	Mississippian	0.01
CPY	Limestone	Cambrian	0.015
CTS	Intrusive mafic rocks	Tertiary	0.015
DLM	Limestone, dolomite	Paleozoic	0.015
EPR	Volcanic rock	Tertiary	0.01
FMT	Metamorphic rock	Precambrian	0.01
GLR	Limestone and dolomite	Paleozoic	0.02
GMN	Granite	Mesozoic	0.015
GMR	Limestone and dolomite	Paleozoic	0.015
GVN	Fanglomerate	Tertiary	0.01
GWY	Volcanic rocks	Miocene	0.03
HCR	Ash-flow tuff	Tertiary	0.01
JON	Quartzite	Precambrian	0.025
KRNA	Ash-flow tuff	Tertiary	0.04
LCH	Limestone and dolomite	Cambrian	0.01
LOP	Lava	Tertiary	0.015
LSM	Basalt	Tertiary	0.01
MCA	Limestone, dolostone	Paleozoic	0.015
MCY	Dolomite, limestone	Devonian	0.01

TABLE 6.1 (continued)

STATION NAME	ROCK TYPE	GEOLOGIC AGE	κ_0
MGM	Quartzite	Precambrian	0.01
MTI	Carbonates	Devonian	0.01
MZP	Volcanic tuffs	Tertiary	0.012
NOP	Limestone	Paleozoic	0.02
NPN	Ash-flow	Tertiary	0.015
PPK	Granite	Mesozoic	0.01
PRN	Ash-flow tuff	Tertiary	0.01
QCS	Basalt	Tertiary	0.04
QSM	Tuff	Tertiary	0.03
SDH	Quartzite	Precambrian	0.008
SGV	Rhyolite	Miocene	0.01
SPRG	Tuffaceous sediments	Tertiary	0.01
SSP	Ash-flow tuff	Tertiary	0.02
TCN	Ash-flow tuff	Tertiary	0.02
TMBR	Granitic ring-dike intrusion	Tertiary	0.02
TMO	Limestone and dolomite	Paleozoic	0.02
TPU	Shales and sandstone	Mississippian	0.01
WCT	Alluvium of Crater Flat	Quaternary	0.02
WRN	limestone and dolomite	Ordovician	0.01
YMT1	Ash-flow tuff	Tertiary	0.007
YMT2	Welded tuff	Tertiary	0.01
YMT3	Welded Tuff	Tertiary	0.01
YMT4	Welded tuff	Tertiary	0.008
YMT5	Welded tuff	Tertiary	0.01
YMT6	Welded tuff	Tertiary	0.01

(Site geology description from Harmsen, personal communication)

6.5 Discussion and Conclusion

Figure 6.2 presents the site terms calculated from the three methods. Site response terms estimated from the coda method are shown by solid lines. Broken lines give the site response terms calculated based on the regression of the response spectra data. Lines with small circles are the site responses estimated from spectral modeling. There is general agreement between the coda method and the response spectra method. More significant is the agreement between the spectral method results and the response spectra results. The spectral method results tend to agree better with the response spectral results than with the coda results. Agreement of the three calculations is best when a large number of recordings is used for determination of the site effect at a station. We had more than fifteen recordings for each of the Yucca Mountain sites, YMT1-YMT6. Site terms calculated for horizontal sensors tend to differ more from each other than those for vertical sensors. This is probably because the ratio of vertical to horizontal motion is different for the main part of the signal. In addition, the number of observations per station for the horizontal sensors is usually fewer than vertical one. This can contribute to significant disagreement between site terms of different methods for the horizontal stations. The results demonstrate the adequacy of a frequency-independent Q model and a body-wave geometrical attenuation of $\frac{1}{r}$ for the S

waves. Since we adopted a ω -squared source model based on corner frequencies calculated from regression of the main ground motion, this model adequately describes ground motion of the small earthquakes used for this study.

Many of the sites examined here are located on top of very complex volcanic structure, some sites are on Paleozoic carbonate rocks, and, some sites are on Pre-Cambrian metamorphic rocks. We found a correlation between the site term and geology of the rocks of different sites. The geology and age given in Table 6.1 are preliminary survey of the USGS (Harmsen, personal communication). In the Yucca Mountain sites, we notice a decreasing trend of site terms versus frequency. YMT1 site has a larger positive term in lower frequencies than YMT3, YMT5, and YMT6. As the preliminary survey indicates, some of the Yucca Mountain site volcanic Tuff are welded. The degree of welding can reduce pore space in rocks. A larger impedance of porous rocks can explain large positive site terms at lower frequencies. In two studies conducted by the United States Geological Survey (Nelson *et al.*, 1991; and Hagstrum *et al.*, 1980), it was observed that the ash-flow and bedded tuff sequence at the Nevada Test Site of the Southern Great Basin comprise complex lithologies of variously welded tuffs with superimposed crystallization and altered zones. To characterize these units, resistivity, density, neutron, gamma-ray, well-log measure-

ments were made. It was found that welding and alteration of the tuffs are dominant geological controls on the response of the density, velocity, neutron, and resistivity logs. Variation in thickness, density, and porosity can effect seismic impedance which is directly related to site amplification. The majority of volcanic tuff sites have a positive site term at 2 Hz with a decreasing trend toward 16 Hz. In Figure 6.5, the averaged frequency dependent site terms of volcanic-tuff are compared to those of carbonate rock sites.

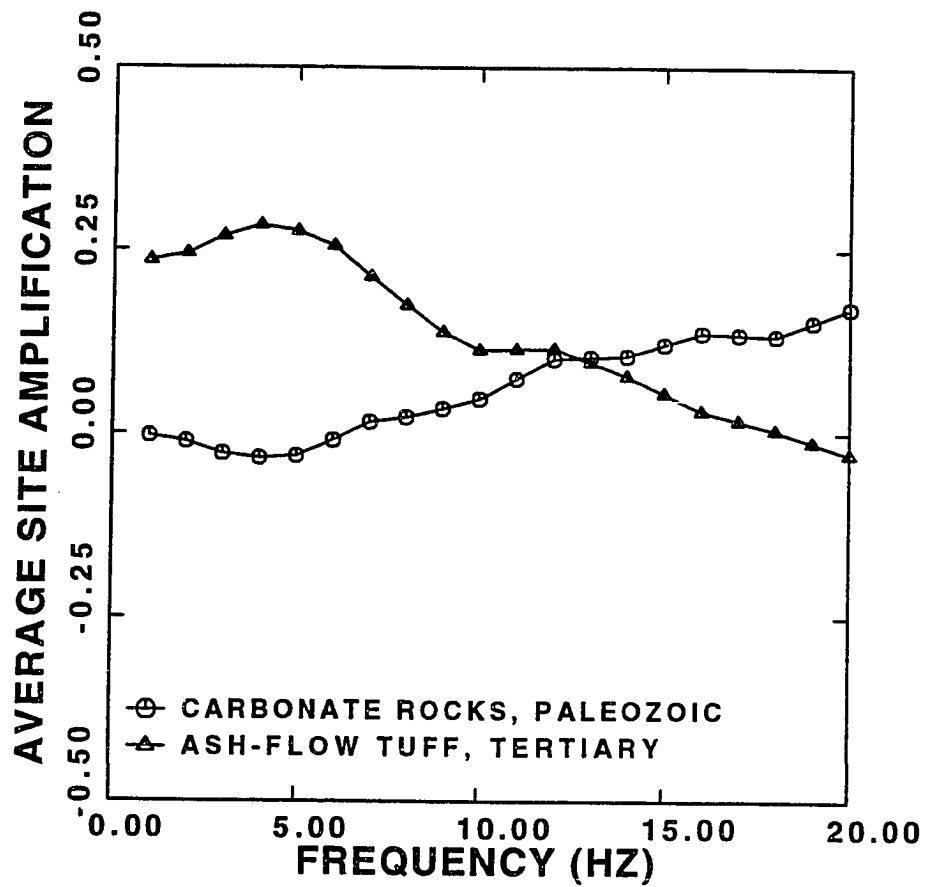


Figure 6.5. Average site amplification for frequencies 1 to 20 Hz for a group of stations located of Paleozoic carbonated rocks and for Tertiary Ash-Flow Tuff. Notice two opposite frequency trends for these two group of stations.

CHAPTER 7

CONCLUSIONS

The attenuation of ground motion and attenuation of the coda wave were calculated in the Southern Great Basin of Nevada and California using network data of small earthquakes. Measurements of ground motion were performed by calculating response spectra of each record. We found that response spectra present an efficient and powerful method for quantifying ground motion for attenuation studies. To obtain response spectra we reconstructed the ground motion time history for the entire seismogram. A recursive method based on zero phase deconvolution using a cascade of filters was designed to remove instrument response.

We measured the attenuation of S waves, direct S wave, Lg wave, PSRV, and SV. S waves are referred to as the peak amplitude observed after the onset of S phase for the entire distance range of 0 to 200 km, while the direct S wave and Lg are referred to the peak amplitude after the onset of S for the distance range of 0 to 60 km and greater than 120 km, respectively. These terms were used in our study of coda normalized motion. PSRV and SV measurements do not isolate any particular phase and because they depend upon the entire S-wave train, including part of the coda,

their definition apply to the entire distance range.

In Chapter 3, a response spectra data set was constructed after removing instrument response. Response spectra amplitude were modeled as a product of source, site, attenuation, and geometrical spreading operators. A linear regression method with a single geometrical spreading mechanism of $\frac{1}{r}$ for the entire distance range produced negative values of Q at low frequencies and high values of Q for frequencies 2 to 4 Hz. This was also seen when the geometrical spreading was $\frac{1}{r^{5/6}}$. In order to obtain lower values of Q one has to assume geometrical spreading not acceptable physically for the propagation of elastic waves at short distances. By allowing segmented geometrical spreading, stable and satisfactory results are produced. The geometrical spreading was determined to be close to r^{-1} for distances less than 60 km, $r^{-0.6 \pm 0.15}$ for $125 > r > 60$ km, and $r^{-5/6}$ for $r > 125$ km. A bilinear regression with a critical distance of $d_c = 60$ km results in Q values close to those from a trilinear regression. The Q values range between 500 to 1400 for frequencies from 2 Hz to 16 Hz. Q is relatively constant between 2 Hz to 8 Hz with $Q(f) \approx 600 f^{0.1}$ for the PSRV and slightly higher values for the SV. Q values are strongly frequency dependent for the higher frequency range of 8 Hz to 20 Hz with $Q = 150 f^{0.8}$. We applied the single scattering model to obtain the coda Q . The fre-

quency dependent Q from coda waves was calculated to be $Q=150 f^{0.9}$ for the entire frequency band of 2 Hz to 16 Hz. We found that the coda decays uniformly with time with constant rate even at large lapse times up to 100 seconds. Our data support the general observation of Rogers *et al.* (1987) of the different Q values of Lg wave and the coda waves for frequencies less than 6 Hz. Q values for peak ground motion for the distance range of this study is highly geometrical spreading related.

Following Aki (1981) a coda normalization method was applied to find Q of S waves, comprising the peak amplitude of local seismograms, and Q of Lg waves. We found that the coda method is a very useful and powerful method because of the uniformity of coda decay. After the separability of source-path and uniformity of coda decay was tested, we used the coda as a tool to remove the effects of instrument, source, and site. This offered a fast and efficient method to calculate the S-waves attenuation measurement at short distances as well as measurement of attenuation of Lg at larger distances. A striking feature of plots of the coda normalized amplitudes versus hypocentral distance are the local peak at around 120 km which necessitates a segmented geometrical spreading factors with the critical distances of 60 and 120 km. We performed a trilinear regression on the coda normalized S waves amplitude. The Q values obtained from this analysis support our

results from the regression of the response spectra data.

Xie and Mitchell (1991) obtained the relation $Q_{Lg}(f) = 267 f^{0.37}$ and $Q_c = 275 f^{0.36}$ for the Basin and Range at frequencies between 0.2 to 2.5 Hz using broad-band data with the distance range of 300 to 2800 km. The equivalence of Q_{Lg} and Lg coda Q implies that the attenuation is due to intrinsic anelasticity. It also leads to a model in which intrinsic shear wave Q is very low (≈ 50) in the upper crust (Mitchell and Xie, 1994). The data used in our study, however, is dominated by seismograms with average epicentral distances around 50 km as is evident from Figure 1.2. S waves traveling in regional distances are set up in a crustal waveguide whereas the S waves traveling at short distances are subject to scattering by layering in the upper crust. We study the coda wave Q and the S waves Q at frequencies between 2 Hz to 16 Hz but our 2 Hz values have large error bars. The frequency bands used in our work and the work by Xie and Mitchell (1991) barely overlap and therefore different values of Q at 1-2 Hz are not necessarily inconsistent because of the large error bars in our estimation at those frequencies. Xie and Mitchell (1991) results apply to a much broader geographical region than ours and the combination of the two studies provides a picture of crustal attenuation process in the 0.2-16 Hz band.

The attenuation of the direct S wave for $r < 60$ km exhibits a greater rate of decay versus distance and their Q values are close to

Q_c . A frequency-independent Q model with a uniform geometrical spreading of $\frac{1}{r}$ for all distances from 0 to 200 km fits the S waves data well. Frequency-independent Q is found to be roughly 1100 for the direct S and 1600 for the peak amplitude of S waves. In Table 7.1 we summarize frequency-dependent Q values obtained from different methods.

TABLE 7.1. Q relations in SGB

Data	Method	Frequency range	Result
PSRV	Trilinear regression	2-8 Hz	$Q \approx 600f^{0.1}$
PSRV	Trilinear regression	8-16 Hz	$Q = 150f^{0.8}$
S waves	Trilinear regression	2-6 Hz	$Q \approx 450f^{0.1}$
S waves	Trilinear regression	6-16 Hz	$Q = 150f^{0.8}$
Direct S wave	Linear regression	2-16 Hz	$Q = 170 f^{0.7}$
Coda waves	Single scattering model	2-16 Hz	$Q = 150 f^{0.9}$

In Chapter 5, we applied the method of radiative transfer energy to data from SGBSN to determine the frequency dependent scattering and intrinsic attenuation. Our analysis showed that low frequency propagation is dominated by scattering. Q_s^{-1} values are closer to Q_c^{-1} and it is highly frequency dependent. The fit to the model is generally better at frequencies higher than 6 Hz, where the

simple assumptions of homogeneously distributed scatterers for the lithosphere is more valid.

In Chapter 6 local site terms were calculated for the network using three different approaches. Site terms were calculated using the main ground motion. These terms were shown to be very close to the site terms from our coda method except for the horizontal components. A spectral model of the ground motion was assumed and the difference between the observed and the model spectrum was interpreted as the site terms. The results of this analysis are generally in good agreement with those based on regression techniques for stations that several earthquakes were recorded. Low frequency site terms from the spectral method and the regression methods are usually close. For some stations, the high frequency site terms calculated by the spectral method increase faster than the regression results. We reduce the difference by introducing a site dependent attenuation parameter. Younger volcanic tuff show higher site amplification terms at low frequencies which gradually decrease with increasing frequency. On the other hand, older carbonate rocks and granite sites are usually characterized by small site terms at low frequencies with increasing trend toward high frequencies.

APPENDIX A

RESPONSE SPECTRA

1. Introduction

For a description of the frequency content of the earthquake ground motion some type of frequency spectrum curve is required. Response spectra are plots of the maximum response of a simple oscillator to a component of the ground acceleration, plotted as functions of the natural period and damping of the oscillator. Another form of frequency spectrum which is widely used is the Fourier amplitude spectrum. In the following, after the definition of response spectra, an exact method to compute the response spectra will be reviewed. The relationship between the Fourier amplitude spectrum and response spectra will be demonstrated. We follow derivations of Nigam and Jennings (1968), and Hudson (1979).

Consider a viscously damped simple oscillator subjected to the base acceleration $a(t)$. The equation of the motion of the oscillator is given by

$$m\ddot{x} + c\dot{x} + kx = -ma(t) \quad (\text{A.1})$$

where m = mass; c = damping coefficient, and k = stiffness of the restoring elements. Dividing by m and setting $\omega = (\frac{k}{m})^{1/2}$ and

$\frac{c}{m} = 2\beta\omega$ in (A.1) gives

$$\ddot{x} + 2\beta\omega\dot{x} + \omega^2x = -a(t) \quad (\text{A.2})$$

where β = the fraction of critical damping, and ω = the natural frequency of the vibrations of the oscillator.

The general solution of (A.2) with the initial conditions $x(0)=0$ and $\dot{x}(0)=0$ is

$$x(t) = -\frac{1}{\omega\sqrt{1-\beta^2}} \int_0^t a(\tau) e^{-\omega\beta(t-\tau)} \sin\omega\sqrt{1-\beta^2}(t-\tau)d\tau \quad (\text{A.3})$$

2. Definition of Response Spectra:

SD = $|x(t)|_{\max}$ = Relative Displacement Response Spectrum

SV = $|\dot{x}(t)|_{\max}$ = Relative Velocity Response Spectrum

SA = $|\ddot{x}(t)+a(t)|$ = Absolute Acceleration Response Spectrum

PSRV = ω SD = Pseudovelocity Spectrum

PSRA = ω^2 SD = Pseudo Acceleration Spectrum

3. Computation of spectra for digitized data

Assuming that $a(t)$ may be approximated between two adjacent digitized time of t_i and t_{i+1} with a straight line then (A.2) can be written as

$$\ddot{x} + 2\beta\omega\dot{x} + \omega^2x = -a_i - \frac{\Delta a_i}{\Delta t_i} (t - t_i)$$

$$\begin{aligned}\Delta t_i &= t_{i+1} - t_i \\ \Delta a_i &= a_{i+1} - a_i\end{aligned}\quad (\text{A.4})$$

The solution of (A.4), for $t_i \leq t \leq t_{i+1}$ is given by

$$\begin{aligned}x &= e^{-\beta\omega(t-t_i)} \left[C_1 \sin \omega \sqrt{1-\beta^2} (t-t_i) + C_2 \cos \omega \sqrt{1-\beta^2} (t-t_i) \right] \\ &\quad - \frac{a_i}{\omega^2} + \frac{2\beta}{\omega^3} \frac{\Delta a_i}{\Delta t_i} - \frac{1}{\omega^2} \frac{\Delta a_i}{\Delta t_i} (t-t_i)\end{aligned}\quad (\text{A.5})$$

in which C_1 and C_2 are constants of integration. Setting $x = x_i$ and $\dot{x} = \dot{x}_i$ at $t = t_i$ and solving for C_1 and C_2 , it can be shown that

$$C_1 = \frac{1}{\omega \sqrt{1-\beta^2}} \left(\beta\omega x_i + \dot{x}_i - \frac{2\beta^2-1}{\omega^2} \frac{\Delta a_i}{\Delta t_i} + \frac{\beta}{\omega} a_i \right) \quad (\text{A.6a})$$

$$C_2 = x_i - \frac{2\beta}{\omega^3} \frac{\Delta a_i}{\Delta t_i} + \frac{a_i}{\omega^2} \quad (\text{A.6b})$$

Substitution of these values of C_1 and C_2 into (A.5) x and \dot{x} at $t = t_{i+1}$ are given by

$$\bar{x}_{i+1} = A(\beta, \omega, \Delta t_i) \bar{x}_i + B(\beta, \omega, \Delta t_i) \bar{a}_i \quad (\text{A.7a})$$

in which

$$\bar{x}_i = \begin{Bmatrix} x_i \\ \dot{x}_i \end{Bmatrix} \quad \bar{a}_i = \begin{Bmatrix} a_i \\ a_{i+1} \end{Bmatrix} \quad (\text{A.7b})$$

$$A = \begin{bmatrix} a_{11} & a_{12} \\ a_{21} & a_{22} \end{bmatrix} \quad B = \begin{bmatrix} b_{11} & b_{12} \\ b_{21} & b_{22} \end{bmatrix} \quad (\text{A.7c})$$

The elements of matrices A and B are given by

$$\begin{aligned}
 a_{11} &= e^{-\beta\omega\Delta t_i} \left(\frac{\beta}{\sqrt{1-\beta^2}} \sin \omega \sqrt{1-\beta^2} \Delta t_i + \cos \omega \sqrt{1-\beta^2} \Delta t_i \right) \\
 a_{12} &= \frac{e^{-\beta\omega\Delta t_i}}{\omega \sqrt{1-\beta^2}} \sin \omega \sqrt{1-\beta^2} \Delta t_i \\
 a_{21} &= -\frac{\omega}{\sqrt{1-\beta^2}} e^{-\beta\omega\Delta t_i} \sin \omega \sqrt{1-\beta^2} \Delta t_i \\
 a_{22} &= e^{-\omega\Delta t_i} \left(\cos \omega \sqrt{1-\beta^2} \Delta t_i - \frac{\beta}{\sqrt{1-\beta^2}} \sin \omega \sqrt{1-\beta^2} \Delta t_i \right)
 \end{aligned} \tag{A.7d}$$

$$\begin{aligned}
 b_{11} &= e^{-\beta\omega\Delta t_i} \left[\left(\frac{2\beta^2-1}{\omega^2\Delta t_i} + \frac{\beta}{\omega} \right) \frac{\sin \omega \sqrt{1-\beta^2} \Delta t_i}{\omega \sqrt{1-\beta^2}} + \left(\frac{2\beta}{\omega^3\Delta t_i} + 1 \right) \cos \omega \sqrt{1-\beta^2} \Delta t_i \right] \\
 &\quad - \frac{2\beta}{\omega^3\Delta t_i}
 \end{aligned}$$

$$\begin{aligned}
 b_{12} &= -e^{-\beta\omega\Delta t_i} \left[\left(\frac{2\beta^2-1}{\omega^2\Delta t_i} \right) \frac{\sin \omega \sqrt{1-\beta^2} \Delta t_i}{\omega \sqrt{1-\beta^2}} + \frac{2\beta}{\omega^3\Delta t_i} \cos \omega \sqrt{1-\beta^2} \Delta t_i \right] \\
 &\quad - \frac{1}{\omega^2} - \frac{2\beta}{\omega^3\Delta t_i}
 \end{aligned}$$

$$\begin{aligned}
 b_{21} &= e^{-\beta\omega\Delta t_i} \left[\left(\frac{2\beta^2-1}{\omega^2\Delta t_i} + \frac{\beta}{\omega} \right) \left(\cos \omega \sqrt{1-\beta^2} \Delta t_i - \frac{\beta}{\sqrt{1-\beta^2}} \sin \omega \sqrt{1-\beta^2} \Delta t_i \right) \right. \\
 &\quad \left. - \left(\frac{2\beta}{\omega^3\Delta t_i} + \frac{1}{\omega^2} \right) \left(\omega \sqrt{1-\beta^2} \sin \omega \sqrt{1-\beta^2} \Delta t_i + \beta \omega \cos \omega \sqrt{1-\beta^2} \Delta t_i \right) \right] \\
 &\quad + \frac{1}{\omega^2\Delta t_i}
 \end{aligned}$$

$$\begin{aligned}
b_{22} = & -e^{-\beta\omega\Delta t_i} \left[\frac{2\beta^2-1}{\omega^2\Delta t_i} \left(\cos\omega\sqrt{1-\beta^2}\Delta t_i - \frac{\beta}{\sqrt{1-\beta^2}} \sin\omega\sqrt{1-\beta^2}\Delta t_i \right) \right. \\
& \left. - \frac{2\beta}{\omega^3\Delta t_i} \left(\omega\sqrt{1-\beta^2}\sin\omega\sqrt{1-\beta^2}\Delta t_i + \beta\omega\cos\omega\sqrt{1-\beta^2}\Delta t_i \right) \right] \\
& - \frac{1}{\omega^2\Delta t_i}
\end{aligned} \tag{A.7e}$$

From (A.3), it follows that the absolute acceleration, \ddot{z}_i , of the mass at time t_i is given by

$$\ddot{z}_i = \ddot{x}_i + a_i = -(2\beta\omega\dot{x}_i + \omega^2x_i) \tag{A.8}$$

Hence, if the displacement and velocity of the oscillator are known at some time t_o , the state of the oscillator at all subsequent times t_i can be computed exactly by a step-by-step application of (A.7) and (A.8). The computational advantage of this approach lies in the fact that A and B depend only on β , ω and Δt_i . β and ω are constant during the calculation of each spectrum value, and if Δt_i is constant also, x_i , \dot{x}_i and \ddot{z}_i can be evaluated by the execution of only ten multiplication operations for each time step of integration. Matrices A and B, defined by the rather complicated expressions, (A.7d) and (A.7e), need to be evaluated only at the beginning of each spectrum calculation. If varying time intervals are used, it is necessary, in general, to compute A and B at each step of integration. However, by rounding the time coordinates of the record, the

number of these matrices needed during the calculation can be reduced to only a few. These, too, can be computed at the beginning of the calculation and called upon when needed, therefore saving computing time.

4. Fourier Spectrum

The definition of the Fourier transform of the absolute ground acceleration is:

$$F(\omega) = \int_0^T a(\tau) e^{-j\omega\tau} d\tau = \int_0^T a(\tau) (\cos\omega\tau + j \sin\omega\tau) d\tau \quad (\text{A.9})$$

where T is the duration of signal.

Fourier amplitude spectrum FS is

$$FS = \left\{ \left[\int_0^T a(\tau) \cos\omega\tau d\tau \right]^2 + \left[\int_0^T a(\tau) \sin\omega\tau d\tau \right]^2 \right\}^{1/2} \quad (\text{A.10})$$

For an undamped oscillator $\beta = 0$, the relative velocity spectra, SV_o is

$$\begin{aligned} \text{Max} | \dot{x}(t) | &= \text{Max} \left| \int_0^t a(\tau) \cos\omega(t-\tau) d\tau \right| \\ &= \text{Max} \left| \left[\int_0^t a(\tau) \cos\omega\tau d\tau \right] \cos\omega t + \left[\int_0^t a(\tau) \sin\omega\tau d\tau \right] \sin\omega t \right| \end{aligned} \quad (\text{A.11})$$

This quantity is maximum at $t=t_{\max}$ where $t_{\max} \leq T$. If $t_{\max} = T$, $FS = SV_o$ otherwise $FS \leq SV_o$. It is important to note that at $\omega = 0$, SD and SV approach maximum ground displacement and velocity

respectively, and SA approaches zero. For this same situation, however, $PSRV = \omega SD = 0$. Thus at zero frequency PSRV can clearly depart considerably from SV.

5. Energy Considerations

Various energy expressions are defined in such a way that they can be conveniently related to response spectra. The maximum strain energy stored in the spring-mass system of a simple damped harmonic oscillator is:

$$\text{Maximum strain energy} = \frac{1}{2} k \left[x(t) \right]_{\max}^2 = \frac{1}{2} k (SD)^2 \quad (\text{A.12})$$

Energy per mass, E_s , will become

$$E_s = \frac{1}{2} \frac{k}{m} (SD)^2 = \frac{1}{2} (PSRV)^2 \quad (\text{A.13})$$

Note that PSRV enters directly into this energy expression rather than SV.

Another energy expression of interest is total energy of the system E_T , which varies with time as:

$$E_T(t) = \frac{1}{2} m \left[\dot{x}(t) \right]^2 + \frac{1}{2} k \left[x(t) \right]^2 \quad (\text{A.14})$$

Substituting in the integral expression for $x(t)$ from (A.3), it is seen that for zero damping $\beta = 0$,

$$\frac{2E_T(t)}{m} = \left[\int_0^t a(\tau) \cos \omega \tau d\tau \right]^2 + \left[\int_0^t a(\tau) \sin \omega \tau d\tau \right]^2 \quad (\text{A.15})$$

which at the end of the earthquake is equal to the square of the Fourier amplitude spectrum of the ground acceleration, or in another words, total energy per mass is equal to or less than $|SV_0|^2$.

BIBLIOGRAPHY

- Aki, K. (1969). Analysis of seismic coda of local earthquake as scattered waves, *J. Geophys. Res.* **74**, 615-631.
- Aki, K. (1980). Attenuation of shear waves in the lithosphere for frequencies from 0.05 to 25 Hz, *Phys. Earth Planet. Interiors* **21**, 50-60.
- Aki, K. (1981). Source and scattering effects on the spectra of small local earthquakes, *Bull. Seism. Soc. Am.* **71**, 1678-1700.
- Aki, K. and B. Chouet (1975). Origin of coda waves: source, attenuation and scattering effects, *J. Geophys. Res.* **80**, 3322-3342.
- Aki, K. and P.G. Richards (1980). *Quantitative Seismology: Theory and methods*, W.H. Freeman, San Francisco, Calif.
- Anderson, J.G. and S.E. Hough (1984). A model for the shape of the Fourier amplitude spectrum of acceleration at high frequencies, *Bull. Seism. Soc. Am.* **74**, 1969-1994.
- Atkinson, G.M. and R.F. Mereu (1992). The shape of ground motion attenuation curves in southeastern Canada, *Bull. Seism. Soc. Am.* **82**, 2014-2031.
- Bouchon, M. (1982). The complete synthesis of seismic crustal phases at regional distances, *J. Geophys. Res.* **87**, 1735-1742.
- Burger, R.W., P.G. Somerville, J.S. Barker, R.B. Herrmann, and D.V. Helmberger (1987). The effect of crustal structure on strong ground motion attenuation in eastern North America, *Bull. Seism. Soc. Am.* **77**, 420-439.
- Brune, J.N. (1970). Tectonic stress and the spectra of seismic shear waves from earthquakes, *J. Geophys. Res.* **75**, 4997-5009.
- Carr W.J. (1990). Styles of extension in the Nevada Test Site region, southern Walker Lane Belt; An integration of volcano-tectonic and detachment fault models, in Wernicke, B.P., ed, *Basin and Range extensional tectonics near the latitude of Las Vegas, Nevada*, Geological Society of America Memoir 176, Boulder, Colorado, 283-303.
- Castro, R.R., J.G. Anderson, and S.K. Singh (1990). Site response,

- attenuation, and source spectra of S waves along the Guerrero, Mexico subduction zone, *Bull. Seism. Soc. Am.* **80**, 1481-1503.
- Campillo, M., M. Bouchon, and B. Massinon (1984). Theoretical study of the excitation, spectral characteristics, and geometrical attenuation of regional seismic phases, *Bull. Seism. Soc. Am.* **74**, 79-90.
- Chandrasekhar (1960). *Radiative Transfer*, Dover, New York (revised version of 1950).
- Dainty, A.M. (1981). A scattering model to explain seismic Q observations in the lithosphere between 1 and 30 Hz, *Geophys. Res. Lett.*, **8**, 1126-1128.
- Dwyer, J.J., R.B. Herrmann, and O.W. Nuttli (1983). Spatial attenuation of the Lg wave in the central United States, *Bull. Seism. Soc. Am.* **73**, 781-796.
- Eaton, G.P. (1982). The Basin and Range Province: Origin and tectonic significance, *Ann. Rev. Earth Planet. Sci.*, **10**, 10,409-10,440.
- Eaton, G.P. (1984). The Miocene Great Basin of western North America as an extending back-arc region, *Tectonophysics* **102**, 275-295.
- Ewing, M., W.S. Jardetsky, and F. Press (1957). *Elastic Waves in Layered Media*, McGraw-Hill, New York.
- Farber, R.-G. (1989). Recursive deconvolution filters for seismograph system, *Bull. Seism. Soc. Am.* **79**, 1629-1641.
- Frankel, A. (1982). Source parameters and scaling relationships of small earthquakes in the northern Caribbean, *Bull. Seism. Soc. Am.* **72**, 1173-1190.
- Frankel, A. (1991). Mechanism of seismic attenuation in the crust: Scattering and anelasticity in New York State, South Africa, and southern California, *J. Geophys. Res.* **96**, 6269-6290.
- Frankel, A. and R. W. Clayton (1986). Finite difference simulations of seismic scattering: Implication for the propagation of short period seismic waves in the crust and models of crustal heterogeneity, *J. Geophys. Res.*, **91**, 6465-6489.

- Frankel, A. and L. Wennerberg (1987). Energy-flux model of seismic coda: Separation of scattering and intrinsic attenuation, *Bull. Seism. Soc. Am.* **77**, 1223-1251.
- Frankel, A., A. McGarr, J. Bicknell, J. Mori, L. Seeber, and E. Cranswick (1990). Attenuation of high-frequency shear waves in the crust: Measurements from New York State, South Africa, and southern California, *J. Geophys. Res.* **95**, 17,441-17,457.
- Gomberg, J. (1991). Seismicity and shear strain in the Southern Great Basin of Nevada and California, *J. Geophys. Res.* **96**, 16,383-16,400.
- Gupta, I.N. and K.L. McLaughlin (1987). Attenuation of ground motion in the eastern United States, *Bull. Seism. Soc. Am.* **77**, 366-383.
- Hagstrom, J.T., J.J. Daniels, and J.H. Scott (1980). Interpretation of the geophysical well-log measurements in drill hole UE25Sa-1, Nevada Test Site, Radiative waste program, *U.S. Geological Survey, Open-File Report 80-941*, 32p.
- Hanks, T.C. (1982). f_{max} , *Bull. Seism. Soc. Am.* **72**, 1867-1879.
- Harmsen, S.C. and A.M. Rogers (1987). Earthquake location data for the Southern Great Basin of Nevada and California: 1984 through 1986, *U.S. Geological Survey, Open-File Report 87-596*, 92p.
- Herrmann, R.B. and A. Kijko (1983). Short-period L_g magnitudes: instrument, attenuation and source effects, *Bull. Seism. Soc. Am.* **73**, 1835-1850.
- Hasegawa, H.S. (1985). Attenuation of L_g waves in the Canadian Shield, *Bull. Seism. Soc. Am.* **75**, 1569-1582.
- Hoshiya, M. (1991). Simulation of multiple-scattered coda wave excitation based on the energy conservation law, *Phys. Earth Planet. Inter.* **67**, 123-136.
- Hudson, D.E. (1979). Reading and interpreting strong motion accelerograms, Earthquake Engineering Research Institute.
- Humphrey, J.R. and J.G. Anderson (1992). Shear-wave attenuation and site response in Guerrero, Mexico, *Bull. Seism. Soc. Am.* **82**, 1622-1645.

- Ishimaru, A. (1978). *Wave propagation and Scattering in Random Media*. Vols. 1 and 2, Academic Press, New York.
- Joyner, W.B. and D.M. Boore (1988). Measurement, characterization, and prediction of strong ground motion, from *Proc. of Earthquake Engineering & Soil Dynamics II GT Div/ASCE*, Park City, Utah, Geotechnical Div., American Society of Civil Engineers, 43-102.
- Kennett, B.L.N. (1985). On regional S, *Bull. Seism. Soc. Am.* **75**, 1077-1086.
- King, K.W. and W. Hays (1977). Comparison of seismic attenuation in northern Utah with attenuation in four other regions of the western United States, *Bull. Seism. Soc. Am.* **67**, 781-792.
- Koponichev, Yu. F. (1975). A Model of generation of the tail the seismogram, *Doklady Akad. Sci. USSR* **222**, 333-335 (in Russian).
- Koyanagi, S., K. Mayeda, and K. Aki (1991). Frequency-dependent site amplification factors using the S-wave coda for the island of Hawaii, *Bull. Seism. Soc. Am.* , .
- Lawson, C.L. and R.J. Hanson (1974). *Solving Least Squares Problems*. Prentice-Hall, Inc., Englewood Cliffs, N.J.
- Levenberg, K. (1944). A method for the solution of certain nonlinear problems in least squares, *Quarterly of Applied Mathematics* **2**, 164-168.
- Marquardt, D.W. (1963). An algorithm for least-squares estimation of nonlinear parameters, *J. Soc. Indust. Appl. Math.* **11**, 431-441.
- Marschall, R. (1984). Ein- und zweidimensionale Rekursive-Filter und ihre Anwendung in der Seismik, *Habilitations-Schrift*, Ruhr-Universität Bochum.
- Mayeda, K. (1991). High frequency scattered S-waves in the lithosphere: Application of the coda method to the study of source, site and path effects, *Ph.D. Dissertation*, University of Southern California.
- Mayeda, K., F. Su, and K. Aki (1991). Seismic albedo from the total seismic energy dependence on hypocentral distance in southern California, *Phys. Earth Planet. Inter.* **67**, 104-114.

- Mayeda, K., S. Koyanagi, M. Hoshiya, K. Aki, and Y. Zeng (1992). A comparative study of scattering, intrinsic and coda Q^{-1} for Hawaii, Long Valley, and central California between 1.5 and 15.0 Hz, *J. Geophys. Res.* **97**, 6643-6660.
- McSweeney, T.J., N.N. Biswas, K. Mayeda, and K. Aki (1991). Scattering and anelastic attenuation of seismic energy in central and south-central Alaska, *Phys. Earth Planet. Inter.* **67**, 115-122.
- Mitchell, B.J. and J. Xie (1994). *J. Geophys. J. Int.* (in press).
- Nelson, P.H., D.C. Miller, U. Schimschal, J.E. Kibler (1991). Geophysical logs and core measurements from forty boreholes at Yucca Mountain, Nevada, *U.S. Geological Survey Map GP-1001*.
- Nigam, N.C. and P.C. Jennings (1968). Digital calculation of response spectra from strong-motion earthquake records, Earthquake Engineering Laboratory, California Institute of Technology, Pasadena, California.
- Nuttli, O.W. (1973). Seismic wave attenuation and magnitude relations for eastern North America, *J. Geophys. Res.* **78**, 876-885.
- Oppenheim, A.V. and R.W. Schaffer (1975). *Digital signal processing*, Prentice-Hall, 585 pp.
- Ou, G.-B. (1990). A study of the use of estimation theory in strong ground motion seismology, *Ph.D. Dissertation*, St. Louis University.
- Ou, G.-B. and R.B. Herrmann (1990). A statistical model for ground motion produced by earthquakes at local and regional distances, *Bull. Seism. Soc. Am.* **80**, 1397-1417.
- Phillips, W.S. and K. Aki (1986). Site amplification of coda waves from local earthquakes in central California, *Bull. Seism. Soc. Am.* **76**, 627-648.
- Rautian, T.G. (1976). Role of source and medium in the formation of seismic oscillations near local earthquakes, in *Investigations of the Physics of Earthquakes*, Nauka Publishing House, Moscow, (in Russian), 27-55.
- Rautian, T.G. and V.I. Khalturin (1978). The use of the coda for determination of the earthquake source spectrum, *Bull.*

Seism. Soc. Am. 68, 923-948.

- Roecker, S.W., B.E. Tucker, J.L. King, and D. Hazfeld (1982). Estimates of Q in central Asia as a function of frequency and depth using the coda of locally recorded earthquakes, *Bull. Seism. Soc. Am.* 72, 129-149.
- Rogers, A.M. S.C. Harmsen, and M.E. Mermonte (1987). Evaluation of seismicity of the Southern Great Basin and its relationship to the tectonic framework of the region, *U.S. Geological Survey Open-File Report 87-408*, 196p.
- Russell, D. R. (1987). Multichannel processing of dispersed surface waves, *Ph.D. dissertation*, Saint Louis University.
- Seidl, D. (1980). The simulation problem for broad-band seismograms, *J. Geophys.* 48, 84-93.
- Su, F., K. Aki, T. Teng, Y. Zeng, S. Koyanagi, and K. Mayeda (1992). The relation between site amplification factor and surficial geology in central California, *Bull. Seism. Soc. Am.* 82, 580-602.
- Taylor, S.R. (1983). Three-dimensional crust and upper mantle structure at the Nevada Test Site, *J. Geophys. Res.* 88, 2220-2232.
- Toksöz, M.N., A.M. Dainty, E. Reiter, and R. Wu (1988). A model for attenuation and scattering in the Earth's crust, *Pageoph* 128, 81-99.
- Tsujiura, M. (1978). Spectral analysis of the coda waves from local earthquakes, *Bull. Earthquake Res. Inst. Tokyo Univ.* 53, 1-48.
- Tucker, B.E. and J.L. King (1984). Dependence of sediment-filled valley response on input amplitude and valley properties, *Bull. Seism. Soc. Am.* 74, 153-165.
- Wu, R.S. (1982). Attenuation of short period seismic waves due to scattering, *Geophys. Res. Lett.*, 9, 9-12.
- Wu, R.S. (1984). Seismic wave scattering and the small scale inhomogeneities in the lithosphere, *Ph.D. Thesis*, Massachusetts Institute of Technology, Cambridge, Massachusetts.
- Wu, R.S. (1985). Multiple scattering and energy transfer of seismic waves - separation of scattering effect from intrinsic

attenuation - I. Theoretical modeling, *Geophys. J. R. Astron. Soc.* **82**, 57-80.

Wu, R.S. and K. Aki (1988). Multiple scattering and energy transfer of seismic waves - separation of scattering effect from intrinsic attenuation. II. Application of the theory to Hindu Kush region, *Pageoph* **128**, 49-80.

Xie, J. and B.J. Mitchell (1990). Attenuation of multiphase surface waves in the Basin and Range province, part I: Lg and Lg coda, *Geophys. J. Int.* **102**, 121-137.

VITA AUCTORIS

Mohammad Reza Samiezhadé Yazd was born in Tehran, Iran on April 21, 1953. He finished his elementary and secondary education in Tehran. After attending Arya-Mehr University of Technology he graduated with a B.S. degree in physics in January 1977. He then enrolled at Columbia University in the city of New York and graduated with a M.S. degree in applied physics in May 1979.

Mohammad Reza Samiezhadé Yazd joined St. Louis University, department of Earth and Atmospheric Sciences in September of 1982 to pursue a Ph.D. degree in geophysics. He has taught physics and mathematics in St. Louis Community College from 1987 to 1993 and is a member of the Seismological Society of America and the American Geophysical Union.